Investigation into the Effect of Thermal Management on the Capacity Fade of Lithium-ion Batteries

by

Andrew Carnovale

A thesis
presented to the University of Waterloo
in fulfillment of the
thesis requirement for the degree of
Master of Applied Science
in
Mechanical and Mechatronics Engineering

Waterloo, Ontario, Canada, 2016

I hereby declare that I am the sole author of this thesis. This is a true copy of the thesis, including any required final revisions, as accepted by my examiners.

I understand that my thesis may be made electronically available to the public.

Abstract

The popularity of electric (and hybrid) vehicles has raised the importance of effective thermal management for lithium-ion batteries, both to prevent thermal runaway leading to a fire hazard, and to minimize capacity fade for longer lifetime. In this research, the focus was on the effect of thermal management on the capacity fade of lithium-ion batteries. A battery thermal management system will impact the battery operation through its temperature, thermal gradient and history, as well as the cell-to-cell temperature variations in a battery module. This study employed AutoLionST, a software for the analysis of lithium-ion batteries, to better understand capacity fade of lithium-ion batteries, complemented by the experimental investigation.

Experimental capacity fade data for a lithium-ion battery cycled under isothermal, 1C charge/discharge conditions was measured first, which was used to validate the numerical model. Then the software's ability to model degradation at moderate to lower temperatures of around 20°C was investigated with simulation of battery capacity under isothermal conditions for a variety of operating temperatures.

The next phase of the study modeled battery capacity fade under a variety of different operating conditions. In the first set of simulations, three different base temperatures, constant discharge rates, and heat transfer coefficients were considered. In the second set of simulations, a fixed-time drive cycle was used as the load case to model a typical day's worth of driving, while varying the base temperature, charge voltage, and heat transfer coefficient. These simulations were repeated considering regenerative braking. It was found that temperature has the largest direct impact on the capacity fade which is expected based on prior sutdies. Further, it was found that thermal management does have a significant impact on capacity fade, as effective thermal management is capable of preventing significant battery temperature rise. As concluded from the constant discharge rate simulations, effective thermal management is most crucial at high discharge rates, which will result in high heat generation. It was also concluded from both constant discharge rate and drive cycle simulations, that thermal management is much more effective at preventing capacity fade at battery temperatures close to 20°C. In the drive cycle simulations, using the same discharge profile, there is a much more significant spread in battery capacity between high and low heat transfer coefficients for a lower base temperature (20°C) compared to higher base temperatures (35°C and 50°C). As well, it was shown that using a lower charge voltage will result in slightly less capacity fade over cycling. Additionally, using regenerative braking makes it more realistic to use lower charge voltages, since the battery pack can be recharged during operation, thereby increasing driving range, while preventing increased capacity fade.

The final phase showed that effective thermal management would be even more imperative for more intense and realistic driving styles. It was shown that different driving styles can result in significant rises in heat generation and hence battery temperature. From previous conclusions this implies that much intense driving (high acceleration) can result in a higher need for effective thermal management.

Acknowledgements

Firstly, I would like to thank my supervisor, Dr. Xianguo Li, for his guidance, advice, and support during my master's degree. His feedback throughout this period has been vital to the completion of my thesis, and all the work which preceded it.

As well, I would like to thank Grant Unsworth for all his recommendations regarding the experimental setup, as well as the direction of the overall project. Grant was always helpful whenever I needed advice, or just needed someone to discuss ideas with, and for that I am most grateful.

I would as like to thank Dr. Ben Kenney, for all his input and industry experience to help guide the project during our partnership. I would also like to acknowledge the Natural Sciences and Engineering Research Council of Canada for their financial support during the Engage project.

Finally, I'd like to thank Dr. Michael Collins and Dr. Serhiy Yarusevych for the time they took to read and evaluate my thesis, as well as their comments.

Dedication

I would like to dedicate this thesis to Romeo and Maria DiSimone, Michele Carnovale, and especially Carmela Carnovale.

You are all sorely missed.

Table of Contents

List of Figures

List of Tables

Nomenclature

F,	Faraday's constant, $C \cdot mol^{-1}$
R,	Universal gas constant, $J \cdot K^{-1} \cdot mol^{-1}$
T,	Battery temperature, *K or °C*
$\Delta G°$,	Gibbs free energy under standard conditions, *J*
ΔG	Gibbs free energy, *J*
E^0,	Standard cell potential, *V*
E,	Cell potential, *V*
a_i,	Activity for species *i*, *no units*
$(\eta_{ct})_i$,	Anode or cathode activation polarization, *V*
$(\eta_c)_i$,	Anode or cathode concentration polarization, *V*
i,	Cell current, *A*
R_i,	Cell internal resistance, Ω
SOC,	Cell state of charge, *no units*
DOD,	Cell depth of discharge, *no units*
c,	Battery capacity, *Ah*
c_0,	Initial battery capacity, *Ah*
N_{cell},	Number of cells in stack, *no units*
E_o/E_{oc}/U/OCV,	Open circuit voltage, *V*
V,	Battery voltage, *V*
LX,	Thickness of battery stack, *m*
q,	Volumetric battery heat generation, $W \cdot m^{-3}$
L,	Thickness of a single cell (two electrodes, separator), *m*
L_-,	Thickness of a single negative electrode, *m*
L_+,	Thickness of a single positive electrode, *m*
L_{sep},	Thickness of a single separator, *m*
r_s,	Radius of particle of active material, *m*
$\emptyset_s$,	Solid-phase electrical potential, *V*
j^{Li},	Volumetric electrode current from all reactions, $A \cdot m^{-3}$
σ_s,	Solid-phase electrical conductivity, $\Omega^{-1} \cdot m^{-1}$
σ_s^{eff},	Effective solid-phase electrical conductivity, $\Omega^{-1} \cdot m^{-1}$
ε_s,	Volume fraction of solid phase, *no units*
n,	Bruggeman exponent, *no units*
$\emptyset_e$,	Electrolyte-phase electrical potential, *V*
c_e,	Lithium-ion concentration, $mol \cdot cm^{-3}$
κ^{eff},	Effective ionic conductivity of electrolyte, $\Omega^{-1} \cdot m^{-1}$
κ_D^{eff},	Effective electrolyte diffusional conductivity, $A \cdot (ln(mol \cdot cm^{-3}))^{-1} \cdot m^{-1}$
t^0_+,	Transference number, *no units*
ε,	Volume fraction of lithium in the electrolyte phase, *no units*
D_e^{eff},	Effective electrolyte diffusion coefficient, $m^2 \cdot s^{-1}$
c_s,	Lithium concentration in the solid phase, $mol \cdot cm^{-3}$
D_s,	Solid-phase lithium diffusion coefficient, $m^2 \cdot s^{-1}$
a_s,	Specific interfacial electrode area, m^{-1}
ρ,	Battery density, $kg \cdot m^{-3}$
C,	Battery heat capacity, $J \cdot m^3 \cdot kg^{-1} \cdot K^{-1}$

q_r,	Heat generation due to reaction, $W \cdot m^{-2}$
q_j,	Joule heating, $W \cdot m^{-2}$
q_c,	Heat generation due to contact resistance, $W \cdot m^{-2}$
q_e,	Entropic heating, $W \cdot m^{-2}$
A_{cell},	Cell cross-sectional area, m^2
A_s,	Battery surface area, m^2
h_{conv},	Heat transfer coefficient, $W \cdot m^{-2} \cdot K$
T_{amb},	Ambient temperature (heat exchange temperature), *K or °C*
R_c,	Contact resistance, Ω
α_i,	Anodic/cathodic transfer coefficients, *no units*
η,	Local surface overpotential, *V*
i_o^{IC},	Exchange current density, $A \cdot m^{-2}$
$c_{s,e}$,	Lithium concentration at the electrode/electrolyte interface, $mol \cdot cm^{-3}$
j^{IC},	Volumetric electrode current due to intercalation reactions, $A \cdot m^{-3}$
i_s,	Side reaction current density, $A \cdot m^{-2}$
c_{EC},	Concentration of ethylene carbonate, $mol \cdot cm^{-3}$
D_{EC}^{eff},	Effective diffusivity of ethylene carbonate through film, $m^2 \cdot s^{-1}$
$i_{s,A}$,	Side reaction current density, $A \cdot m^{-2}$
$i_{t,A}$,	Total current density, $A \cdot m^{-2}$
$i_{0s,A}$,	Side reaction exchange current density, $A \cdot m^{-2}$
R_{SEI},	SEI film resistance, $\Omega \cdot m^2$
c_{EC}^s,	Ethylene carbonate concentration at reaction surface, $mol \cdot cm^{-3}$
δ_{SEI},	SEI layer thickness, *m*
M_{SEI},	SEI layer molecular weight, $g \cdot mol^{-1}$
ρ_{SEI},	SEI layer density, $g \cdot cm^{-3}$
κ_{SEI}^{eff},	Effective conductivity of electrolyte through SEI layer, $\Omega^{-1} \cdot m^{-1}$
$J_{s,C}$,	Side reaction rate per surface area, $mol \cdot m^{-2} \cdot s^{-1}$
ε_{AM},	Active material volume fraction, *no units*
F_{RR},	Rolling resistance, *N*
F_{AD},	Aerodynamic drag, *N*
F_I,	Inertial force, *N*
V_i,	Velocity at time *i*, $m \cdot s^{-1}$
C_D,	Coefficient of drag, *no units*
ρ_a,	Air density, $kg \cdot m^{-3}$
C_{rr},	Rolling resistance coefficient, *no units*
A_f,	Vehicle frontal area, m^2
W_c,	Curb weight, *kg*
W_p,	Payload, *kg*
W_t,	Total weight, *kg*

1 Introduction

In recent years, the topic of climate change has been gaining widespread attention across the world. Fortunately, governments across the globe are acknowledging the need to do something about this. In 2015, the Paris Agreement was adopted at the United Nations Climate Change Conference (COP21) [1]. This agreement has been signed by representatives of 175 countries and will aim to limit the increase of global temperature, and hence, the reduction of greenhouse gas emissions will continue to be a major priority in mitigating climate change [1, 2]. In order to reduce the emission of greenhouse gases, renewable energy sources must be adopted, and advanced technologies must be implemented.

Data has shown that transportation is a major contributor to greenhouse gas emission. The *U.S. Greenhouse Gas Inventory Report: 1990-2014* showed that in 2014, 26% of greenhouse gas emissions in the United States (one of the world's worst polluters) were due to transportation [3]. Similarly, in Canada in 2014, it was reported that transportation accounted for 23% of greenhouse gas emissions [4]. Meanwhile, in the entire world, transportation accounts for 14% of greenhouse gas emission [5]. All these figures imply that the burning of fossil fuels due to transportation (especially in North America) is a significant contributor to greenhouse gas emissions, and hence climate change.

A widespread solution to greenhouse gas emissions caused by transportation is to reduce or eliminate the use of internal combustion engines (ICE); this includes the use of battery electric vehicles (BEVs), fuel cell electric vehicles (FCEVs), and hybrid electric vehicles (HEVs) [6]. Note that BEVs and FCEVs are pure electric vehicles, where HEVs still employ the use of an ICE coupled with an alternate power source.

Currently, electric vehicles represent a small portion of vehicle sales worldwide; however, in certain parts of the world, electric vehicles have already possessed a large portion of the automobile market. In 2015, Norway led the world in electric vehicle market share (newly purchased passenger electric vehicles as a percent of total passenger vehicles purchased) with 22.39% [7]. For reference to a North American market, electric vehicles accounted for only 0.66% of passenger vehicles purchased in 2015 in the United States [7]. It should, however, be noted that the United States trails only China in total electric vehicle purchases in 2015 [7].

In terms of the electric vehicles being sold, in the United States the three most popular electric vehicles sold in 2015 were the Nissan Leaf, Tesla Model S (both fully BEVs), and the Chevrolet Volt (an HEV); these accounted for approximately 50% of total electric vehicle sales [8]. Between the top selling fully electric vehicles, the Nissan Leaf is relatively affordable, however offers a shorter total range of 84 miles (for 2014, and 2015 models) [9, 10]. Meanwhile, the Tesla Model S, is considered a luxury car, but offers a total range of up to 265 miles with the 85kWh battery pack [9, 11]. The next generation of fully electric vehicles will look to eradicate this disparity with affordable, high range fully electric vehicles. Chevrolet is looking the release the Bolt, an affordable BEV with a 200 mile range [9]. While in early 2016 the Tesla Model 3 was revealed, boasting 215 mile range, with a cost of $35,000; within approximately a month of the reveal Tesla received close to 400,000 orders for the Model 3 [12]. With a wide range of affordable and reliable options becoming available, it is safe to assume the EV market will only improve from its current state.

A further indicator that our society will trend towards EVs is the incentive programs that governments are putting in place. In Canada, in the provinces of Ontario, British Columbia, and Quebec, rebates of up to $10,000 (varies by province) are available, as well as other incentive programs that make purchasing an EV a more attractive option [13, 14, 15]. In the United States, similar programs exist, with income tax credits of up to $7,500, plus additional incentives varying by state [16].

This quick overview shows that it seems likely that with the need to reduce greenhouse gas emissions, the growing options of reliable and affordable electric vehicles coming in the near future, and ongoing government incentives, that electric vehicles will grow in popularity. In order to power these vehicles, lithium-ion (Li-ion) batteries are preferred, primarily due to their high energy density and high power density [17, 18]. The next section of the report will discuss the operational principles of a battery (specifically a Li-ion battery), as well as advantages, disadvantages of using Li-ion batteries.

1.1 Lithium-ion battery fundamentals

1.1.1 Lithium-ion cell assembly

A typical battery is composed of multiple electrochemical cells; each of these cells converts chemical energy to electrical during discharge, and vice versa during charging (for electric vehicles, and in this study only rechargeable batteries are considered) [19]. The most basic components of a cell are negative and positives electrodes (anode and cathode, respectively), the electrolyte, and the separator [19]. Figure 1-1 shows a simplified schematic of a single electrochemical cell with the four major components. During discharge, an oxidation reaction occurs at the negative electrode [19]. During this process positively charged ions (lithium ions) are transferred from the negative electrode to the positive via the electrolyte which acts an as ionic conductor [19]. At the same time electrons are transferred from the negative to positive electrode via an external circuit, which can be used to power some external load [19]. The separator is used to separate the two electrodes, preventing transport of electrons (a short circuit), while allowing transport of ions [19]. At the positive electrode, ions and electrons recollect in a reduction reaction [19]. During charge periods the reverse process occurs. For simplicity and consistency with convention, the negative electrode, termed the anode, will refer to the negative electrode *during discharge*, while the positive electrode, termed the cathode, will refer to the positive electrode again *during discharge*.

The electrodes are composed of two primary components; the electrode active material, and the current collector [19]. The active material is portion of the electrode which participates in the redox reactions; the anode active material is often carbon based, while the cathode active material is often a transition metal oxide [19]. The current collectors are merely thin metal plates which collect and distribute electrons from the redox reactions; the negative electrode current collector is often copper, while the positive is often aluminum [19]. Figure 1-2 shows a more detailed depiction of a lithium-ion cell, distinguishing between the electrode active materials and current collectors.

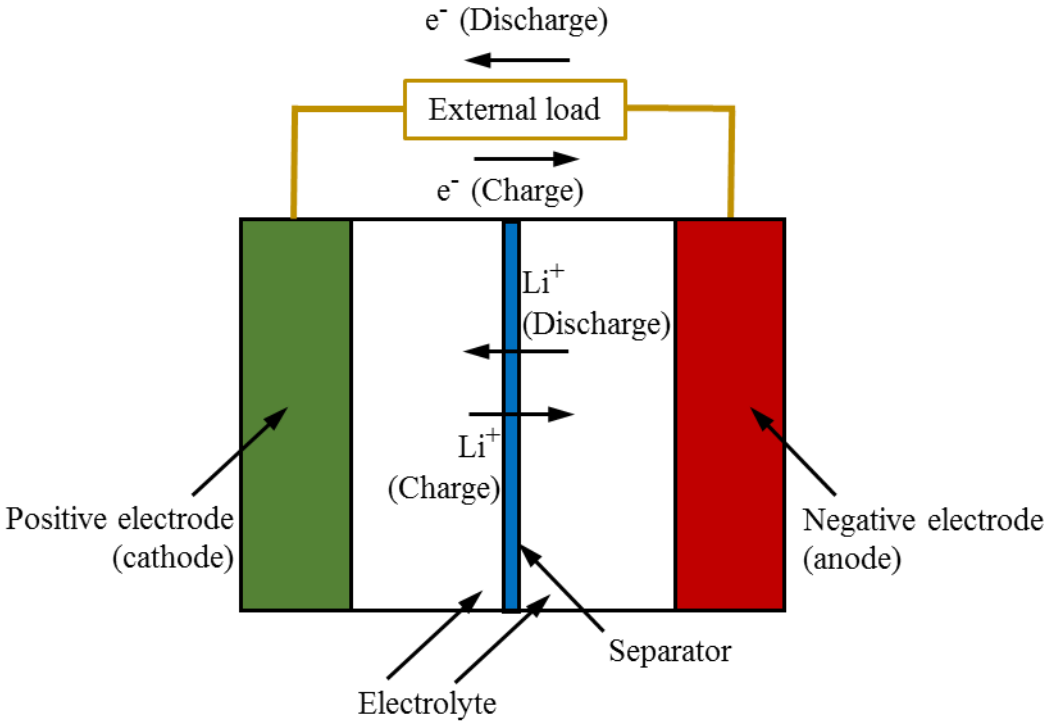

Figure 1-1: Simple schematic of lithium-ion electrochemical cell

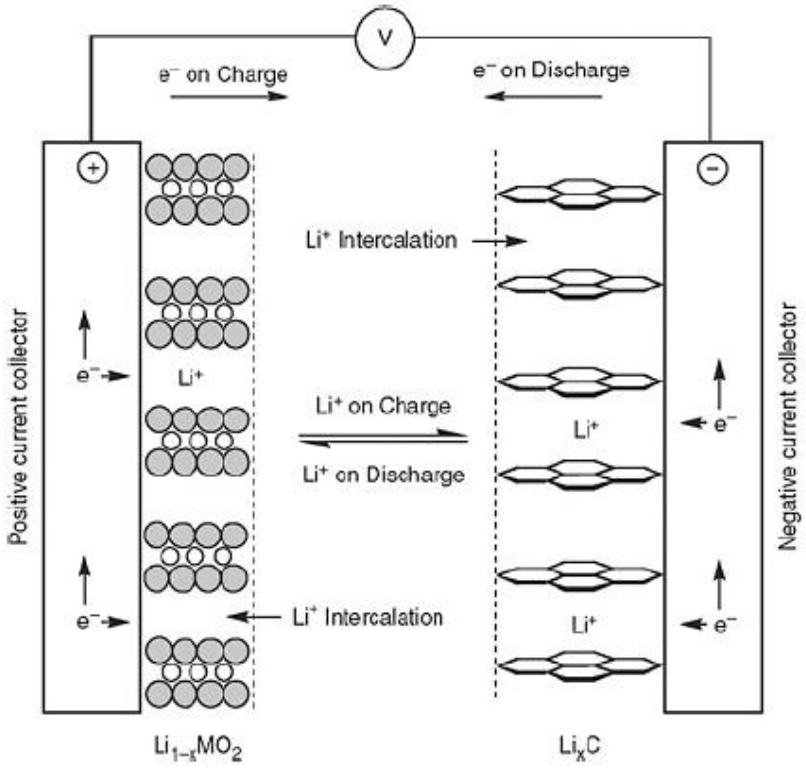

Figure 1-2: Detailed schematic of lithium-ion cell [20]

Other components of the electrodes can include conductive agents and binders. Conductive agents will aid with electrical conductivity throughout the electrode active material; common conductive agents are carbon based, such as acetylene black [19]. Binders are used to improve mechanical stability in the electrodes [19]. During charge and discharge electrode active material can expand and contract, this can lead to poor contact between electrode materials, and hence increased contact resistance [19]. Binders supply improved contact between active material, conducting agents, and the current collector; binders are often polymer based with polyvinylidene fluoride (PVDF) being a popular option [19].

1.1.2 Lithium-ion cell operational fundamentals

Several fundamental reactions are occurring during battery operation. These fundamental reactions can be generalized to be independent of electrode material. The current discussion will assume a generic transition metal oxide as the cathode active material (MO_2), and a generic carbon based anode active material (C), as was shown in Figure 1-2 [20]. As previously mentioned, during discharge, an oxidation reaction occurs at the anode, causing deintercalation of lithium from the anode, and causing electrons to flow through the external circuit [20]. This lithium, in the form of lithium ions, are shuttled through the electrolyte to the cathode [20]. At the cathode a reduction reaction occurs, with lithium being intercalated into the cathode, and electrons collected at the cathode via the external circuit [20]. The opposite reactions occur during charge (deintercalation of lithium at the cathode, intercalation of lithium at the anode). These half-reactions can be summarized in the following two Equations; note that the forward reactions describe discharging, while the backward reactions describe charging [20]:

Anode half-reaction:

$$Li_xC \rightleftharpoons C + xLi^+ + xe^- \tag{1}$$

Cathode half-reaction:

$$Li_{1-x}MO_2 + xLi^+ + xe^- \rightleftharpoons LiMO_2 \tag{2}$$

Overall reaction:

$$Li_xC + Li_{1-x}MO_2 \rightleftharpoons LiMO_2 + C \tag{3}$$

For these reactions, a theoretical maximum available electric energy from this chemical transformation can be expressed using the concept of free energy, $\Delta G°$ [20, 21]:

$$\Delta G^0 = nFE^0 \tag{4}$$

The above expression describes the maximum potential electrical energy available from a cell operating at standard state, with standard potential, $E°$ [19, 20]. For a cell operating at non-standard conditions, the voltage of the cell can be expressed using a Nernst; the Nernst equation for the reactions shown in Equations (1) – (3) is shown below [19, 20]:

$$E = E^0 - \frac{RT}{nF}\ln\left(\frac{a_{LiMO2}a_C}{a_{Li_xC}a_{Li1-xMO2}}\right) \tag{5}$$

In Equations (4) and (5), R is the gas constant, T is the absolute temperature, n is the number of moles of electrons transferred during operation, F is Faraday's constant, and each of the terms inside the logarithmic function (a_i) is the activity for the specified species in the overall reaction shown in Equation (3) [19, 20]. Using the cell voltage for non-standard conditions, E, the maximum potential electrical energy, ΔG, can be calculated using Equation (4).

While Equation (5) described the theoretical cell voltage from a thermodynamic standpoint, a polarization curve can be used to observe the effect that a given operating current will have on cell voltage [20]. The polarization curve shows the expected drop in cell voltage due to energy losses during cell operation, which is mostly given off as heat [20]. Figure 1-3 shows the polarization curve for an electrochemical cell.

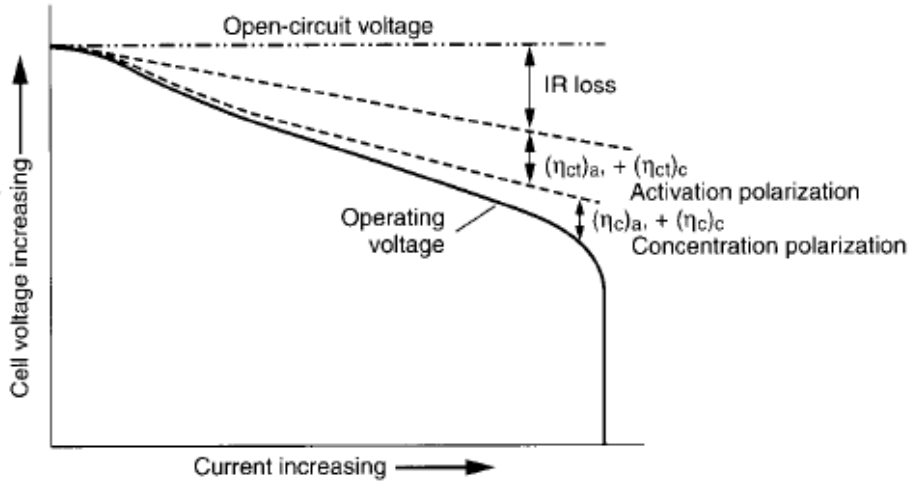

Figure 1-3: Electrochemical cell polarization curve [20]

As shown in Figure 1-3, three types of losses cause an operating voltage lower than open-circuit voltage (OCV) with increasing current. These are *IR* losses (also known as *IR* drop, ohmic losses, or ohmic polarization), activation polarization, and concentration polarization [20]. *IR* losses is the energy lost to the internal resistance of the cell, and is equal to the operating current multiplied by the internal resistance of the cell [20]. Activation polarization refers to the energy lost to the electrochemical reactions at the electrodes, as these reactions require an energy barrier be overcome for the reaction to occur [20]. Concentration polarization refers to energy lost to unfavourable concentration gradients at the electrode surface reaction sites; this implies a lack of reactants diffusing to the reaction sites, and a lack of products diffusing away from reaction sites [19, 20]. The cell voltage, corrected for these losses is shown in the below equation [20]:

$$E = E_0 - [(\eta_{ct})_a + (\eta_c)_a] - [(\eta_{ct})_c + (\eta_c)_c] - iR_i \quad (6)$$

Here, E_0, is the OCV, $(\eta_{ct})_a$ and $(\eta_{ct})_c$ respectively denote the anode and cathode activation polarization, $(\eta_c)_a$ and $(\eta_c)_c$ respectively denote the anode and cathode concentration polarization, and iR_i denotes ohmic losses due to internal resistance [20].

1.1.3 Lithium-ion battery capacity

When discussing battery performance, capacity is a measure of charge of the battery. Unlike the measure of electrical charge which is measured in coulombs (C), the common units for capacity is ampere-hours (Ah, also commonly mAh). With units of Ah, capacity becomes a very practical measure of battery charge. For instance, a fully charged battery with a rated capacity of 10Ah, should be capable of discharging 10A for one hour (or similarly 20A for 30 minutes, etc.). Furthermore, capacity can be represented per unit mass, often quoted with units of mAh/g. Specific capacity is often used to describe the available charge from a given electrode active material; for instance, the first charge capacity of graphite active material for the anode in this study is 371.933 mAh/g.

From capacity other common battery related measures are defined. C-rate, is an alternate, non-dimensional form of current. It can be found by dividing the specified current by the battery capacity. For example, drawing a 10Ah battery at 1C means a drawn current of 10A, a C-rate of 0.5C draws a current of 5A, and a C-rate of 2C draws a current of 20A.

Another battery parameter derived from capacity is state of charge (SOC). SOC is defined as the capacity of a battery divided by the maximum battery capacity range. Note that the maximum battery capacity range might not be the rated capacity. SOC is measured on a range between 0 and 1 (or based on percentage); 0 being fully discharged, 1 being fully charged. Depending on the operation of a battery the capacity can be higher than the rated capacity, and over cycling a battery's capacity will decrease, but SOC should still be on a range between 0 and 1. Depth of discharge (DOD) is the compliment to SOC, it is a measure of discharge rather than a measure of charge. Opposite to SOC, using a scale from 0 to 1, a DOD of 0 implies a fully charged battery, while DOD of 1 implies a fully discharged cell.

Energy density is another important measure of a battery's energy. This is often represented by two measures, volumetric energy density, and specific energy, with common units of Wh/cm^3, and Wh/g, respectively. These measures are important in comparing different batteries, as an ideal battery for automotive applications should be lightweight, and take up minimal space, while providing sufficient power.

The important parameter measuring the lifetime of a battery is the capacity fade; which is defined as the irreversible losses in the capacity of a battery when it is cycled – discharge/charge cycling causes the maximum capacity of a battery to decrease over the number of cycles.

Now that the fundamentals of cell operation and important terms have been discussed, the next subsection will briefly address some of the materials used inside a lithium-ion cell.

1.1.4 Anode and Cathode Active Materials

As mentioned, the anode active material is often carbon based, while the cathode active material is often a transition metal oxide. This subsection will briefly discuss some of the different materials in use.

Some of the major preferred characteristics for anode materials are: materials should have a low potential and be close to the electrochemical potential of an anode utilizing lithium metal,

there should be insignificant changes in the crystal structure during redox reactions, and the material should promote reversible redox reactions [19]. In terms of properties, the anode should also allow diffusion of lithium ions, high electrical conductivity, and be high in density [19]. Firstly, anodes using lithium metal as the active anode material are often avoided due to safety concerns [19]. Carbon-based anode materials are often graphite, while common non-carbon materials include silicon, and tin based alloys [19]. Graphite provides an electrochemical potential very similar to that of lithium metal, and show nearly insignificant changes in the crystal structure, leading to superior cycling [19]. Silicon and tin alloys have a higher electrochemical potential, and show very poor cycling performance due to significant volume changes during charging and discharging; however, they provide very superior theoretical capacity compared to graphite [19].

Further work in carbon-based anodes will look to employ nanostructured materials to increase the capacity of these materials [22]. Some of the possibilities to increase anode material capacity are carbon nanotubes (CNTs) and nanofibers (CNFs), graphene, and porous carbon [22]. While all these options show increase in theoretical capacity compared to graphite, these materials all have drawbacks [22]. CNTs and CNFs generally have favourable Coulombic efficiency (ability to transfer charge during electrochemical processes), but a low volumetric energy density [22]. Graphene tends to have low initial Coulombic efficiency, large irreversible capacity, and low volumetric energy density, while porous carbon also has low volumetric energy density, and large irreversible capacity [22]. Current lithium-ion battery technology still heavily relies on graphite anode material, however advances in alloys, or other carbon materials might result in anode active material with similar cycling characterises to graphite, but superior theoretical capacity.

Active materials for cathodes should have the following characteristics: have a high potential (for a high potential difference compared to the anode), reversible behaviour through cycling (including minimal irreversible crystal structure phase transitions), electrochemical and thermal stability to minimize side reactions [19]. As well, the cathode active material should be light, with high density, and highly electrically and ionically conductive [19]. Some common cathode active materials include oxides of cobalt, manganese, nickel, and iron (such as $LiCoO_2$, $LiMn_2O_4$, $LiNiO_2$, $LiFePO_4$); many cathode designs include combinations of these metals (such as $LiNi_{1/3}Mn_{1/3}Co_{1/3}O_2$, commonly referred to as NMC) [19]. $LiCoO_2$ was used as the cathode active material in early lithium-ion batteries; research took place to find other cathode active materials with higher operating voltage, and larger rechargeable capacity, leading to higher energy density compared to $LiCoO_2$ [23]. $LiMn_2O_4$ has been used as it possesses a higher operating voltage than $LiCoO_2$ (flat operating voltage of 3.95V – 4.1V compared to 3.9V), however it also has a lower rechargeable capacity compared to $LiCoO_2$ [23]. Materials combining $LiNiO_2$ and $LiCoO_2$ display a higher rechargeable capacity, but a lower operating voltage compared to $LiCoO_2$, meaning these two batteries would still possess similar energy densities [23]. $LiNi_{1/3}Mn_{1/3}Co_{1/3}O_2$ shows only a slightly lower operating voltage compared to $LiCoO_2$, but a larger rechargeable capacity, leading to a battery with an energy density at least comparable to, if not greater than, a $LiCoO_2$ battery [23]. Batteries employed $LiNi_{1/2}Mn_{1/2}O_2$ cathode active material display similar characteristics to $LiNi_{1/3}Mn_{1/3}Co_{1/3}O_2$, however are difficult to manufacture [23]. Meanwhile $LiFePO_4$ is another option, as iron is one of the cheaper and more abundant metals [19]. As well, $LiFePO_4$ displays much improved structural, thermal, and chemical stability [19, 23]. At the same time, while $LiFePO_4$ is the safer option, it

generally possesses a lower operating voltage and smaller energy density compared event to $LiCoO_2$ [23].

1.1.5 Lithium-ion battery assemblies

The last subsection of lithium-ion battery fundamentals will be briefly discussed the different types of lithium-ion cell assemblies. As seen in Figure 1-4, lithium-ion batteries can come in multiple configurations, such as cylindrical, coin, prismatic, and pouch [19, 20].

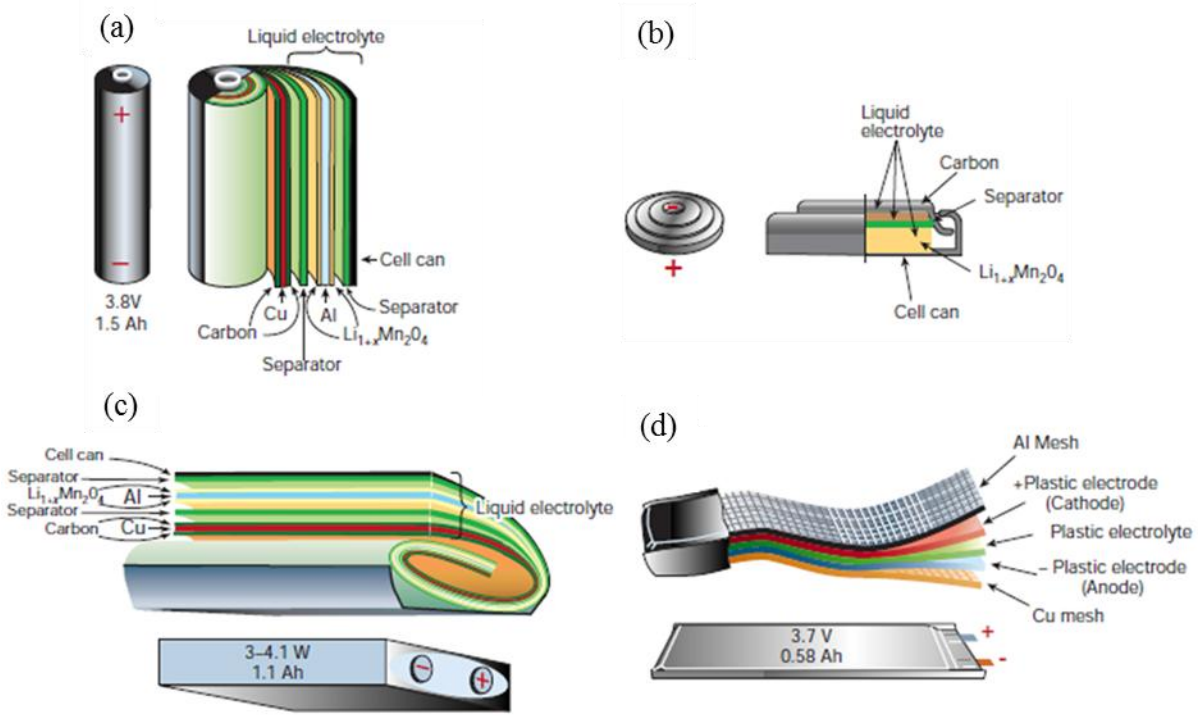

Figure 1-4: Types of assemblies of lithium-ion batteries: (a) cylindrical; (b) coin; (c) prismatic; (d) pouch [24]

While modern cylindrical cells can have superior energy density to prismatic and pouch cells, they do not pack as well; however, unlike prismatic or pouch cells they do expand with use [25]. Cylindrical cells are very popular in laptops, however they have also been in electric vehicle applications, as the Tesla Model S battery pack consists of thousands of Panasonic 18650 cylindrical cells [25, 26]. Coin cells are very small, and their uses are mostly in small electronics such as watches [25].

Prismatic cells are layered rather than wound about an axis like a cylindrical cell. This allows possibility for a thin cell with large surface area allowing for better thermal management as it is easier to minimize temperature gradients throughout the cell. The flat, rectangular shape also allows better packing compared to cylindrical cells [25]. These cells can be high capacity and are often used in electric vehicles [25]. Prismatic cells often use a welded aluminum enclosure [25].

The pouch is similar to the prismatic cell in both construction and uses, but with a flexible, lightweight enclosure, making it even more favourable for packing [25]. The downfall of the pouch cell is that it is very susceptible to swelling and becoming "puffy" over time [25].

1.2 Lithium-ion batteries: advantages and disadvantages

As mentioned earlier, Li-ion batteries are preferred due to their specific energy and energy density [20]. Comparing to other batteries such as nickel-cadmium and lead-acid, lithium-ion batteries show superior specific energy, and energy density [24, 27]. As well lithium-ion batteries tend to have a long cycle life, rapid charge capability, ability to discharge at high power and high rates, and no memory effect seen by other batteries [20].

Conversely, lithium-ion batteries do have some disadvantages. These include degradation at high temperature, and significant degradation with overdischarging and overcharging [20]. Possibly the highest concerns are with safety; thermal runaway can be triggered by very high temperatures, when the battery is overcharged, or when the battery is physically damaged [20]. Thermal runaway is a process where an exothermic reaction is accelerated by high temperature, leading to further increase in temperature; this can lead to fires and explosions of the battery [28]. As a result of these concerns battery management systems such as mechanical disconnects and thermal management systems must be used to protect against overdischarge, overcharge, and unfavourable thermal conditions [20].

1.3 Motivation for This Work

In order to further improve electric vehicles, studies must take place in order to gain knowledge and understanding that will aid in the design of future electric vehicles.

One of the technical challenges to be addressed is the degradation that batteries experience over their life. This degradation will be characterised by capacity fade; the reduction of available energy that a battery can supply per charge over its lifetime. A better understanding of how a battery's capacity reduces over time as a function of operational parameters such as cell temperature, thermal management, and voltage swing can provide insight on how best to utilise batteries in electric vehicles to result in superior performance over time. Notably, this will give great insight into the design of battery management systems, specifically thermal management systems.

1.4 Scope and Outline of Thesis

This report will focus on using AutoLionST, a numerical software package that utilizes MATLAB and Simulink, to characterise lithium-ion cells using numerical models, to study the capacity fade of lithium-ion cells used in electric vehicles. This degradation model will be tuned based on experimental results. This study will focus on 10Ah prismatic cells with NMC ($LiNi_{1/3}Mn_{1/3}Co_{1/3}O_2$) cathode active material, and graphite (C_6) anode material. The study will observe capacity fade using both more experimental load cases (i.e. different C-rates), and more realistic load cases (i.e. drive cycles).

The results of this thesis can be used by industry (specifically the industry partner which instigated this research) to evaluate and design thermal management systems based on expected capacity fade, and in the research community to better understand and quantify the factors affecting lithium-ion battery degradation.

The following are the objectives of the work presented in this thesis:

- To validate the model which is employed by AutoLionST through experimental work
- To study the effect of thermal management on lithium-ion battery capacity fade under different temperature conditions and discharge rates
- To study the effect of thermal management on lithium-ion battery capacity fade for realistic loading (drive cycles); and to determine if regenerative braking has any impact on capacity fade
- To study the effect of different drive cycles on heat generation and battery temperature increase

Chapter 1 of this thesis has presented the background of the expanding electric vehicle market, lithium-ion battery operational fundamentals, a short discussion of the materials used, and the purpose of this study. Chapter 2 will present a literature review of relevant work and findings regarding such topics as battery degradation mechanism, degradation modeling, characterisation of battery thermal management systems, and numerical modeling efforts. Chapter 3 will present the numerical model employed by AutoLionST. Chapter 4 will explain the methodology used throughout the study, both experimental and simulation based. Chapter 5 will present the experimental results. Chapter 6 will discuss the subsequent parameter adjustment with the using experimental data. Chapter 7 will present and discuss all key results of the simulation work. Lastly, Chapters 8 and 9 will present the important conclusions, and any applicable recommendations of how to proceed in future work, respectively.

2 Literature Review

This chapter of the thesis will present key literature which has been reviewed concerning lithium-ion batteries. This review can be sectioned into literature discussing lithium-ion battery degradation, thermal management systems, and lithium-ion battery modeling.

2.1 Lithium-ion battery degradation

The works reviewed include those which discuss and review the degradation mechanisms, those which model certain mechanisms, and those which explore capacity fade by experimental means.

In 1998, Arora et al. presented an extensive study detailing many processes and reactions leading to capacity fade in lithium-ion batteries, and how to incorporate them in future battery modeling [29]. They indicated that lithium-ion batteries undergo the most rapid capacity loss within the first few cycles, as a result these early cycles are seen as a period to condition the battery before use [29]. This capacity loss was attributed to the initial formation of a solid electrolyte interface (SEI) layer which forms on active particles of the carbon negative electrode [29]. In order to form this layer, active lithium is consumed following an electrolyte reduction reaction causing electrolyte decomposition; while lithium is consumed in this formation, the layer acts as a passivating film, greatly reducing further loss of lithium, and hence loss of capacity [29, 41].

Arora et al. also report that overcharging will result in side reactions which will significantly reduce battery capacity [29]. Overcharge processes can result in metallic lithium formation at the carbon negative electrode (yielding electrode material unusable), unwanted inert material such as Co_3O_4, $LiNi_2O_4$, Mn_2O_3 at the positive electrode causing loss of active material [29]. Overcharge can also have an effect on the electrolyte; high voltages from overcharge can cause oxidation of the solvent leading to decomposition of the electrolyte resulting in insoluble products, which not only consumes electrolyte, but also block pores in the electrode material [29]. As well, they discussed film formation at both electrodes, indicating a passive interfacial layer will form on electrodes, protecting the electrode material, even though it causes an initial loss of lithium [29]. Other mechanism discussed by Arora et al. include corrosion and pitting of aluminum and copper current collector, and dissolution of the positive electrode into the electrolyte [29]. Many of these mechanisms have been considered, and included in future modeling efforts.

In 2002, Ramadass et al. published a multiple works studying the capacity fade of lithium-ion batteries at elevated temperatures [30, 31]. In the first of these studies, they cycled Sony 18650 cells ($LiCoO_2$ cathode, carbon anode) at elevated temperatures (in the range of room temperature to 55˚C, performing charging and discharging between 2.0V and 4.2V [30]. They found that cells at elevated temperatures showed higher capacity during early performance compared to cells cycled at room temperature, but over time, all cells aged more rapidly with higher temperature [30]. They also found that cell resistance increased with cycling and more rapidly at higher temperatures; however, cells with higher temperature initially exhibited lower resistance [30]. Both these results were attributed to the continued growth of the SEI layer on the anode during cycling at elevated temperature due to lithium loss and film growth causing

decreased capacity and increased impedance at the anode [30]. They did however note that at room temperature and 45˚C cell resistance increased primarily due to increased impedance at the cathode [30]. They also showed that cycling causes decreased rate capability. This means cycled cells, especially at high temperatures, will show considerably worse discharge capacity when discharged at higher C-rates (1C) oppose to a lower C-rate of C/9 [30]. These effects were attributed to dissolution of unwanted products in the electrolyte causing a decrease of transference number, and an increase of lithium-ion intercalation resistance [30]. The capacity fade results captured by Ramadass et al. are depicted in Figure 2-1.

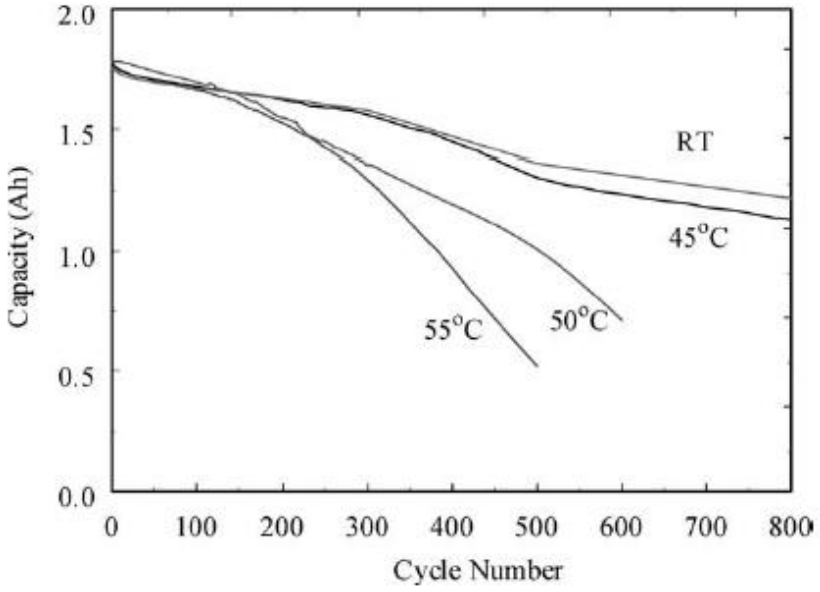

Figure 2-1: Results captured by Ramadass et al. [30] showing capacity of Sony 18650 cells after cycling at different temperatures

In the second part of the study, Ramadass et al. studied the causes of capacity fade more closely [31]. Loss of capacity was attributed to three main factors, decrease in rate capability, loss of active lithium, and loss of active electrode materials [31]. In the study, batteries were cycled by discharging them at 1A (~0.56C). However, due to a decrease of rate capability with cycling, discharge capacity would be higher at lower discharge rates; hence some loss of discharge capacity can be attributed to the current level at which the cells were discharged [31]. Ramadass et al. were able to estimate capacity fade for each of these phenomena; it is shown that with the exception of the cell cycled at 150 cycles (oppose to 300 and 800 cycles) at room temperature, capacity fade can primarily be attributed to loss of electrode active material, and these effects are amplified with high cycling [31]. Loss of active lithium is the second highest contributor to capacity fade; both loss of active lithium and losses due to rate capability contribute less at high cycles [31].

In 2005, Vetter et al., published a paper summarizing a multitude of ageing mechanism in lithium-ion batteries [39]. They effectively discussed many of major ageing mechanisms at the anode and cathode, their causes, effects, and methods of mitigation. The anode mechanisms

which they attribute to capacity fade include: electrolyte decomposition resulting in SEI growth which is enhanced at high temperatures, cracking particles enhanced by overcharge, detached active material particles due to volume changes enhanced by cycling, decomposition of the electrode binder enhanced at high temperatures, and plating of metallic lithium which is enhanced at low temperatures [39]. While many of these mechanisms have already been discussed in this review, the most important mechanism to note is lithium plating, as it is the only mechanisms listed which is enhanced at low temperatures [39]. This enhancement of lithium plating at low temperatures can be attributed to slow lithium-ion diffusion through carbon particles and slow lithium-ion diffusion through the electrolyte, causing plating or dendritic growth [39].

Vetter et al., separated their discussion of cathode ageing mechanism into those occurring in nickel-cobalt based cathodes, and those occurring in manganese based cathodes. They noted that cathodes constructed with nickel-cobalt oxides tend to not experience dissolution unless charged to too high a potential (4.2V versus Li/Li^+); even charged passed this limit only cobalt oxides experience a small amount of dissolution [39]. They did however note that nickel-cobalt cathodes are susceptible to film formation as a result of electrolyte oxidation and decomposition of $LiPF_6$ (the electrolyte salt) [39]. Unlike nickel-cobalt cathodes, it is reported that manganese cathodes are prone to dissolution where active manganese (Mn(III)) is lost; some of this material (Mn(II)) is soluble in the electrolyte and may deposit on the anode, while other material (Mn(IV)) remains at the cathode in solid form [39]. Later in this review the work by Cai et al. is discussed where they model degradation using the manganese dissolution mechanism [35].

In 2011, Smith et al. experimentally studied the growth of SEI under different conditions of lithium-ion coin cells [36]. In their study, cells produced composed of different weight ratios (i.e. increasing the amount of active material in the electrode, while reducing the quantity of binders and carbon black, a conductive agent) and were tested at different temperatures of 30, 40, and 50˚C, and at different (but relatively low) charge/discharge currents of C/26, C/24, C/20, and C/10; all cells were cycled between 0.005V and 1.2V [36]. They concluded that time (as opposed to cycle count) and temperature are the main contributors to SEI growth [36]. However, it should be noted that at high C-rates (unlike those used in this study) resulting in lower discharge/charge time, there would be significant heat generation which would lead to temperature rise and enhanced SEI formation [36]. Another important conclusion is that since SEI growth is continuous (not just limited to the first few cycles), decreasing the negative electrode surface area can reduce the development of SEI [36].

Also in 2011, Amine et al. further studied capacity fade mechanisms, specifically of a lithium-ion cell with a NMC ($Li_{1.1}[Ni_{1/3}Mn_{1/3}Co_{1/3}]_{0.9}O_2$) cathode and graphite anode at elevated temperatures [38]. Figure 2-2 below shows their capacity fade results for a coin cell discharged and charged at 1C with a voltage range of 3.0V and 4.0V, at room temperature and 55˚C [38]. They concluded that the main cause for degraded performance is dissolved metals from the cathode depositing on the anode, and suggested using an electrolyte additive to mitigate this degradation [38].

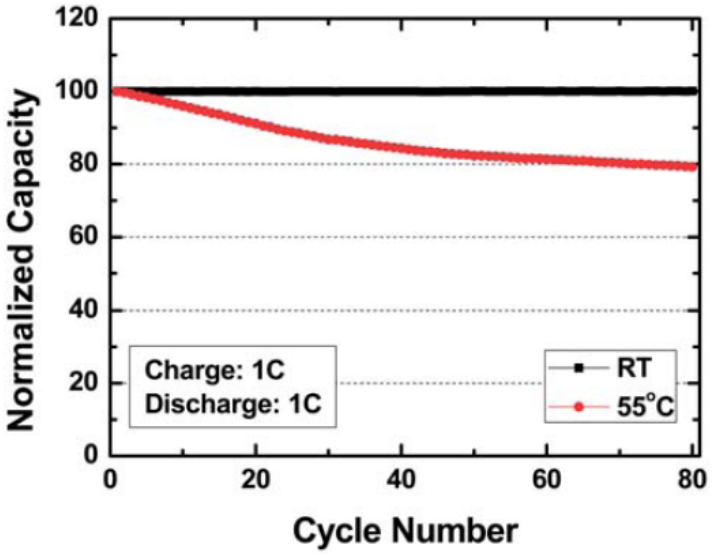

Figure 2-2: Results found by Amine et al. [38] showing capacity fade of coin lithium-ion cells at different temperatures

In 1990, Bro and Levy published a book titled *Quality and Reliability Methods for Primary Batteries* [40]. In it they suggested a very early and simple model to describe the loss of battery capacity over time; note that this model did not directly take into account any degradation mechanisms but was merely based on an Arrhenius relation [40]. They suggested multiple models for different conditions, but their model of most relevance to this work describes capacity fade with an acceleration factor, taking temperature into account; this model is shown in Equation (7) below [40]:

$$c(t,T) = c_0 - k_0 t e^{-\frac{E}{RT}} \tag{7}$$

In the above equation, c denotes capacity for a battery discharged for a given time period at a given temperature, with an initial capacity of c_0 [40].

In 2002, Ramadass et al. discussed a semi-empirical model to predict capacity fade [37]. Using experimental data from previous work, they fit experimental discharge curves to a first principles model, and developed semi-empirical correlations to describe capacity fade [37]. Semi-empirical relations for state of charge and film resistance were developed; the relation for film resistance (as a function of cycling) is used in the first principles model to predict capacity fade behaviour with cycling [37].

In 2004, Ramadass et al. also published work describing a first principles capacity fade model with the intention of studying the effect of parameters on capacity fade [32]. In this study, the only capacity fade mechanism considered is SEI layer formation as a result of a side reaction which consumes solvent and lithium-ions [32]. This side reaction is only considered during charge periods as this is when lithium-ions intercalate into the carbon active material, causing volume increase, leading to damage to the passive SEI layer, and hence greater exposure to the

unprotected carbon active material [32]. In this model, this ageing mechanism is described by relating the change in thickness of the passive film to the transfer current density for the side reaction, which is found through use of a simplified Butler-Volmer expression; the thickness of the passive film is then used to calculate the resistance of this film [32]. This approach will be more thoroughly explained in Chapter 3 of this thesis, describing model development. This work proceeded to study the effect of select parameters on capacity fade; one important conclusion showed that cells cycled while charged to lower voltages (denoted as EOCV, end of charge voltage) demonstrate less capacity fade [32]. In this study EOCVs of 3.9, 4.0, and 4.2V were employed [32].

Similar to Ramadass et al., in 2012 Vazuqez-Arenas et al. also developed a model incorporating capacity fade effects incorporating two key extensions [33]. Firstly, they incorporated thermal effects into their model by including heat generation due to reaction, joule, and entropic heating [33]. Secondly, they included an additional ageing mechanism, namely the dissolution of active cathode material (in this study $Li_yMn_2O_4$) leading to volume changes at the positive electrode [33].

A more detailed model including capacity fade due to SEI film formation was created by Deshpande et al. in 2012 [34]. Their model couples chemical reactions which lead to loss of capacity with fatigue mechanisms which lead to continued SEI growth and degradation [34]. They modeled degradation solely based on continuous SEI film formation which occurs as a result of physical damage due to diffusion induced stresses (DIS) caused by cyclic volume changes leading to fatigue and cracking at the particle surface of active negative electrode material [34]. These cracks at the particle surface expose new active material, leading to further SEI layer growth [34]. This model describes the development of DIS during cycling as a result of volume change, crack propagation using Paris Law, and subsequent SEI layer growth [34]. Deshpande et al. were successful in their ability to accurately model degradation of a $LiFePO_4$ battery; Figure 2-3 shows their results compared to experimental work. Note that the results in Figure 2-3 depicts capacity fade of $LiFePO_4$ lithium-ion batteries charged and discharged at C/2, with 90% DOD (cut-off voltages of 3.6V and 2.0V) [34].

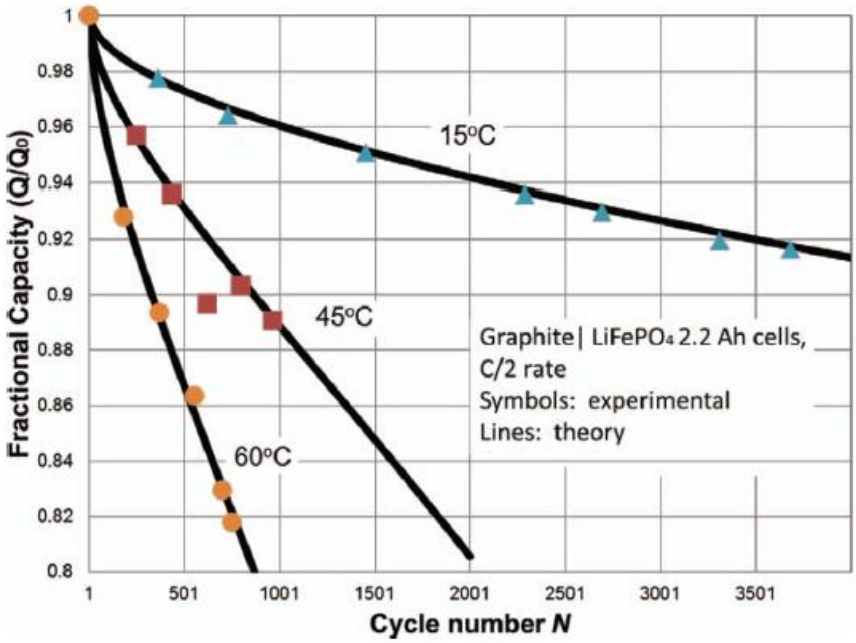

Figure 2-3: Results by Deshpande et al. [34] showing normalized capacity over cycling for multiple cell temperatures

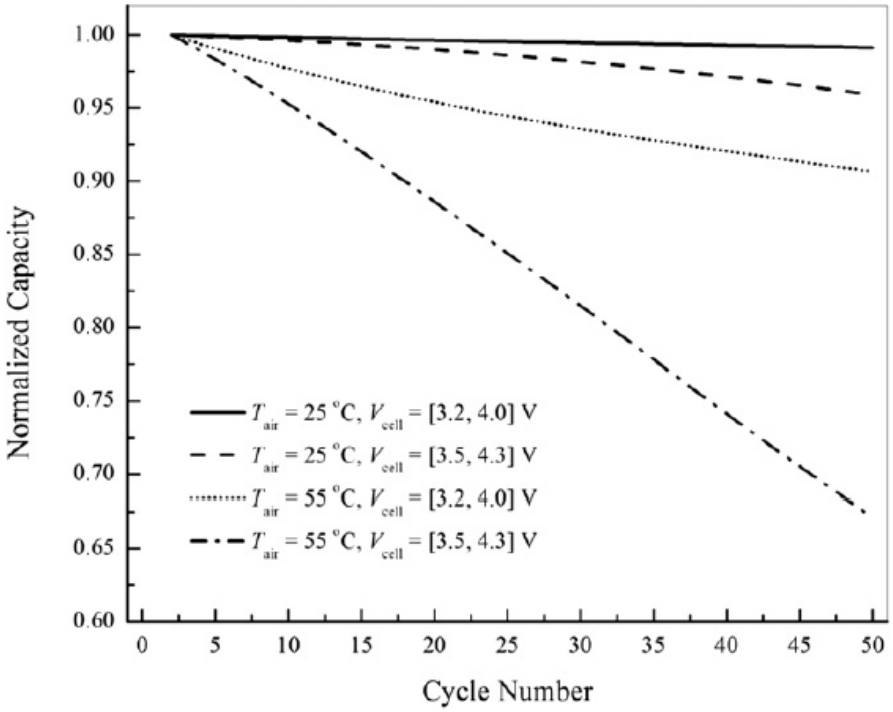

Figure 2-4: Results from Cai et al. [35] showing normalized capacity of a battery after cycling under a four different conditions

In 2013, Cai et al. published work again discussing the modeling of battery lifetime performance focusing on degradation at the cathode [35]. Specifically, they studied the dissolution of Mn of a $LiMnO_2$ cathode; in their model, capacity loss occurs due to loss of active Mn, and formation of a resistive film on cathode particles [35]. The dissolution reaction of Mn(III) (the active phase) creates two phases; Mn(II) and Mn(IV); Mn(II) dissolves into the electrolyte and may transfer to and deposit on the anode leading to anode degradation, while solid and inert Mn(IV) remains at the cathode forming a film around the active material [35]. Both of these also lead to direct loss of useable Mn at the cathode [35]. This dissolution is modeled by calculating the changing volume of cathode material particles as active material is lost to the electrolyte, and also calculating the changing volume of active material within these particles as a resistive film develops [35]. Figure 2-4 shows the capacity fade results obtained by them for two different temperatures and two different voltage ranges. Note all these results are for a battery with a $LiMn_2O_4$ cathode, discharged and charged at 2C, at the given conditions shown in Figure 2-4.

2.2 Battery thermal management systems

This subsection will discuss works reviewed which focused on thermal management systems of batteries. This literature mostly included papers which describe a model which has been developed to model heat generation, and study the resulting temperature rise, temperature profiles, and/or heat dissipation.

In 1994, Chen and Evans developed an early two-dimensional thermal model to describe lithium-ion batteries [42]. This model used conservation of energy, and assumed uniform heat generation throughout the battery domain, using a calculation for battery heat generation published by Bernardi et al. [50]; in this model the only sources of heat generation are Joule heating and entropic heating [42]. This calculation can be seen in Equation (8) [42]:

$$q = \frac{N_{cell} i \left(E_{oc} - V - T \frac{dE_{oc}}{dT} \right)}{LX} \tag{8}$$

In the above equation, q is the volumetric heat generation, N_{cell} is the number of cells in the stack, i is the current density (A/cm^2), E_{oc} is the open circuit voltage of a single cell, V is the cell voltage, T is the battery temperature, and LX is the thickness of the stack [42].

They studied the effect of cell geometry, dimensions of different stack components, different discharge rates, and different cooling rates on battery temperature (and temperature profile) [42]. Figure 2-5 shows two of their key results of interest; (a) maximum cell temperature due to different C-rates, and (b) temperature profile throughout the battery at the end of discharge for a variety of heat transfer coefficients [42].

In the above figure, Chen and Evans were able to show significant temperature increase can occur as a result of discharge rate, and that this heat generation can be countered by effective cooling, although depending on the size of the stack, internal temperature may be relatively unchanged [42].

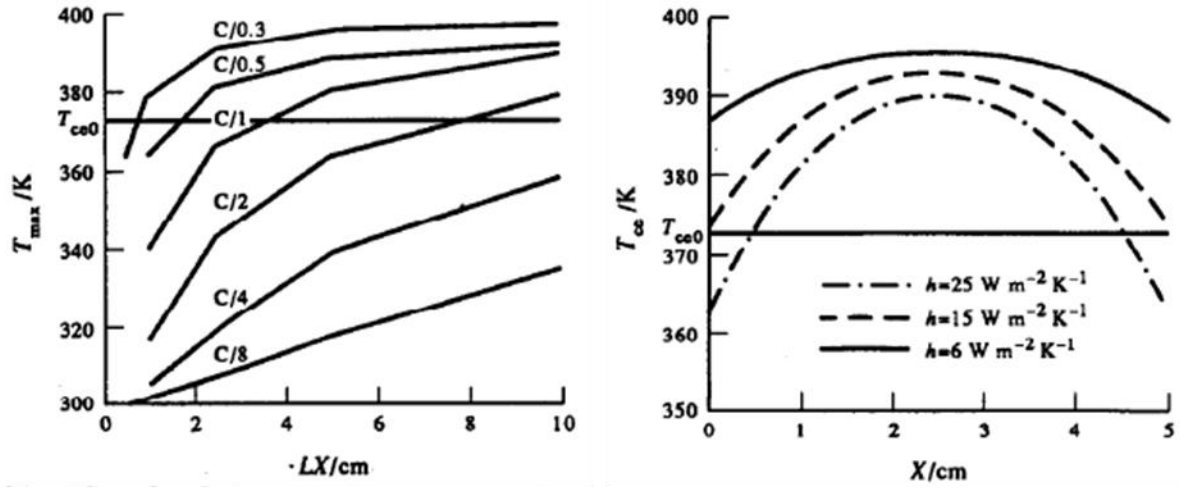

(a) (b)

Figure 2-5: Results from Chen and Evans [42] depicting: (a) maximum temperature reached by cells discharged at different C-rates and different stack sizes; (b) temperature profiles in cells at the end of discharge for different heat transfer coefficients

In 1996, Chen and Evans continued mathematical modeling on battery performance. They reported heat generation in the battery for a variety of C-rates, as well as further temperature results showing the effect of different cooling rates at different discharge rates [43]. It was shown that at normal discharge rates, high heat transfer rates are effective at removing heat from the entire stack [43]. At the same time, with high discharge rates, internal stack temperature remains high even with high cooling rates, instead resulting in much steeper temperature gradients at the stack boundaries [43]. These results can be seen in Figure 2-6.

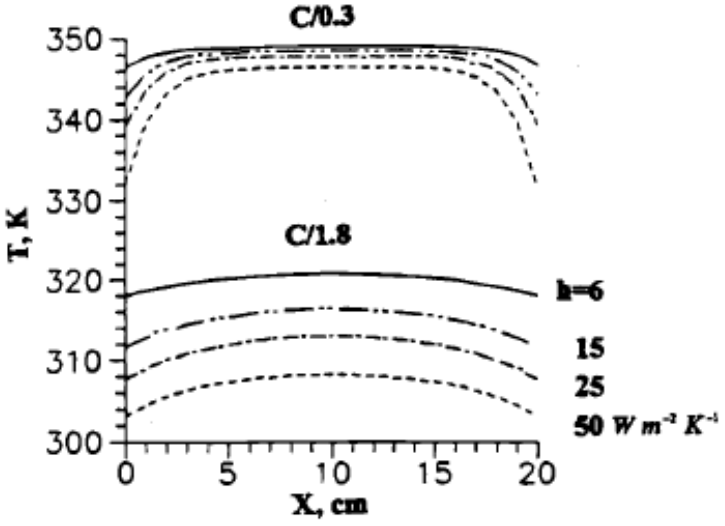

Figure 2-6: Results by Chen and Evans [43] showing temperatures profiles in battery stacks at the end of discharge for different discharge rates and heat transfer coefficients

Al Hallaj et al. has also used a thermal model to simulate battery performance; their model used experimental heat generation data for Sony 18650 cells from cells discharged at rates of 1C, C/2, C/3, and C/6 [44]. This heat generation data was also used to extrapolate heat generation data for cells at higher discharge rates (2C) [44]. Using the heat generation data, simulations were also performed to quantify increase of cell temperature over time for different discharge rates and different cooling rates [44]. Similar results were shown by Chen and Evans [43]. Additionally, they studied the onset of thermal runaway for batteries at different OCVs [44]. Similar to Chen and Evans [43], they also concluded that enhanced cooling provides the capability to lower overall battery temperature, but also increases temperature gradients in the cell [43, 44]. They also indicated that thermal runaway is a distinct possibility with high discharge rates (1C) and low cooling rates [44].

While the previously mentioned studies considered heat generation from just a battery or battery pack, in 2002 Maleki and Shamsuri developed a thermal model of a notebook computer battery pack, including heat generation from electrical components used for battery management [45]. They calculated battery heat generation from experimental data using the same method as Chen and Evans [42], considering only Joule heating and entropic heating [45]. They also assigned heat generation to each electrical component equal to I^2R, for each component where I is the current used by each component and R is the resistance of each component [45]. They were able to show that heat production is dominated by battery heat generation during discharge, while during charge periods it is governed by heat dissipation from electronics [45].

In addition to these modeling efforts to understand heat generation in batteries and the resultant thermal effects, research has taken place in the development of different thermal management strategies. In 2004 Khateeb et al. designed a thermal management system employing a phase change material (PCM) to manage the heat generated by an electric scooter [46]. PCM is a passive cooling method (opposed to active methods such as air or liquid cooling). They found that PCM alone is not an effective cooling system due to low thermal conductivity leading to possible thermal runaway [46]. However, using aluminum foam for good conductivity with PCM, and external aluminum fins, they showed that the battery temperature remained sufficiently low even over long periods of use, meaning PCM is a promising method of battery thermal management [46].

In 2005, Mills and Al-Hallaj, did similar work to Khateeb et al. [46], in simulating a battery pack of Sony 18650 cells using a passive battery thermal management system [47]. In their simulations they used a PCM composite material made of a PCM with an expanded graphite (EG) matrix [47]. This PCM/EG composite addressed the issue of low thermal conductivity of the PCM, which Khateeb et al. solved through use of aluminum foam [46, 47]. For a given battery pack they were able to determine the required volume of PCM/EG needed to keep the battery pack below their maximum allowable temperature of 55°C [47]. They showed that for their most intense case, drawing 6.6W of power from a battery pack of 6 cells, the required volume of PCM/EG was 106.82 cm^3 to ensure no local temperature of the pack exceeded 55°C [47]. They also showed that using a PCM with ideal yet realistic properties attained by

advanced manufacturing methods will greatly reduce the volume of PCM/EG to 59.53 cm^3 for the conditions same conditions [47].

To further study the use of a PCM thermal management system, in 2008 Sabbah et al. performed simulations to compare a passive thermal management system employing a PCM, to an active thermal management system using blowing air [48]. It was shown that even compared to moderate Reynold's number airflow, a PCM based thermal management system can provide superior cooling and temperature uniformity throughout the batteries; the passive management system is especially useful in situations with high ambient temperature or high discharge rates [48]. Figure 2-7 below shows some of results.

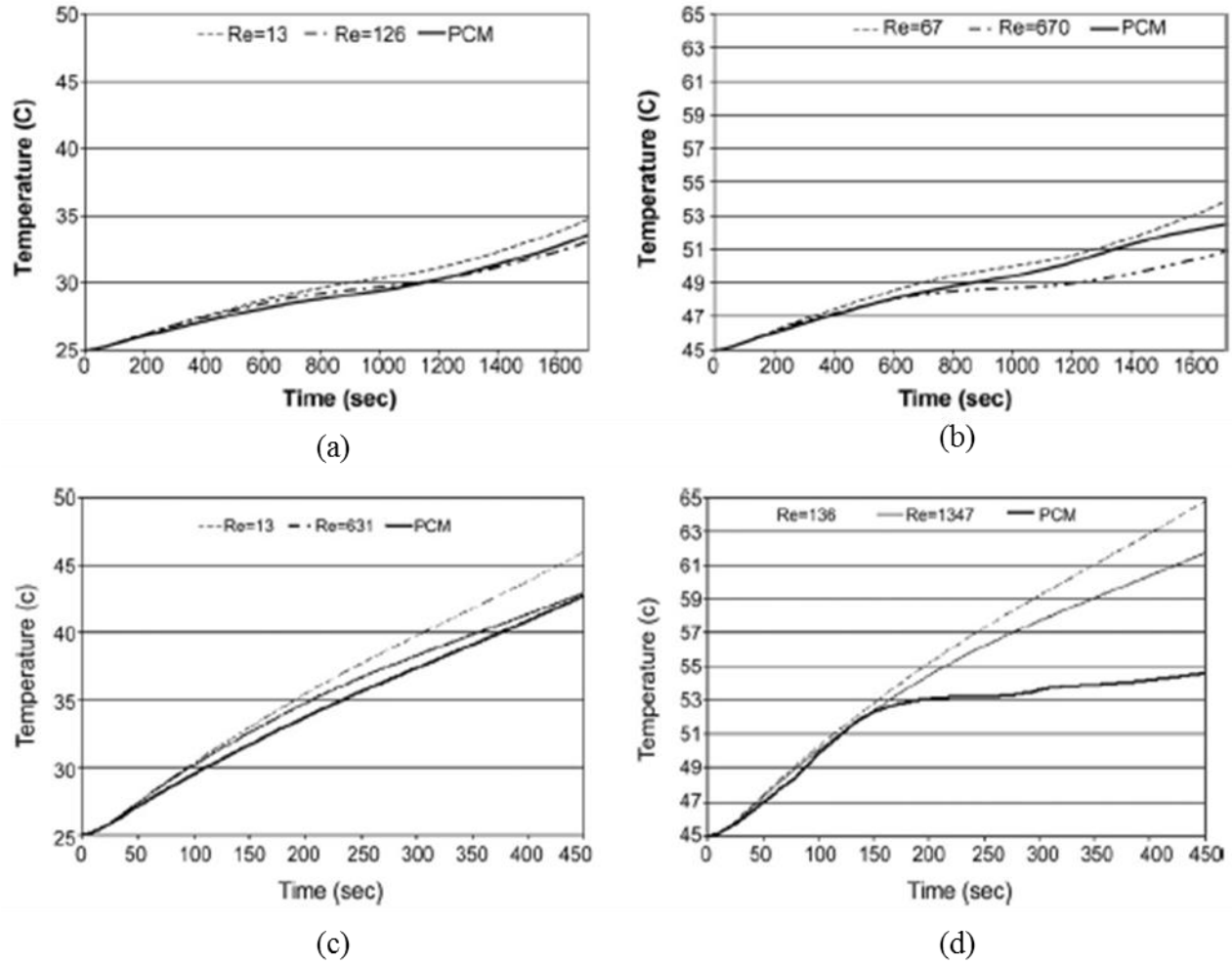

Figure 2-7: Results from Sabbah et al. [48] depicting battery pack temperature rise with varying Reynold's number, discharge rates and ambient temperature: (a) 2C, 25°C; (b) 2C, 45°C; (c) 6.67C, 25°C; (d) 6.67C, 45°C

Finally, in 2012 Karimi and Li simulated the thermal management of a battery pack for electric vehicle applications [49]. They simulated a battery pack of 20 batteries with cooling ducts on either side of the pack and investigated the use of different cooling methods to manage

temperature and voltage variation between batteries in the pack; natural convective cooling, forced convective cooling (with air and liquid), and a PCM were all used [49]. It was found that enhanced cooling will cause large variation in temperature and voltage between batteries in the pack; the temperature of batteries at the centre of the stack were unaffected by changes in cooling strategy [49]. Figure 2-8 below depicts some of their results.

It was concluded that a more effective cooling strategy should employ multiple cooling ducts with smaller channels (oppose to just cooling ducts at the ends of the pack) to be distributed throughout the pack [49].

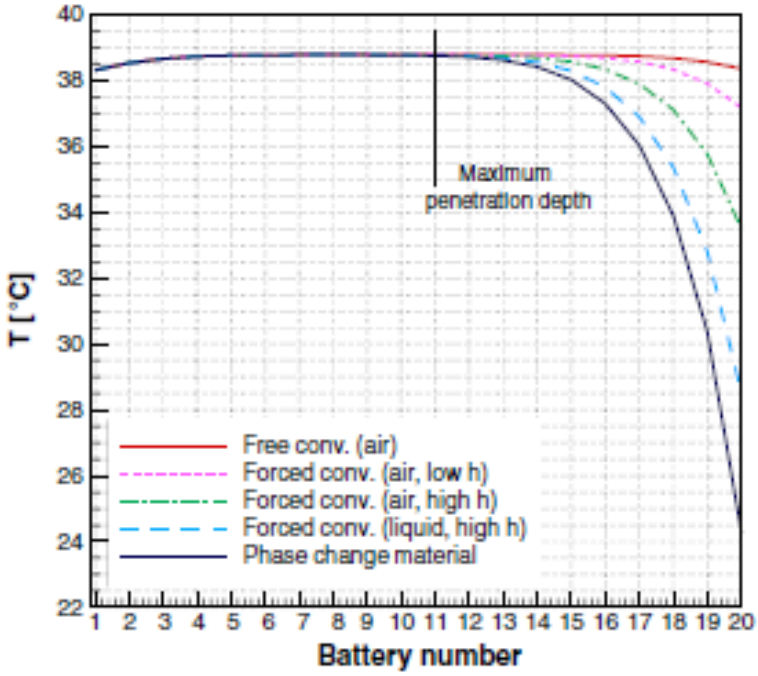

Figure 2-8: Results from Karimi and Li [49] showing temperature distribution in a battery pack after being discharged at 2C while varying thermal management strategy

2.3 Gap in Literature

As shown, there have been many efforts to better understand lithium-ion battery degradation, and some effects of thermal management. The first evident gap in literature is the lack of research directly linking choice of thermal management system to the effect it could have on degradation. This work will look to employ the methods used to model battery degradation mechanisms to characterize capacity fade under a variety of operating conditions to demonstrate the usefulness of battery thermal management (and when effective thermal management is most important). This work will also present simulations aiming to reflect real life driving conditions, and characterize the subsequent battery ageing in an attempt to justify the importance of effective thermal management in today's electric vehicles.

3 Model Formulation

In this chapter, the mathematical model for the capacity and performance of a lithium-ion battery is formulated, involving the fundamental lithium-ion intercalation/deintercalation reactions being modeled at the electrodes, all the governing equations being applied to the problem, the side reactions describing the ageing mechanisms, and the corresponding modeling of these ageing mechanisms.

The physical problem modeled is the operation of a lithium-ion battery subject to some form of cycling using specified discharge and charge profiles, and the subsequent battery degradation that occurs as a result. Like some of the works described in the literature, this model takes thermal effects into account when considering the operation of degradation of the modeled battery [33, 34, 35, 40]. The simulation work will entail operating a battery under set conditions, while varying parameters to observe battery degradation, quantified by loss of capacity. Mathematically, this requires solving the governing equations, and degradation mechanisms associated with the key chemical reactions occurring during battery operation. AutoLionST is a numerical software package which gives the user the ability to design a battery, and simulate its performance using a Simulink environment [57]. It should be noted that AutoLionST is largely based on the initial works of Doyle et al. [51], and the subsequent work by Fang et al. [52], Gu and Wang [53], Wang and Srinivasan [54], and Smith and Wang [55]. AutoLionST works by solving the governing equations describing the intercalation and deintercalation reactions at the electrodes of the cell, and the subsequent degradation mechanisms [57].

3.1 Lithium Insertion Reactions

The general reaction of intercalation/deintercalation of lithium-ions at the negative electrode of a lithium-ion cell was presented in Chapter 1. As modeled by AutoLionST, for a lithium-ion battery with a negative electrode active material of graphite the reactions at the negative electrode are as follows [57]:

$$Li_xC_6 \rightleftharpoons C_6 + x\,Li^+ + x\,e^- \tag{9}$$

Where the forward reaction represents the deintercalation of lithium-ions from graphite structure (during discharge), and the backward reaction represents the intercalation of lithium into the graphite structure (during charge).

The general reaction of intercalation/deintercalation of lithium-ions at the negative electrode of a lithium-ion cell has also been presented in Chapter 1. As mentioned in the scope section of Chapter 1, this study will simulate batteries featuring nickel-manganese-cobalt (NMC) oxide cathodes. For an NMC oxide positive electrode, the reactions at the positive electrode are as follows [57]:

$$Ni_{1/3}Mn_{1/3}Co_{1/3}O_2 + y\,Li^+ + y\,e^- \rightleftharpoons Li_yNi_{1/3}Mn_{1/3}Co_{1/3}O_2 \tag{10}$$

Where the forward reaction represents the intercalation of lithium into the NMC structure (during discharge), and the backward reaction represents the deintercalation of lithium-ions (during charge).

3.2 Assumptions and Mathematical Domain

Before the model equations are presented, there are two very key assumptions used in the development of this model:

i. A lumped thermal model is used, in that it is assumed the entire cell is at a uniform temperature, and there is only variation in time [52, 57]
ii. Uniform current distribution, concentrations, and overpotential are assumed over the cell height [52, 54]
iii. The only reactions occurring are the intercalation/deintercalation reactions at each electrode, and side reactions resulting in film growth

Figure 3-1 shows a good example of the domain used in solving the governing equations as shown by Fang et al. [52]. Note that this domain is 1-D through the thickness of the cell (*x-direction*), and also 1-D through the radial direction of electrode active material particles. As mentioned previously, there is no temperature variation throughout this domain.

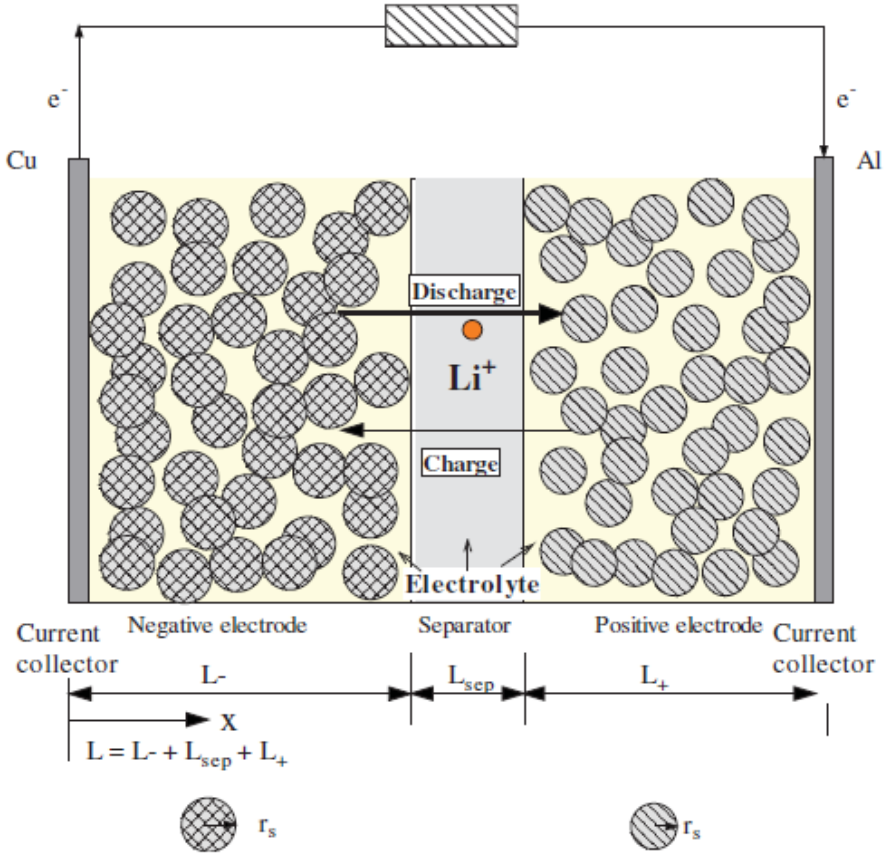

Figure 3-1: 1-D lithium-cell domain used in modeling as presented by Fang et al. [52]

3.3 Governing Equations

The governing equations used to describe the domain are the solid-phase conservation of charge, electrolyte-phase conservation of charge, electrolyte-phase Li^+ species concentration, the active material Li species conservation, the conservation of energy, and the Butler-Volmer equations (at each electrode) [57]. These equations are shown below:

Solid-phase conservation of charge and corresponding boundary conditions [52, 57]:

$$0 = \frac{\partial}{\partial x}\left(\sigma_s{}^{\text{eff}}\frac{\partial \emptyset_s}{\partial x}\right) - j^{\text{Li}} \tag{11}$$

$$-\sigma_{s_-}{}^{\text{eff}}\frac{\partial \emptyset_s}{\partial x}\bigg|_{x=0} = \sigma_{s_+}{}^{\text{eff}}\frac{\partial \emptyset_s}{\partial x}\bigg|_{x=L} = \frac{i}{A} \tag{12}$$

$$\frac{\partial \emptyset_s}{\partial x}\bigg|_{x=L_-} = \frac{\partial \emptyset_s}{\partial x}\bigg|_{x=L_-+L_{sep}} = 0 \tag{13}$$

In the above equations, $\emptyset_s$ represents the electrical potential in the solid phase with units of *V*, j^{Li} is the volumetric electrode current from all reactions with units of A/m^3, and $\sigma_s{}^{\text{eff}}$ is the effective electrical conductivity of the given material (different for anode and cathode) [52, 57]. $\sigma_s{}^{\text{eff}}$ is an effective electrical conductivity adjusting for the tortuous electrode using a Bruggeman relationship; the Bruggeman expression can be seen below [52]:

$$\sigma_s{}^{\text{eff}} = \sigma\varepsilon_s{}^{n} \tag{14}$$

In the above equation, σ is the uncorrected electrical conductivity of the solid, ε_s is the volume fraction of material in the solid phase, and *n* is the Bruggeman exponent, normally taken to be 1.5 [52].

Equation (11) essentially describes the distribution of charge throughout the solid electrode, subject to some electrical production (or consumption) as a result of electrochemical reactions. Boundary Condition (12) indicates that the charge gradient at the boundary between the electrode material and current collector is linearly related to the current drawn from the battery. Boundary Condition (13) indicates that the gradient of charge in the solid material is zero at either side of the separator, implying that no charge transfers through the separator via a solid phase. Note that solid-phase conservation of charge is applied separately at each of the electrodes.

Electrolyte-phase conservation of charge and boundary conditions [52, 57]:

$$0 = \frac{\partial}{\partial x}\left(\kappa^{\text{eff}}\frac{\partial \emptyset_e}{\partial x}\right) + \frac{\partial}{\partial x}\left(\kappa_D{}^{\text{eff}}\frac{\partial \ln(c_e)}{\partial x}\right) + j^{\text{Li}} \tag{15}$$

$$\frac{\partial \emptyset_e}{\partial x}\bigg|_{x=0} = \frac{\partial \emptyset_e}{\partial x}\bigg|_{x=L} = 0 \tag{16}$$

In the above equations, $\emptyset_e$ represents the electrical potential in the electrolyte phase with units of *V*, c_e is the lithium-ion concentration measured in mol/cm^3, κ^{eff} is the effective ionic

conductivity of the electrolyte, and κ_D^{eff} is the effective electrolyte diffusional conductivity (both being corrected by a Bruggeman expression) [52, 57]. An expression for κ (the uncorrected ionic conductivity) was suggested by Doyle et al. [58], and used by Fang et al. [52] for an electrolyte composed of 1.2M $LiPF_6$ salt in a solvent mixture of ethylene carbonate (EC) and dimethyl carbonate (DMC) (note that the only difference in the AutoLionST model is the inclusion of ethylene methyl carbonate (EMC)) [52, 58]:

$$\kappa = 4.1253 \times 10^{-4} + 5.007c_e - 4.7212 \times 10^{3}c_e{}^{2} + 1.5094 \times 10^{6}c_e{}^{3} - 1.6018 \times 10^{8}c_e{}^{4} \quad (17)$$

After correcting the above expression using a Bruggeman expression, it can be used to find κ_D^{eff} according to the following expression suggested by Doyle et al. [51] and used by Fang et al. [52]:

$$\kappa_D{}^{eff} = \frac{2RT\kappa^{eff}}{F}(t^0{}_+ - 1)\left(1 + \frac{d\ln(f_\pm)}{d\ln(c_e)}\right) \quad (18)$$

R, T, and F are the universal gas constant, temperature, and Faraday's constant respectively, while $t^0{}_+$ is the transference number for lithium-ions in the electrolyte [52]. The transference number is the ratio of charge carried by a given ion species in a given electrolyte; an accepted value for the transference number of lithium-ions in an electrolyte with $LiPF_6$ salt is 0.38 [59].

Since c_e is not dimensionless, the units of the above coefficients are quite complicated, however performing a Taylor-series expansion on $ln(c_e)$ from Equation (15) would show that after neglecting higher-order terms, the units of each group of terms does indeed return A/m^3.

Note that j^{Li} appears in both Equations (11) and (15), however is opposite in sign; this implies that this quantity, j^{Li}, is transferred between the solid and electrolyte phase through electrochemical reactions. j^{Li} is calculated using a Butler-Volmer equation. This will be discussed later.

Similar to Equation (11), Equation (15) describes the distribution of charge throughout the electrolyte phase. In the solid phase, charge is transferred via electrons; however, in the electrolyte phase, charge is transferred through the movement of ions so the distribution of charge is also influenced by the concentration gradient of lithium-ions (as is expressed in the second term of Equation (15)). Boundary Condition (16) indicates that the charge gradient at the boundary between the electrolyte and current collector is zero, indicating that charge is not transferred directly from the current collectors to the electrolyte (or vice versa). Note the electrolyte-phase conservation of charge is solved continuously from throughout the entire domain, including through the separator.

Electrolyte-phase Li^+ species conservation, boundary and initial conditions [52, 57]:

$$\frac{\partial(\varepsilon c_e)}{\partial t} = \frac{\partial}{\partial x}\left(D_e{}^{eff}\frac{\partial c_e}{\partial x}\right) + \frac{1 - t_+{}^0}{F}j^{Li} \quad (19)$$

$$\left.\frac{\partial c_e}{\partial x}\right|_{x=0} = \left.\frac{\partial c_e}{\partial x}\right|_{x=L} = 0 \tag{20}$$

$$c_e(t=0) = {c_e}^0 \tag{21}$$

In the above equation, ε is the volume fraction of lithium in the electrolyte phase, and ${D_e}^{eff}$ is the electrolyte diffusion coefficient corrected using a Bruggeman coefficient measured in m^2/s; all other parameters and variables have been shown in other equations [52, 57]. Equation (19) describes the distribution of lithium-ion concentration as it changes over time as a result of electrochemical reactions. The last term in Equation (19) describes the production (or consumption) of lithium-ions as of result of reactions at the electrodes. The boundary condition implies that lithium-ions cannot diffuse through the current collectors.

Li species conservation (in particle radial direction), boundary and initial conditions [52, 57]:

$$\frac{\partial c_s}{\partial t} = \frac{1}{r^2}\frac{\partial}{\partial r}\left(D_s r^2 \frac{\partial c_s}{\partial r}\right) \tag{22}$$

$$\left.\frac{\partial c_s}{\partial r}\right|_{r=0} = 0 \tag{23}$$

$$-D_s \left.\frac{\partial c_s}{\partial r}\right|_{r=r_s} = \frac{j^{Li}}{a_s F} \tag{24}$$

$$c_s(t=0) = {c_s}^0 \tag{25}$$

In these equations, c_s is the concentration of lithium in the solid phase (electrode material) measured in mol/cm^3, D_s is the lithium diffusion coefficient in the solid, a_s is the specific interfacial area of an electrode calculated below [52, 53, 57]:

$$a_s = \frac{3\varepsilon_s}{r_s} \tag{26}$$

These equations describe the distribution of lithium in the electrode particles, through the radial direction, as it changes with time due to electrochemical reactions. Boundary Condition (23) is a symmetry condition applied at the centre of the particle, and Boundary Condition (24) describes the process of lithium-ions being consumed (or produced) at the particle boundary causing lithium to be inserted (or removed) from the electrode material as a result of electrochemical reactions.

Conservation of energy and initial condition [57]:

$$\frac{\partial(\rho C T)}{\partial t} = \left(q_r + q_j + q_c + q_e\right)A_{cell} - h_{conv}A_s(T - T_{amb}) \tag{27}$$

$$T(t=0) = T^0 \tag{28}$$

As mentioned earlier, the conservation of energy for the battery only takes into account temporal variation, with no discretization in space. In this equation, there are four heat generation terms, q_r, q_j, q_c, and q_e. They represent the heat due to reaction, joule heating, heat

due to contact resistance, and entropic heating respectively [52, 57]. ρ, C, and T are the battery density, heat capacity, and temperature, respectively. A_{cell} is the cell cross-sectional area normal to the thickness of the cell, A_s is the external surface area of the battery, h_{conv} is the convective heat transfer coefficient, and T_{amb} is the ambient temperature with which convective heat transfer occurs. The first three heat generation are calculated as shown below; note that they all have units of W/m^2 [52]:

$$q_r = \int_0^L j^{Li}(\emptyset_s - \emptyset_e - U)\,dx \tag{29}$$

$$q_j = \int_0^L {\sigma_s}^{eff}\left(\frac{\partial \emptyset_s}{\partial x}\right)^2 + \kappa^{eff}\left(\frac{\partial \emptyset_e}{\partial x}\right)^2 + {\kappa_D}^{eff}\left(\frac{\partial \ln(c_e)}{\partial x}\right)\left(\frac{\partial \emptyset_e}{\partial x}\right)dx \tag{30}$$

$$q_c = i^2\frac{R_C}{A} \tag{31}$$

As mentioned, Equation (29) calculates the total heat from reaction (U is the open-circuit potential), Equation (30) calculates the total heat from Joule heating which is caused by the resistance of the solid and electrolyte materials, and Equation (31) calculates the total heat from contact resistance between the current collectors and electrodes [52, 57]. AutoLionST does not explicitly present how entropic heating is modeled, an example of the calculation process for entropic heating is shown below as described by Srinivasan and Wang [54]. The actual entropic heat generation is defined as [42, 54]:

$$q_e = \int_0^L j^{Li} T\frac{\partial U}{\partial T}dx \tag{32}$$

As before, U is the open-circuit potential. The difficulty is modeling the $\partial U/\partial T$ term. Srinivasan and Wang [54] used two empirical equations fit to data; the one for the positive electrode of $LiMn_2O_4$ in their case used data from Thomas et al. [60] and the other expression for the negative carbon electrode used data from Al Hallaj et al. [61]. Srinvasan and Wang expressed these empirical formulas as functions of SOC [54]. In the two equations shown below, *x* denotes the SOC of the given electrode, and the subscripts *a* and *c* denotes anode and cathode, respectively [54]:

$$\frac{\partial U}{\partial T_a} = 344.1347148 \times \frac{\exp(-32.9633287x + 8.316711484)}{1 + 749.0756003\exp(-34.79099646x + 8.887143624)} - 0.8520278805x + 0.362299229x^2 + 0.2698001697 \tag{33}$$

$$\frac{\partial U}{\partial T_c} = 4.31274309\exp(0.571536523x) + 1.281681122\sin(-4.9916739x) \quad (34)$$
$$- 0.090453431\sin(-20.9669665x + 12.5788250)$$
$$- 0.0313472974\sin(31.7663338x - 22.4295664)$$
$$- 4.14532933 + 8.147113434x - 26.064581x^2$$
$$+ 12.7660158x^3 - 0.184274863\exp\left(-\frac{x - 0.5169435168}{0.04628266783}\right)^2$$

Butler-Volmer equation (solved for each electrode) [57]:

$$j^{IC} = a_s {i_o}^{IC}\left\{\exp\left[\frac{\alpha_a F}{RT}\left(\eta - \frac{R_f}{a_s}j^{Li}\right)\right] - \exp\left[-\frac{\alpha_c F}{RT}\left(\eta - \frac{R_f}{a_s}j^{Li}\right)\right]\right\} \quad (35)$$

Finally, the Butler-Volmer equation is applied at each electrode to model the reaction rates of the lithium intercalation reactions [52, 57]. R, T, and F are the universal gas constant, battery temperature and Faraday's number respectively. α_a and α_c are the anodic and cathodic transfer coefficients (both taken to be 0.5 at both electrodes), R_f is the film resistance at the given electrode measured in $\Omega{\cdot}m^2$, and again a_s is the specific interfacial area [52, 57]. ${i_o}^{IC}$ is the exchange current density, and η is the local surface overpotential [52, 57]. ${i_o}^{IC}$ is a function of lithium concentrations and as reported by Fan et al. is calculated by:

$${i_o}^{IC} = k(c_e)^{\alpha_a}\left(c_{s,max} - c_{s,e}\right)^{\alpha_a}\left(c_{s,e}\right)^{\alpha_c} \quad (36)$$

Here, c_e, and $c_{s,e}$, are the lithium concentrations in the electrolyte and at the electrode/electrolyte interface, respectively [52]. $c_{s,max}$ is the maximum lithium concentration in the solid phase [52].

η is defined in Equation (37) below:

$$\eta = \emptyset_s - \emptyset_e - U \quad (37)$$

Experimental curve fits are used to define the open-circuit voltage, U; AutoLionST's method for defined the open-circuit voltage curve is proprietary, however for reference Gu and Wang [53] present an experimental fit which they employ in their model.

Finally, in Equation (35), j^{IC} represents the volumetric electrode current due to intercalation reactions (not taking into account side reactions) [57]. This can be related back to j^{Li} by Equation (38) below [57]:

$$j^{Li} = j^{IC} + i_s a_s \quad (38)$$

i_s, is the side reaction current density, this will be defined when discussing the degradation modeling [57].

With the model presented above, defines the operation of a lithium-ion cell; the next subsection will present the degradation model used by AutoLionST.

3.4 Modeling of Degradation Mechanisms

AutoLionST provides the user the ability to apply degradation mechanisms, as seen in literature, during cycling. The available degradation mechanisms are: SEI film formation at the carbon anode, film formation at the cathode, and active material loss at both electrodes [57]. Based on the suggested degradation parameters suggested by AutoLionST for cells with $LiFePO_4$ or NMC cathodes, the mechanism at the anode are the dominant ones in these simulations [57].

3.4.1 SEI Film Growth

In order to model SEI growth on the carbon anode, AutoLion assumes a reaction occurs at the interface between carbon particles and the current SEI layer [57]. Note that the model includes an initial SEI layer. Before this reaction occurs, ethylene carbonate (EC) must diffuse through the SEI layer to this interface [57]. Equation (39) represents the diffusion equation which describes this movement of EC [57]:

$$\frac{\partial c_{EC}}{\partial t} = D_{EC}^{eff} \frac{\partial^2 c_{EC}}{\partial r^2} \tag{39}$$

Where, D_{EC}^{eff} is an effective diffusivity accounting for the tortuosity of the path through the SEI layer, and is a function of SEI layer porosity [57]. Like other effective parameters, it is calculated using a Bruggeman relation [57].

Once EC has diffused to the particle-SEI layer interface, the following reaction occurs to produce lithium alkyl carbonate ($(CH_2OCO_2Li)_2$) [57]:

$$2(CH_2O)_2CO + 2e^- + 2Li^+ \rightarrow (CH_2OCO_2Li)_2 + C_2H_4 \tag{40}$$

This reaction is described by the kinetic equation shown by Equations (41) and (42) [57]:

$$i_{s,A} = -i_{0s,A} \exp\left[\frac{\alpha_{s,A} F}{RT}\left(\phi_s - \phi_e - R_{SEI} i_{t,A}\right)\right] \tag{41}$$

$$i_{t,A} = \frac{j^{Li}}{a_s} \tag{42}$$

Here, $i_{s,A}$ is the side reaction current density, and $i_{t,A}$ is the total current density of both intercalation and the side reaction which is related to the volumetric electrode current as seen above [57]. R_{SEI} is the SEI film resistance measured in $\Omega \cdot m^2$ [57]. $i_{0s,A}$ is the exchange current density for the side reaction and is related to the concentration of ethylene carbonate (EC) at the reaction surface according to Equation (43) [57]. As well, $k_{s,A}$ is a rate constant specified using an Arrhenius relation with a defined activation energy and reference rate constant [57]:

$$i_{0s,A} = F k_{s,A} c_{EC}^s \tag{43}$$

c_{EC}^s is the concentration of EC at the reaction surface (found from Equation (39)). After solving these equations, the growth of the SEI layer is determined by Equation (44) [57]:

$$\frac{\partial \delta_{SEI}}{\partial t} = \frac{-i_{s,A}}{2F} \frac{M_{SEI}}{\rho_{SEI}} \tag{44}$$

Here δ_{SEI} is the SEI layer thickness, and M_{SEI} and ρ_{SEI} are the molecular weight and density of the SEI layer, respectively [57]. The resistance of the SEI layer can also be calculated at this point [57]:

$$R_{SEI} = \frac{\delta_{SEI}}{\kappa_{SEI}^{eff}} \tag{45}$$

Here, κ_{SEI}^{eff} is the effective conductivity of the electrolyte through the SEI layer, again accounting for the tortuous path using a Bruggeman relation [57].

In this model, the SEI film growth is continuous. As seen in literature such as with Desphande et al. [34], this is attributed to crack propagation as a result of fatigue triggered by volume changes, although this physical damage is not directly modeled.

Using these equations, the growth of the SEI layer is modeled by AutoLionST as the battery is cycled. A similar model is used for film growth at the cathode.

3.4.2 Positive Electrode Film Growth

To describe diffusion of EC through the layer, Equation (36) is used again, with appropriate parameters. The reaction describing production of the film for an NMC cathode is as follows [57]:

$$Li(Ni, Co)O_2 + ROCO_2R' \rightarrow (Ni, Co)O_2R + R'OCO_2Li \tag{46}$$

In Equation (46), R is a radical. The reaction shown in Equation (46) is described by a rate equation shown below [57]:

$$J_{s,c} = k_{s,C} c_{EC}^{s} c_{Lix(Ni,Co)O_2} \tag{47}$$

In Equation (47), $J_{s,C}$ represents the side reaction rate per surface area, c_{EC}^{s} is the EC concentration at the particle surface, and $c_{Lix(Ni, Co) O2}$ is the cathode material concentration [57]. Like the SEI film formation, $k_{s,C}$ is a rate constant specified using an Arrhenius relation with a defined activation energy and reference rate constant. The growth of the film can then be described as follows [57]:

$$\frac{\partial \delta_{film}}{\partial t} = J_{s,C} \frac{MW_{film}}{\rho_{film}} \tag{48}$$

The film resistance R_f can be calculated in the same manner at the SEI layer resistance, using appropriate parameters.

Many of the values used for parameters listed in the above degradation equations can be found in the Appendix A.

3.4.3 Loss of Active Material

Another source of degradation is the loss of active material. In AutoLionST, this is referred to as Active Material Isolation (AMI). This mechanism takes into account particles of active material that over time have detached from the binder, and no longer serve as an active material site [57]. This detachment is attributed to mechanical stresses caused by volume changes during cycling [57]. It should be noted that this mechanism is taken into account by AutoLionST [57].

This mechanism is modeled in AutoLion using a simple relation between the rate of material loss and the electrode current from reaction. This relation is shown below [57]:

$$\frac{\partial \varepsilon_{\mathrm{AM}}}{\partial \mathrm{t}} = -\mathrm{k(T)}\left|\mathrm{j^{Li}}\right| \tag{49}$$

Here ε_{AM} represents the volume fraction of the active material [57]. Similar to before, *k(T)* is the rate constant defined by an Arrhenius relation with a specified activation energy and reference rate constant.

At this point, the entire model used to describe the operation and ageing of a lithium-ion cell has been discussed. The next chapter of this thesis will present the methodology for both the experimental and simulation work.

4 Methodology

This chapter will discuss the methodology used during this study. First, the battery selected for the study will be discussed, and then the experimental methodology and the simulation methodology will be presented.

4.1 Battery Selection

As mentioned in the scope of Chapter 1, this study will use lithium-ion batteries with a graphite anode (by far the most common choice of anode), and an NMC cathode. An NMC-cathode battery has been selected due to reasons listed in the introduction; higher rechargeable capacity compared to $LiMn_2O_4$, higher rechargeable capacity and comparable (or greater) energy density compared to $LiCoO_2$, easier to manufacture and similar properties to $LiNi_{1/2}Mn_{1/2}O_2$, and superior operating voltage and energy density to $LiFePO_4$ [23]. As well, at the suggestion of the industry partner the desired battery capacity is 10Ah.

4.1.1 Experimental Battery Selection

The battery studied is a pouch-cell supplied by *AA Portable Power Corporation* with aluminum packaging of dimensions 11 x 60 x 162 mm, a carbon anode, NMC cathode, and a polymer electrolyte; any further specifications of the battery chemistry are proprietary [62, 63]. The battery rated capacity is 10Ah (± 0.5Ah), with a charge cut-off voltage of 4.2V and a discharge cut-off voltage of 2.75V [63].

Once this battery was decided on and purchased, the battery was replicated in AutoLionST to a best approximation.

4.1.2 Simulation Battery Design

Using AutoLionST's battery design interface a battery was designed to reflect the battery purchased for experimental work. Figure 4-1 shows an example of AutoLionST's battery design interface.

A summary of the important battery parameters will be given here, but for a comprehensive list of all battery parameters used in this study refer to Appendix A. The parameters listed as "database" are non-constant, and use built-in AutoLionST relations, some of which are undisclosed.

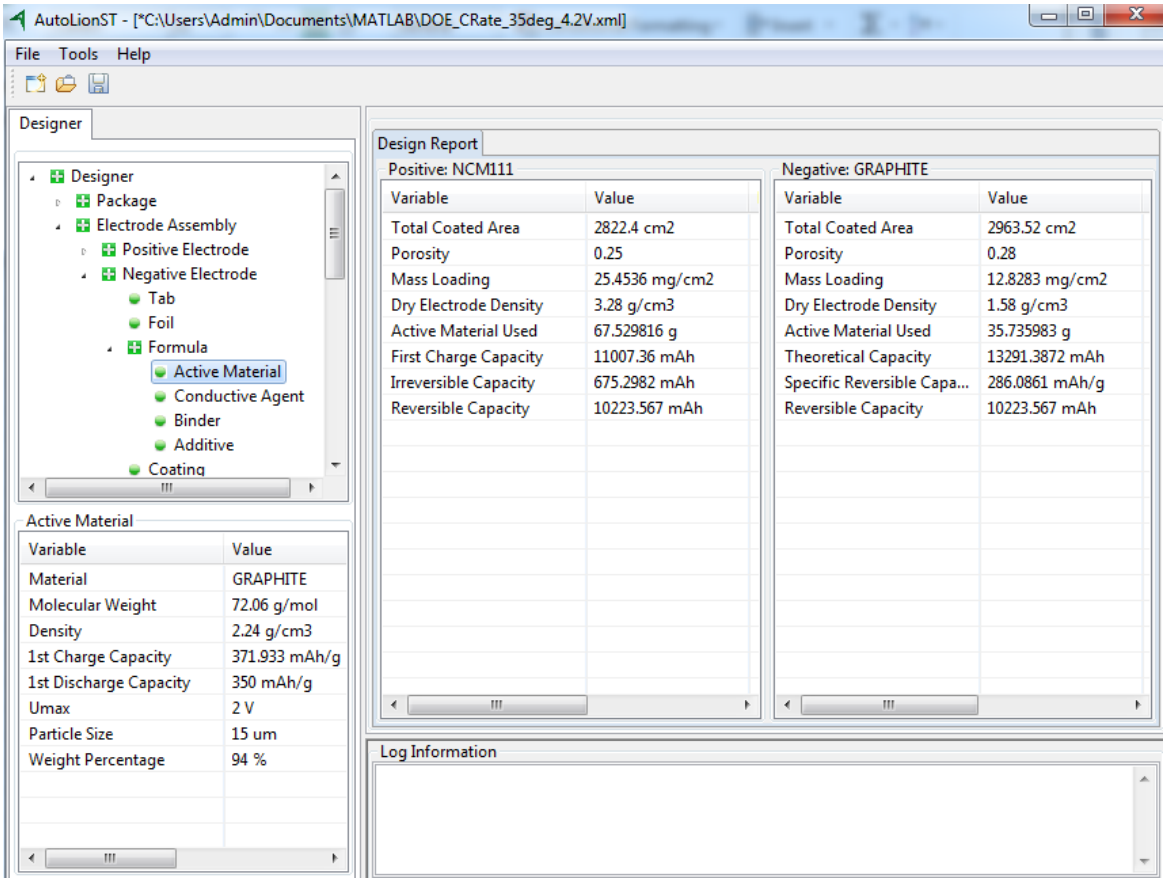

Figure 4-1: Example screenshot of the AutoLionST battery design interface; on the left is the design tree and on the right is a report of important properties [64]

The battery dimensions are listed below in Table 4-1. These dimensions are based on dimensions of batteries purchased for experimental work.

Table 4-1: Physical dimension of the cell used in simulations

Cell Dimension	Value (mm)
Cell width	60
Cell height	162
Cell thickness	11
Inner width	55
Inner height	148
Inner thickness	8

To differentiate between the inner and cell dimensions, the inner dimensions refer to the dimensions of the electrode stack, while the cell dimensions refer to the dimensions of the entire battery [57]. The next table depicts the materials used in the positive and negative electrodes. It should be noted that material properties for the active materials are supplied by AutoLionST.

Table 4-2: Electrode constituents [64]

Electrode Component (Positive)	**Material**	**Weight Percentage (%)**
Active Material	Nickel-manganese-cobalt	94
Conductive Agent	Carbon	3
Binder	PVDF	3
Electrode Component (Negative)	**Material**	**Weight Percentage (%)**
Active Material	Graphite	94
Conductive Agent	Carbon	3
Binder	PVDF	3

The electrode dimensions and loading must also be specified; these are the main parameters which dictate the cell capacity. In order to specify the loading of both electrodes, the positive electrode loading and the N/P loading ratio are specified. All of the parameters listed in Table 4-1, Table 4-2, and Table 4-3 result in a battery of capacity 10.22Ah.

Table 4-3: Electrode dimensions and loading [64]

Electrode Parameter (Positive)	**Value**	**Units**
Thickness	170	µm
Width	49	mm
Height	144	mm
Loading	3.9	mAh/cm^2
Electrode Parameter (Negative)	**Value**	**Units**
Thickness	170	µm
Width	49	mm
Height	144	mm
Loading	4.485	mAh/cm^2

As for the additional physical battery aspects, a 20µm Celgard separator is used, and an electrolyte using $LiPF_6$ salt in a solution of EC (ethylene carbonate)-EMC (ethylene methyl carbonate)-DMC (dimethyl carbonate) with a concentration of 1.2M is considered.

All of the parameters listed above are defined under the "Designer" tab in AutoLionST's design interface; the "Simulator" tab defines the remaining coefficients, constants, and parameters required to solve the equations governing battery operation. Under the "Simulator" tab the lower and upper cut-off voltages are set to 2.75V, and 4.2V, respectively, and the OCV at 100% SOC was also set to 4.2V. The other initial conditions such as cell temperature and SOC varied between simulations. As mentioned earlier, Appendix A has a full list of all the battery parameters used in the present simulations.

To reflect the battery to be used in the experimental work, the lower and upper cut-off voltages were set to 2.75V, and 4.2V, respectively. The OCV at 100% SOC was also set to 4.2V. The other initial conditions such as cell temperature and SOC varied between simulations.

All the parameters and coefficients for the governing equations (excluding the conservation of energy) were either accessed through the AutoLionST database, or utilized the default value suggested by AutoLionST.

The next subsections will describe the methodology used throughout the study.

4.2 Experimental Methodology

4.2.1 Experimental Plan

Experimentation will be used as a base case to validate the simulation model. Two experiments will take place. First, the battery will be held at isothermal conditions and cycled over long periods; this will be used to validate the electrical governing equations, and degradation mechanisms. As well, non-isothermal tests will take place to measure the increase in battery temperature over a typical cycle; this will be used to validate the temperature trends of the thermal model.

4.2.1.1 Isothermal Experiments

Experimental work was performed in order to come up with a base case in order to validate the simulation model. Performing capacity fade experiments is incredibly time consuming (1000 cycles of 1C charge/discharge would take close to three months) so experimentation is not an ideal method to explore the effects on capacity fade. A battery will be tested in a laboratory environment for a relatively short number of cycles (approximately 350 cycles), capacity fade data will be captured, and from this the simulation model can be calibrated.

Since all experimental work is only being used as a base case, a simple loading will be applied. The battery will be fully discharged from 4.2V to 2.75V at a rate of 1C (10A), and charged using a 1C constant-current-constant-voltage (CCCV) load profile. CCCV charging strategy is common strategy used to charge batteries where a constant current, 10A in this case, is applied until the upper-cut-off voltage, 4.2V, is reached, then the battery is charged with at constant voltage of 4.2V and the current is stepped down until it reaches a specified value. This value is often 1% of charge current, which is 0.1A in this case. This charging profile allows the battery to hold charge more effectively once the load is removed. Between each discharge (or charge) and charge (or discharge) the battery is rested for 5 minutes. As the battery is cycled, battery capacity will be recorded.

As well, since battery operation is sensitive to thermal conditions, it is desired that battery temperature is controlled for this base experimental case. It was decided that these experiments would take place at a moderately elevated temperature of 35˚C.

4.2.1.2 Non-Isothermal Experiments

As mentioned previously, these experiments are performed to validate the trends in battery temperature rise over typical operation. In these experiments, a battery is left open to room conditions; one side lies on a slab of insulation, the other faces up, exposed to the environment.

The battery is discharged at 1C (10A) while the battery surface temperature is measured for the surface exposed to the room air, using an array of thermocouples.

4.2.2 Experimental Setup

An experimental apparatus was set up to cycle batteries over long periods, and record capacity data. These experiments were performed using an *Emerald-Advanced Battery Test Station*, manufactured by *Greenlight Innovation* to repeatedly discharge and charge a battery over an extended period of time [73].

The battery test station also records extensive data and monitors the battery during operation. The test station records accumulated charge as the battery is in operation which represents the charge (in Ah) that the battery supplies. Hence, the accumulated charge at the end of discharge is the true capacity that the battery delivers, which is the data of interest.

Battery temperature was controlled through the use of temperature-controlling plates to hold the battery at near-isothermal conditions. Two plates were designed to control temperature on both sides of the battery; both plates featured identical ¼ NPT tapped channels to control temperature by the use of a working fluid. Figure 4-2 shows multiple views of a SolidWorks model with transparent plates to show the manifold design in relation to the size and location of the battery. These were machined out of aluminum to ensure good thermal conductivity. Observe that the projected area of flow channels occupies much of the battery surface area.

Both plates are connected to a *Thermo Scientific A 25B* thermal bath [74] supplying a 50/50 mixture of water and ethylene glycol circulated by a *Thermo Scientific AC200 Immersion Circulator* [75] at a flow rate of 20L/min (10L/min per plate) through tubing of 5/16″ I.D. The specified working fluid and flow rate results in a mass flow rate of approximately 0.4 kg/s. The battery surface temperature was monitored by *Labview* using an array of 15 T-type *Omega* thermocouples, held in place using *Swagelok* brass tube fittings. The standard limits for error for the T-type thermocouples is ±1°C [76]. The two thermal plates are held parallel to each other using four bolts; springs are also set below the bottom thermal plate to ensure good contact between the plates and battery while allowing for any expansion. Figure 4-3 depicts the thermal plates, and the full experimental set up.

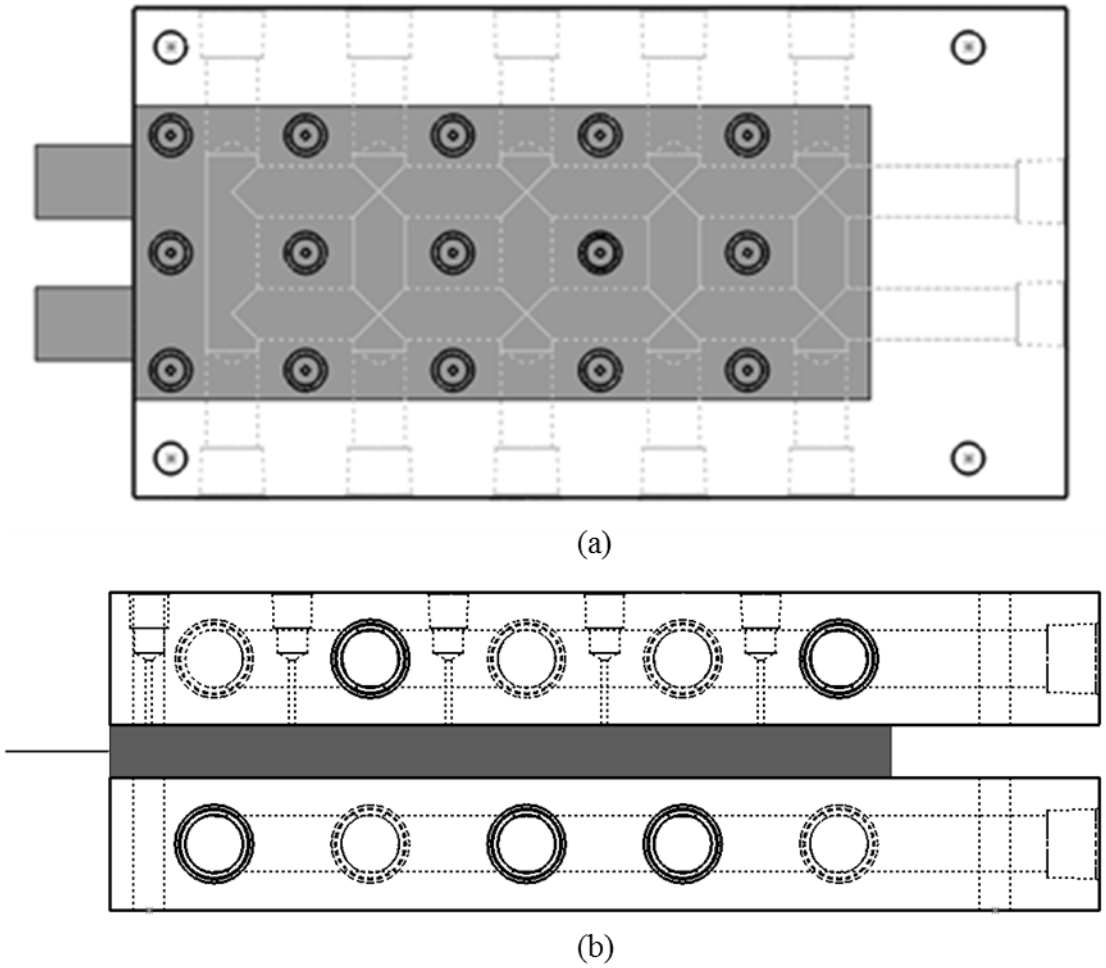

Figure 4-2: Thermal plate model, showing channel and thermocouple locations relative to a battery (a) top view; (b) side view

The thermocouples are in contact with the battery surface by firmly pressing them against the battery surface with the use of the pressure fittings. For the isothermal conditions, the entire weight of the top thermal plate rests on the battery with the thermocouples pressure fit to the thermal plate; as such, it is assumed that there is good thermal contact between the battery and thermocouples. For the non-isothermal conditions, a thermal plate is not used and as a result poor thermal contact between the thermocouples and battery surface is expected. To remedy this, *Silver Ice 710NS* thermal grease was applied to the battery surface at thermocouple locations, resulting in much improved thermal contact [72]. The thermal conductivity and thermal resistance of this grease are rated at 7.0 W/m·K and $3.23*10^{-6}$ K·m^2/W [72].

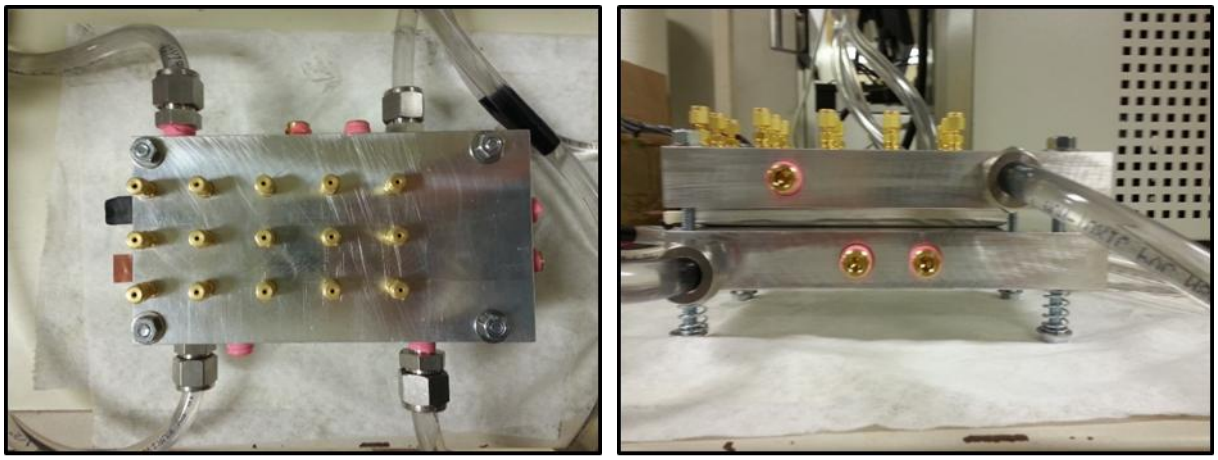

(a) (b)

(c)

Figure 4-3: Experimental setup; (a) top view, thermally-regulated inlets/outlets and thermocouple fittings are seen; (b) side view, battery can be seen between plates; (c) full setup including thermocouples

4.3 Simulation Methodology

This subsection will present the setup for key simulations. The main types of simulations performed were: isothermal 1C charge/discharge simulations, constant C-rate simulations, and simulations applying drive cycles.

4.3.1 AutoLionST Simulation Interface

After designing the battery in the design interface, the second part of AutoLionST is the Simulink interface and solver. In the Simulink environment, a load profile is applied. The load

profile can be applied using a programmable function block, or a simpler predefined block provided by AutoLionST (UDLP block). While the UDLP block is much simpler, it is sufficient for applying drive cycles. Both were used at different points in this study. The figure below depicts part of an example Simulink file.

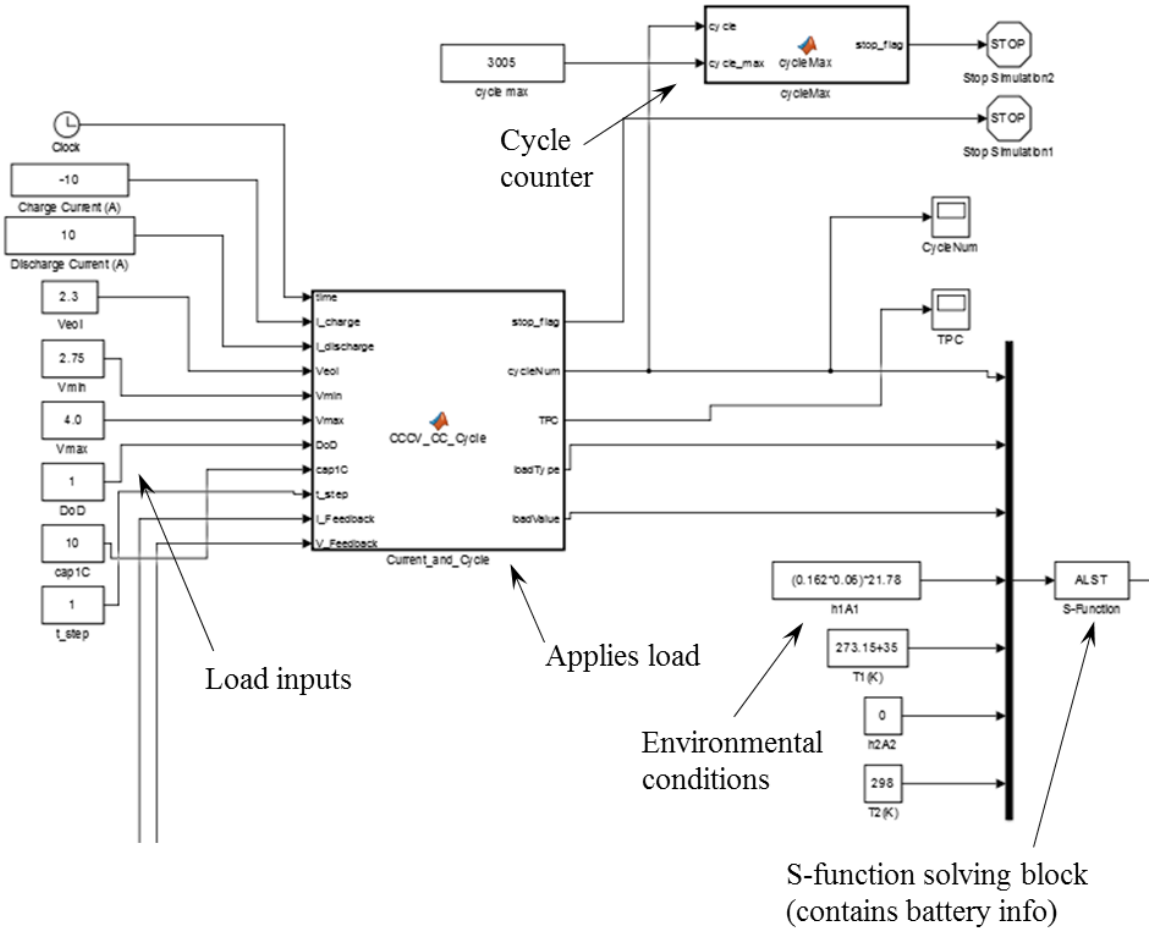

Figure 4-4: Image depicting an example of inputs and S-function blocks of the Simulink solver; here a programmable function block is used

The block titled “CCCV_CC_Cycle” on the left dictates the load profile. In this case, the load profile used was a constant C-rate loading. The inputs to this block are the constant current for charging, the discharge current, the end of life voltage, the minimum voltage, the maximum voltage (4.0V in this case), the DOD (depth of discharge), battery capacity, and time step.

Also seen in Figure 4-4 is a block labelled “ALST”. This block is where the previously designed battery is loaded and solved. The inputs to the ALST block are the parameters defined from the load profile, as well as environmental conditions. These environmental conditions are defined by two pairs of heat transfer coefficients multiplied by a surface area (h1A1 and h2A2), and the temperature with which heat transfer is occurring (T1 and T2). These conditions are applied to battery using Newton’s law of cooling as shown in the equation below:

$$q_1 = h1A1 * (T_{cell} - T1) \quad (50)$$

Also depicted in Figure 4-4 is the block labelled "cycleMax", which acts as a cycle counter. When the cycle limit is reached, the simulated is terminated.

There are numerous outputs created by the solver, however, some of the important ones are current, voltage, power, temperature, and heat generation. A full list of all dynamic outputs can be found in Appendix B.

In order quantify degradation, the simulation is paused at user-defined cycles and is discharged at a user-defined current. All degradation mechanisms are turned off during this period so no further battery ageing occurs during capacity characterization. This quantification was always performed using a 10A discharge current (1C). This process outputs the updated capacity of the cell.

4.3.2 Isothermal 1C Charge/Discharge Simulation Setup

The first simulations performed were to characterize the capacity fade for the selected battery under the isothermal conditions, subject to 1C full discharge (4.2V to 2.75V) and CCCV (constant-current-constant-voltage) charging. These profiles match that which is used for experimental work; 10A discharge, CCCV charging at 10A then 4.2V until the current drawn is 0.1A, with rest period of 3minutes in between. As well, multiple battery temperatures will be used.

The figures below show what the profiles for both current and voltage would look like during one of these cycles. This cycle will be applied until the failure criteria is reached; at the suggestion of the industry partner, the failure criteria is once the battery reaches 75% of its original capacity.

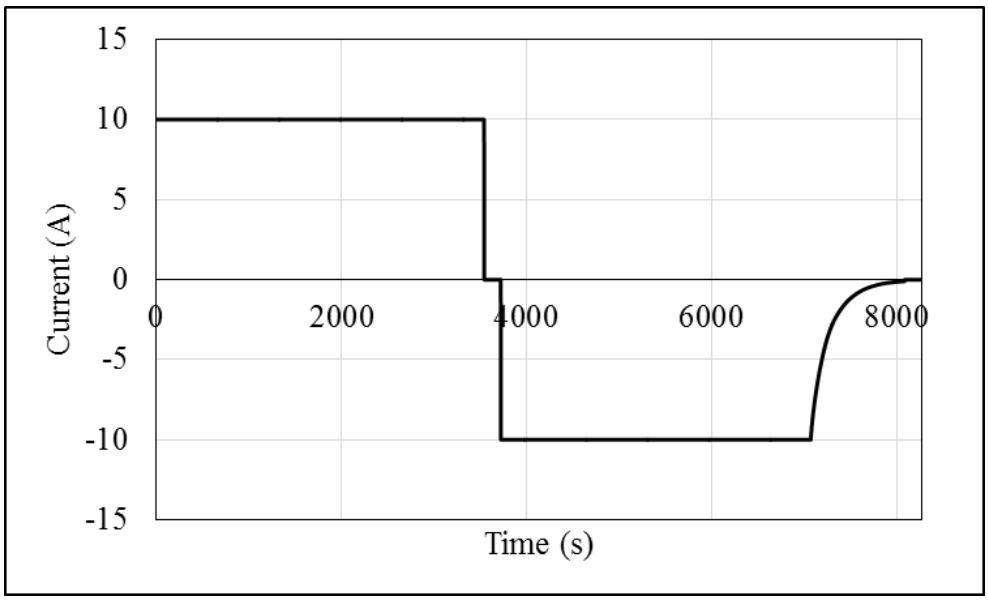

Figure 4-5: Battery current during a single cycle of 1C discharge and CCCV charging with a rest period

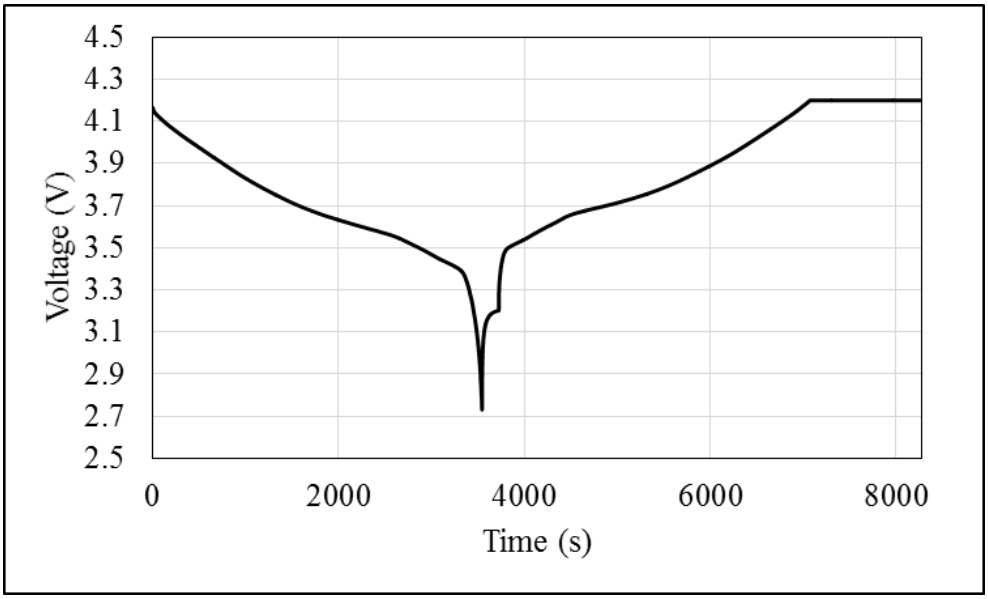

Figure 4-6: Battery voltage during a single cycle of 1C discharge and CCCV charging with a rest period

These simulations will be used to calibrate the model against the experimental work.

4.3.3 Constant C-Rate Simulations

These simulations will begin to explore the effects of operating parameters on capacity fade. Again, batteries will be cycled with a constant discharge current from 4.2 to 2.75V, and then charged with a CCCV profile. However, these simulations will vary the C-rate used for discharge, using rates of 1C, 2C, and 4C, while the charge current will remain at 10A. As well, these simulations will no longer be isothermal; three different thermal management strategies will be considered in the study. At the request of the industry partner, the three thermal management strategies used are natural convection, ICE plate (thermal management plate for electric vehicles) using air as the working fluid, and an ICE plate using a coolant as the working fluid. For reference, Figure 4-7 shows an image of an ICE plate that might be used in an electric vehicle to cool a battery.

The ICE plate shown in Figure 4-7 would be installed between two batteries. The heat transfer coefficients as supplied by the industry partner are for the three methods of thermal management are 6.3, 21.78, and 340 W/m^{2}K. However, these coefficients represent the total cooling for both batteries; the cooling for a single battery is expressed as:

$$q_1 = \left(\frac{h1}{2}\right)(2 * A1) * (T_{cell} - T1) = h1A1 * (T_{cell} - T1) \tag{51}$$

Figure 4-7: Example of an ICE plate that is used in electric/hybrid vehicles to provide battery thermal management [69]

In Equation (51), h1 represents the total heat transfer coefficient (i.e. 6.3, 21.78, or 340 W/m^2K) and A1 is the surface area of only one face of the battery. Convective heat transfer off the edges of the battery is neglected.

On top of the C-rate and thermal management strategy, the battery temperature will also be varied. Since these simulations are not isothermal, the "base" temperature of the battery will be varied. In each case the initial battery temperature, T_0, and the temperature with which heat transfer occurs, T1 (or T_{amb}), will be set to the same value. The values used will be 20, 35, and 50°C. Table 4-4 shows a summary of the operating parameters used in this study.

Table 4-4: Values for operating parameters used in constant c-rate simulations, *heat transfer coefficients supplied by industry partner*

	T_0, T_{amb} (°C)	**C-Rate**	**Heat Transfer Coeff. (W/m^2K)**
Low Value	20	1	6.3
Med. Value	35	2	21.76
High Value	50	4	340

All combinations of operating parameters are simulated resulting in 27 simulations. Again, a failure criterion of 75% of initial capacity is used.

4.3.4 Drive Cycle Simulations

A series of simulations employing drive cycles were performed while varying three chosen variables. The variables of interest were charge voltage (the high voltage which the cell is charged to), battery temperature, and heat transfer coefficient. Again, three values are chosen for each variable, leading to 27 unique simulations. The same drive cycle load profile is used for all simulations; it will soon be discussed in more detail. Table 4-5 shows the values used for the drive cycle simulations.

Table 4-5: Values for operating parameters used in drive cycle simulations, *heat transfer coefficients supplied by industry partner*

	T_0, T_{amb} (°C)	Charge Voltage (V)	Heat Transfer Coeff. (W/m^2K)
Low Value	20	4.0	6.3
Med. Value	35	4.1	21.76
High Value	50	4.2	340

For all simulations, 3.0V was set as the minimum cell voltage. In these simulations the failure criteria are defined as if the battery reaches 75% of its original capacity or, the battery reaches its minimum voltage level of 3.0V. This change is due to the fact that using a drive cycle, there is a fixed energy requirement and the battery is used for a fixed amount of time. Hence, failure is considered once the battery can no longer provide the required energy within the specified voltage range. This is opposed to constant C-rate simulations where the battery was fully drained, but the energy delivered is directly related to the capacity, and so decreased over cycling.

The vehicle parameters used were chosen to reflect a Chevrolet Volt, Table 4-6 shows these values.

Table 4-6: Vehicle parameters used for the simulations under the FTP drive cycle

Parameter	Value	Units
Coefficient of drag (C_D) [67]	0.28	-
Rolling resistance coefficient (C_{rr}) [68]	0.011	-
Frontal area (A_f) [67]	23.7	ft^2
Curb weight (W_c)	1721	kg
Payload (W_p)	100	kg
Total Weight (W_t)	1821	kg
Air density (ρ_a)	1.2	kg/m^3

The drive cycle used in these simulations is the FTP (Federal Test Procedure) drive cycle, which is also known as FTP-75 or EPA 75 [66]. The FTP drive cycle lasts for 1875 seconds,

covering a distance of 11.04 mi (17.77 km), with an average speed of 21.2 mi/hr (34.12 km/hr), and reaches a top speed of 56.7 mi/hr (91.25 km/hr). The data available for a given drive cycle is just the vehicle velocities over the drive cycle duration. A method found on an online drive cycle calculator titled, *Wheels: Vehicle Road Load and Fuel Economy Online Calculator*, was used to translate these velocities to power consumption [65].

In order to translate vehicle velocity to power consumption simple Newton mechanics are used. Three forces are taken into account; rolling resistance (F_{RR}), aerodynamic drag (F_{AD}), and inertial forces (F_I). The discretized equations used to calculate them at a given time are as follows [65]:

$$F_{RR} = mgC_{rr} \tag{52}$$

$$F_{AD} = \frac{1}{2}\rho_a C_D A_f \left(\frac{V_i + V_{i-1}}{2}\right)^2 \tag{53}$$

$$F_I = m(V_i - V_{i-1}) \tag{54}$$

In Equation (53), $(V_i+V_{i-1})/2$ represents an instantaneous velocity, averaged between two consecutive times. In Equation (54) (V_i-V_{i-1}) represents an instantaneous acceleration, since the time step is one second. The total force is merely the sum of these three forces. The tractive power can then be calculated as [65]:

$$P_{tractive} = F_{Total}\frac{(V_i + V_{i-1})}{2} \tag{55}$$

An efficiency of 75% was also included. In addition, only one cell is simulated so this tractive power must be divided by the number of cells in the vehicle; a value of 288 cells (same as the Chevrolet Volt) was used. Therefore, the true power consumed by a single cell is expressed as [65]:

$$P_{true,per\ cell} = \frac{1}{0.75} * \frac{P_{tractive}}{288} \tag{56}$$

Figure 4-8 depicts the calculated power profile during an FTP drive cycle for a single cell. The negative power indicates braking power which has been captured via regenerative braking.

In the first part of the analysis, regenerative braking will be neglected, and power will only be drawn. Later in the analysis, regenerative braking will be considered using the calculated braking power. It is assumed that the regenerative braking is 50% efficient (on top of the system efficiency of 75%). The power associated with regenerative braking is expressed in Equation (57). Note that $P_{tractive}$ will be a negative value:

$$P_{Regen,per\ cell} = 0.5 * 0.75 * \frac{P_{tractive}}{288} \tag{57}$$

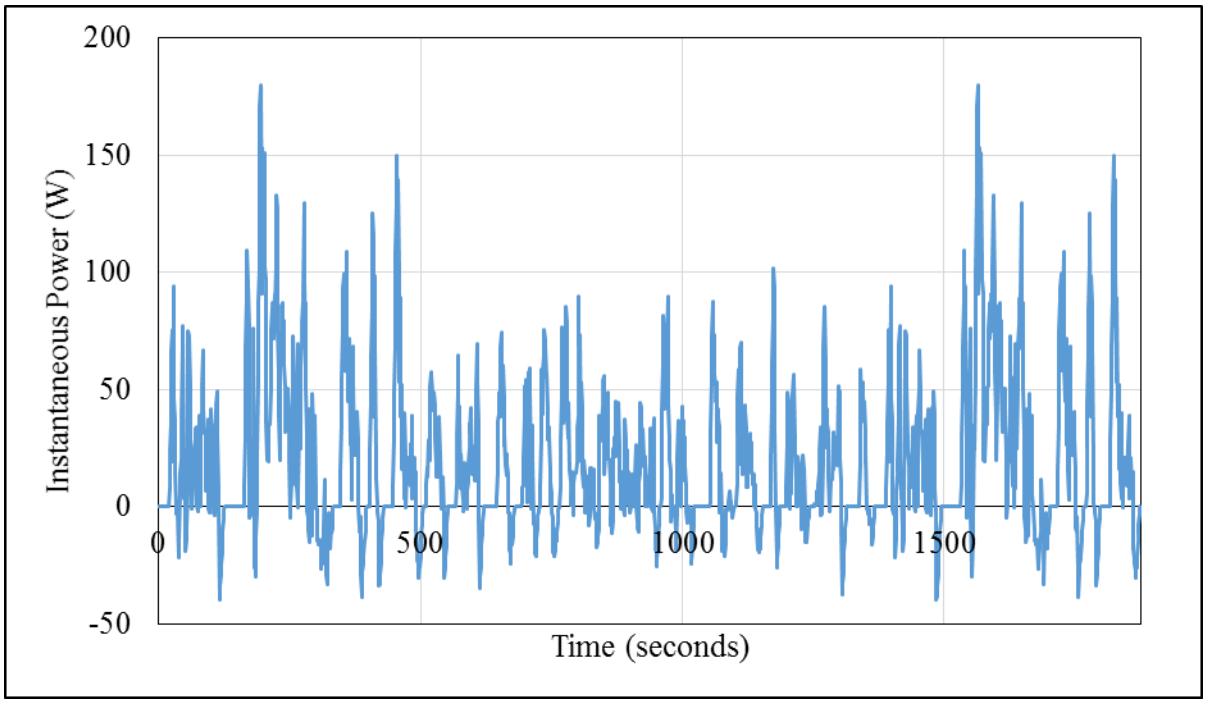

Figure 4-8: Instantaneous power consumption for a single cell during an FTP drive cycle

The overall drive cycle applied is meant to represent a single day use of the vehicle. A single cycle is composed of the following:

- Eight hour rest period (overnight)
- FTP drive cycle (drive to work)
- Eight hour rest period (at work)
- FTP drive cycle (drive home)
- Three minute rest period (rest period before charging)
- 1C-CCCV charge period

This cycle allows the battery voltage and more importantly temperature to come to a steady value before a new driving period.

5 Experimental Results

5.1 Isothermal Experiments

This section presents the experimental results. Experimental results are quite brief since simulations made up the majority of this study; recall that these results are used for calibration purposes.

Figure 5-1, on the following page, displays the discharge and charge profiles of for both current and voltage for one cycle of results. In the next chapter these will be compared to discharge and charge curves performed in simulations. These results are for Battery 1, cycled at 35°C.

As mentioned in the methodology, battery capacity is recorded at the end of each discharge/charge phase by the battery test station. As mentioned in Chapter 4, these batteries were held at 35°C. Figure 5-2 shows the temperature measurements over 10 cycles (cycles 11-20) for arrays of 15 thermocouples for two separate batteries, each with the thermal bath temperature set to 35˚C.

As seen in Figure 5-2 temperatures remain very consistent, at just below 35˚C for both batteries over cycling. As an example, over the first 10 cycles, the average battery surface temperature is 34.6°C with a standard deviation of 0.03°C. The maximum spatial surface temperature difference within a single time step is 0.42°C, with an average spatial temperature difference of 0.32°C throughout all time steps.

Figure 5-3 depicts the capacity fade data for two separate batteries each subject to the same loading, both held at approximately 35˚C (as seen in Figure 5-2).

Since the same testing was applied to both batteries, using the exact same apparatus, it is assumed that differences in manufacturing resulted in one battery degrading more rapidly than the other. It should also be noted that Figure 5-3 contains all the data collected – the capacity at every cycle, including outliers. Multiple outliers can be seen below the curves for both Battery 1 and 2; these outliers were neglected when this data was used for model validation and refinement. Due to time constraints, further experimental testing has not been performed; Battery 1 will be used to validate and refine the simulation model used for the remainder of the study. This calibrated model will be used to explore the trends of capacity fade; specifically, the effect which thermal management system has on ageing. Prospective future work could include acquiring more detailed capacity fade results for this temperature, and for a range of other temperatures.

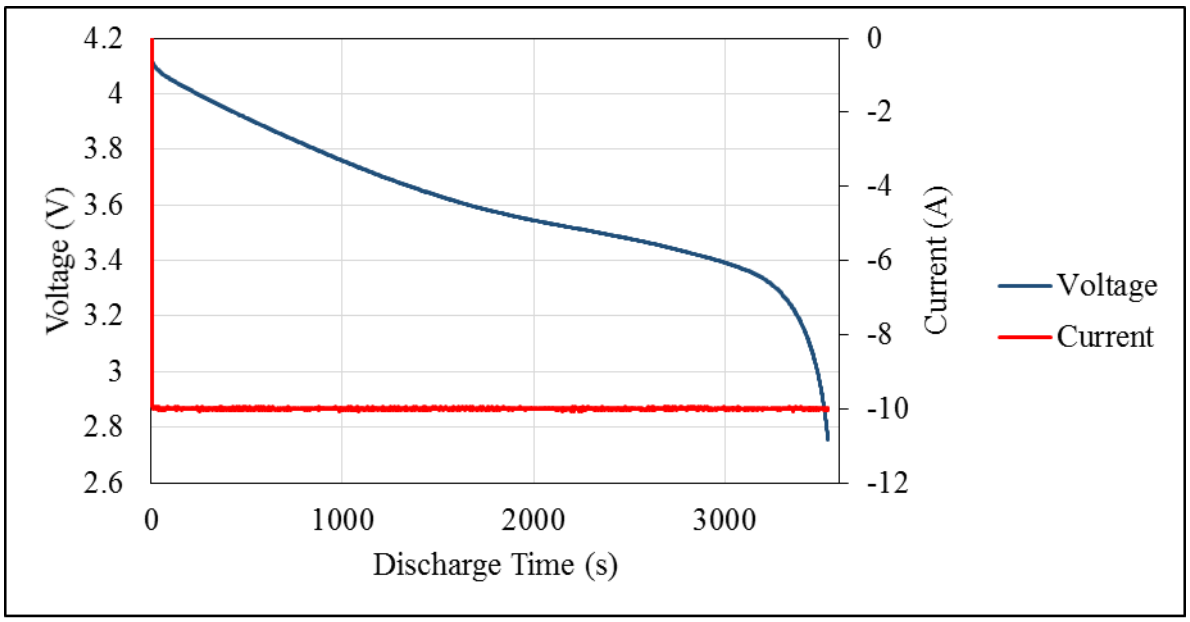

(a)

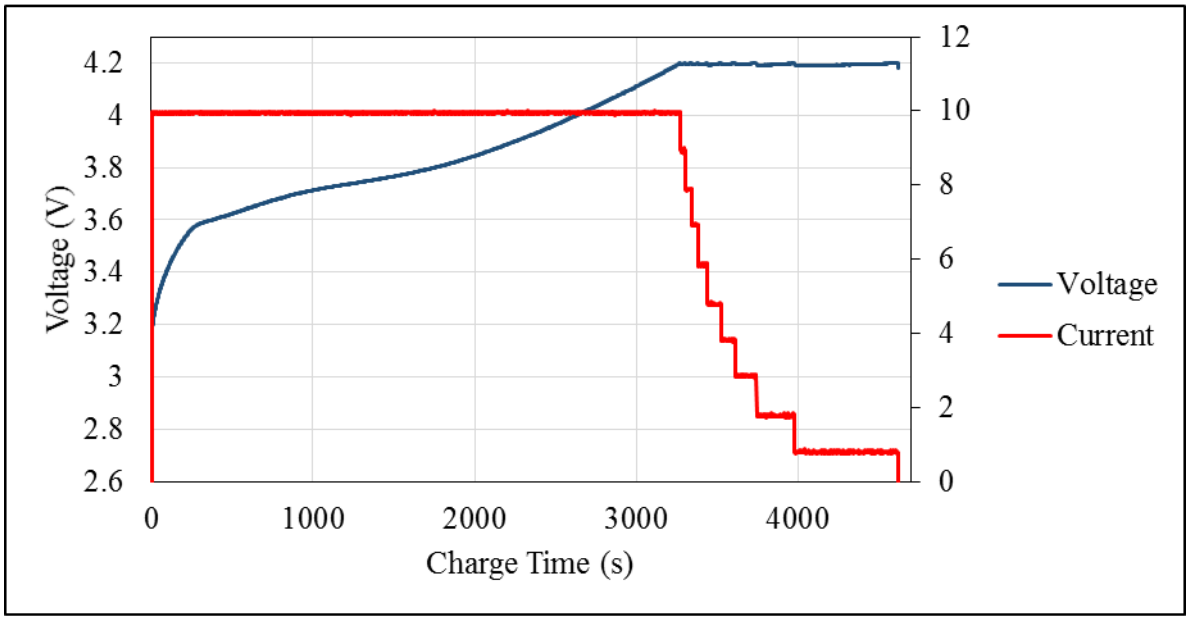

(b)

Figure 5-1: Voltage and current profiles for Battery 1 at 35˚C during (a) discharge period; (b) charge period

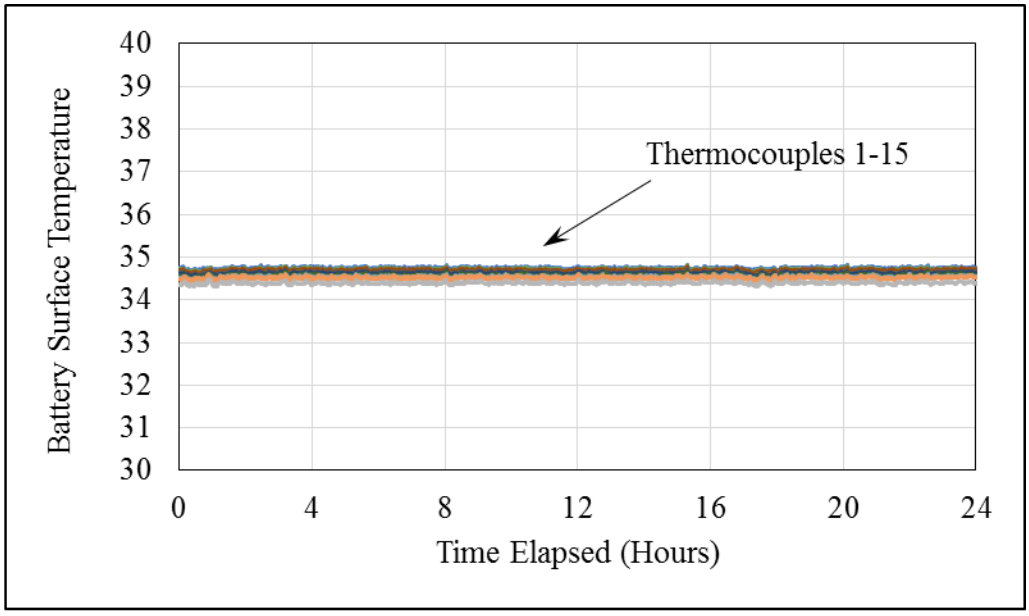

(a)

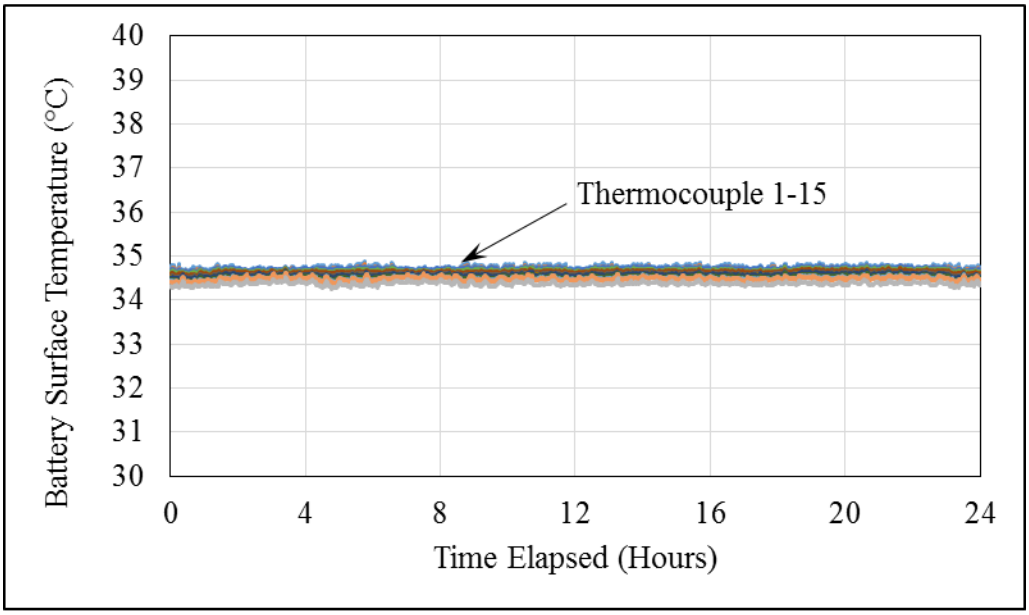

(b)

Figure 5-2: Battery surface temperature as measured with an array of 15 thermocouples over cycles 11-20 for (a) Battery 1; (b) Battery 2

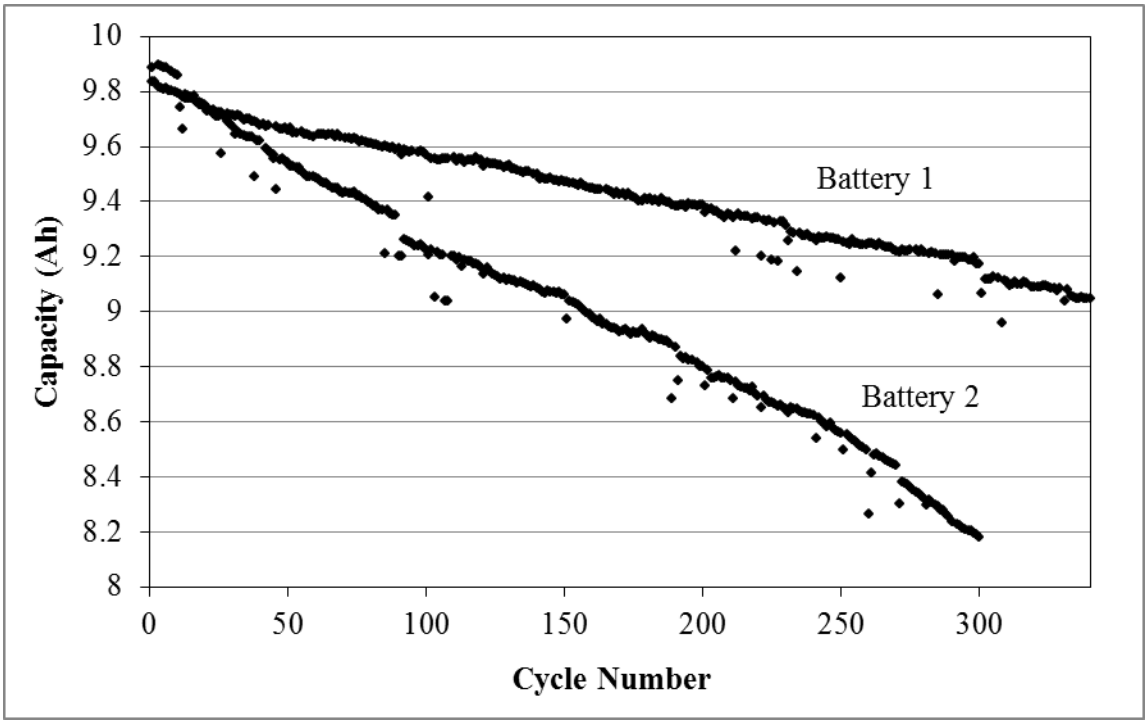

Figure 5-3: Battery capacity following 1C charge/discharge cycling at 35°C

5.2 Non-Isothermal Experiments

A non-isothermal test was performed to observe the trends in temperature increase of a battery. As a reminder, in this experiment, a battery was discharged at 1C (10A) from fully charged state to fully discharged. The battery laid on a piece of insulation, with the top face open to room conditions, while an array of thermocouples measured the battery surface temperature. Thermal grease was used to enhance thermal contact between the battery surface and thermocouples. These results are shown in the validation section.

6 Model Validation and Refinement

This section describes the preliminary results that were obtained and the adjustment of degradation parameters that followed, based on the experimental capacity fade data and data collected by an external source for batteries cycled at lower temperatures.

6.1 Model Validation

This subsection compares the experimental results to results from simulations. Results shown here include discharge and charge profiles, capacity fade data, and well as temperature increase curves.

Figure 6-2 compares the discharge and charge profiles for voltage and current from the experimental work and simulations. In these figures, it is most useful to compare the voltage curves since current is mostly the specified load parameter (apart from the second leg of CCCV charging). As seen in Figure 6-2 and Figure 6-2 there is good agreement between the experimentation and simulations for the battery loads. This validates the electrical governing equations.

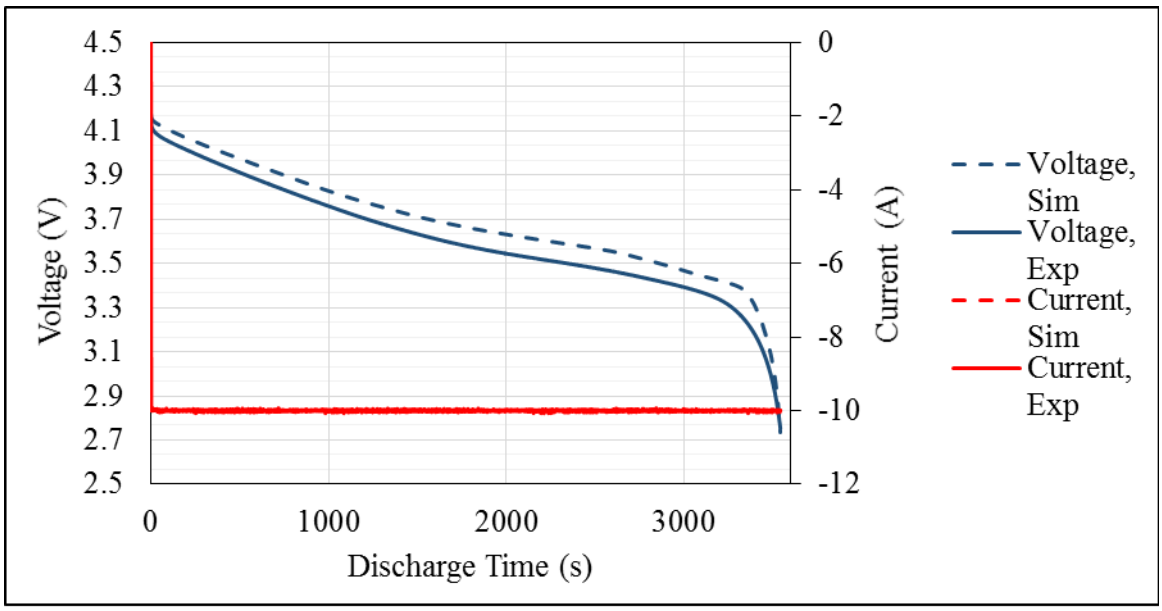

Figure 6-1: Comparison and simulated and experimental voltage and current profiles during a discharge period

As well, the experimental results of the isothermal test can be seen in Figure 6-3. For comparison, Figure 6-4 shows the temperature increases of three cells all discharged at 1C with a specified temperature of 35°C, each cooled with a different heat transfer coefficient. Note that the experimental and simulation trends match very well, with very similar temperature increase for the case of 6.3W/m^2·K (which represents natural convection). As well it should be noted that since only the battery surface temperature was measured, and the other side of the battery was considered insulated, the temperature overall battery temperature would be slightly

higher than what was measured. This information still agrees with the trends since slightly more heat generation is expected for a battery at room temperature than a battery at 35°C.

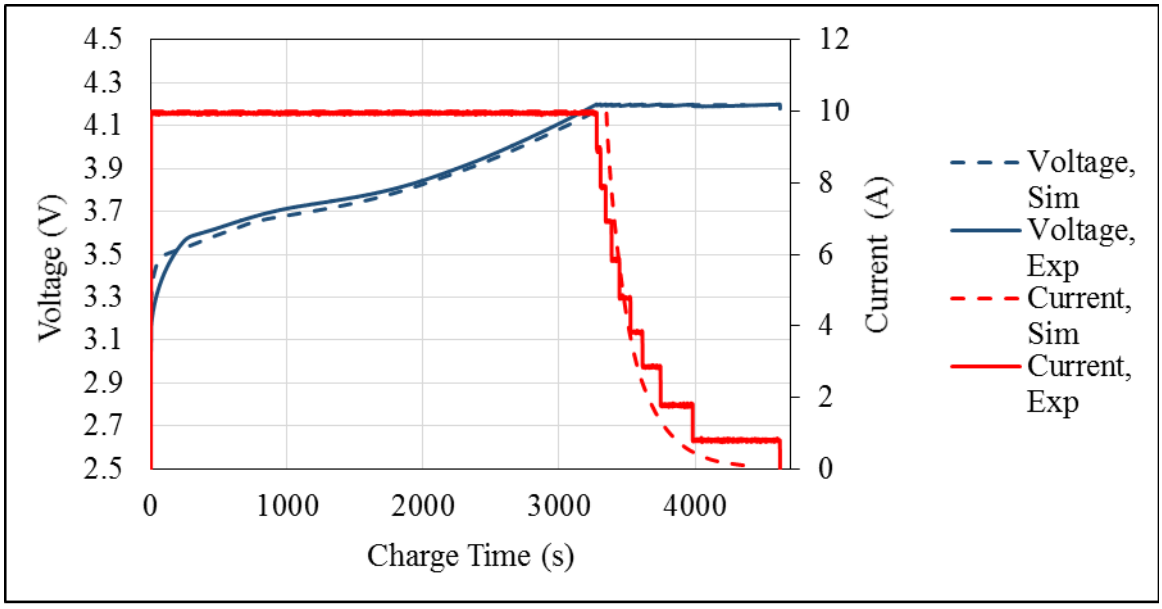

Figure 6-2: Comparison and simulated and experimental voltage and current profiles during a charge period

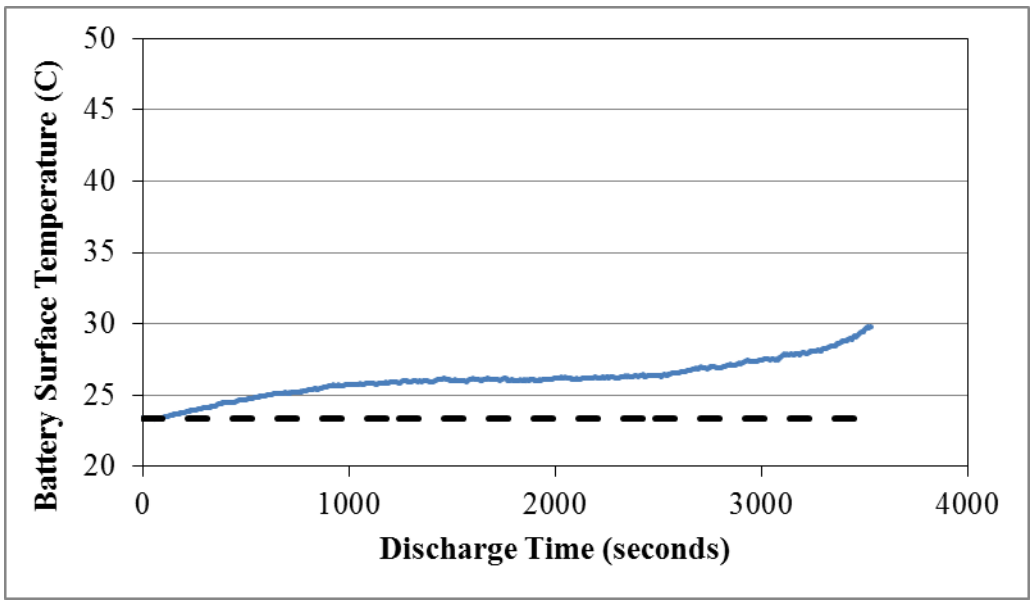

Figure 6-3: Experimental results of battery surface temperature over a single 1C discharge, open to room conditions, $T_{amb} \approx 22°C$, $h \approx 5$ W/m^2·K

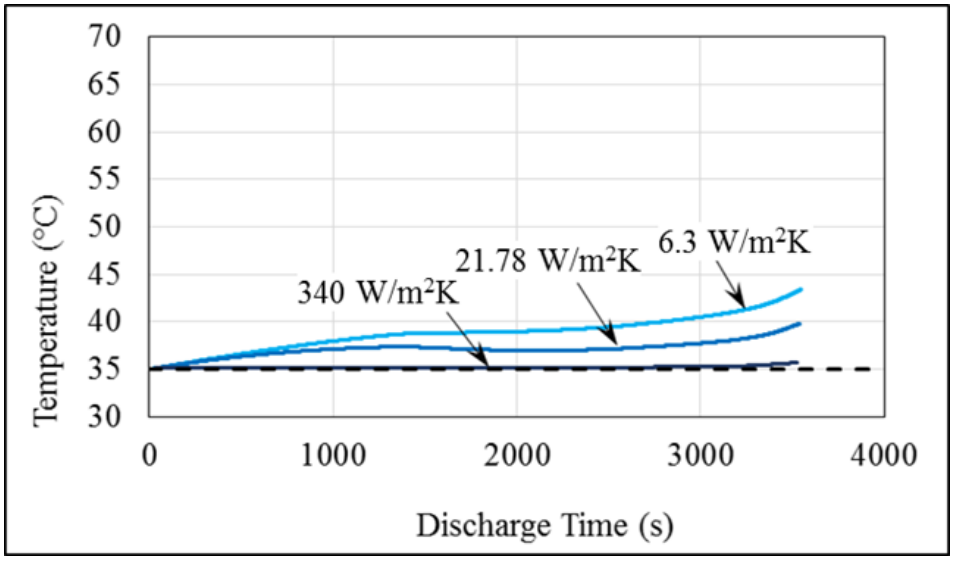

Figure 6-4: Temperature rise during discharge; 1C discharge, specified temperature of 35°C

Figure 6-5 shows the experimental results for the first battery tested compared to AutoLionST preliminary results for an isothermal battery tested at 35°C, under 1C charge/discharge, using original degradation parameters suggested by AutoLionST.

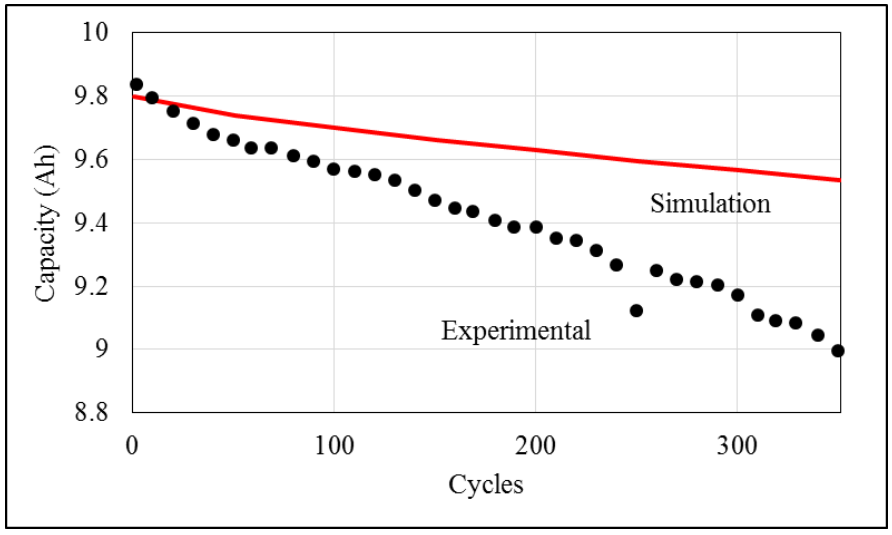

Figure 6-5: Comparison of experimental vs. simulation battery capacity following 1C charge/discharge at 35°C using suggested degradation parameters

Figure 6-5 does not indicate good agreement between the two using default degradation parameters; as a result model refinement was required. In order to perform this refinement, a degradation mechanism parameter study was performed.

6.2 Low Temperature Results and Parameter Investigation

6.2.1 Preliminary Isothermal Results

Figure 6-6 below depicts the preliminary isothermal results for capacity fade over a range of temperatures plotted against the cycle number, for batteries subject to 1C charge/discharge cycles. This study used degradation parameters suggested by AutoLionST for simulation of an NMC/graphite battery.

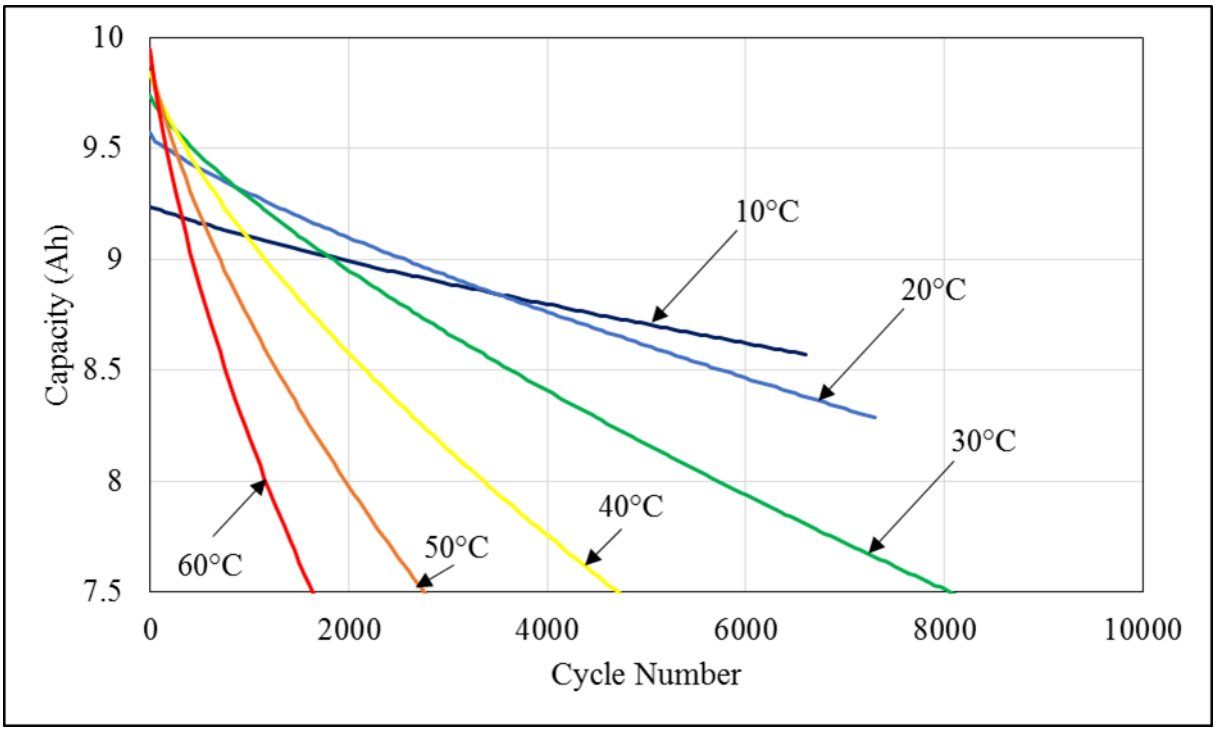

Figure 6-6: Preliminary isothermal capacity fade results for a range of temperatures, using 1C charge/discharge, with AutoLionST suggested parameters

Due to the difference in the initial capacity, it is important to normalize the results (this also makes it easy to observe the failure criteria of 75% of initial capacity). Figure 6-7 below shows the results from Figure 6-6 plotted as normalized capacity; this is merely the battery capacity divided by that battery's initial capacity.

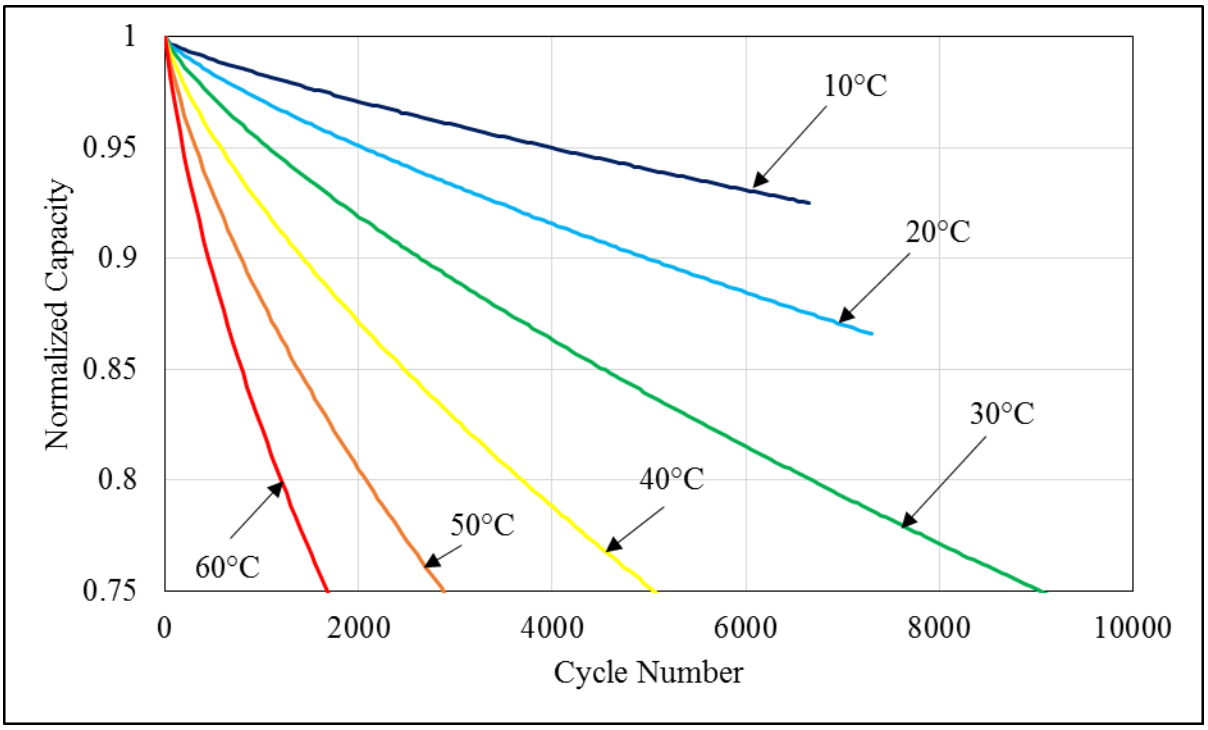

Figure 6-7: Normalized preliminary capacity fade results

An important observation of these figures is the degradation of the low temperature curves (10°C and 20°C). If these were to be extrapolated, it would be well longer than 10,000 cycles (closer to 20,000) before the battery approaches 75% of its initial capacity. Knowing that lithium plating can occur at lower temperatures, the degradation of these batteries seems somewhat high. These trends can be compared to some found in literature. In Figure 2-1, Ramadass et al. showed that batteries cycled from room temperature up to 45˚C exhibit similar capacity fade behaviour after cycling, and that significant accelerated ageing does not occur until 50˚C [30]. This would suggest that for batteries at lower temperatures in Figure 6-7, the model might be overestimating the capacity of the batteries through life. Results from Deshpande et al. much better reflected the capacity fade trends seen by simulations performed with AutoLionST (with results being concave up, oppose to the results from Ramadass et al. [30] which are mostly concave down) [34]. However, the curves are spaced much more evenly between different temperatures compared to the work by Ramadass et al. [30, 34].

After observing these trends in literature, the industry partner requested that a different set of parameters were fit for batteries simulated at 20˚C. The industry partner supplied experimental data of battery degradation for NMC/graphite cells with trends similar to those shown by Deshpande et al. [34]. For these cells, they showed that ideal operating temperature for battery life is at around room temperature (20-25˚C), however there is not a significant improvement in battery life compared to slightly elevated temperatures (~30˚C). Unfortunately, due to confidentiality this data cannot be shared in this thesis.

It was decided not to simulate batteries at any temperature lower than 10˚C to avoid simulations where, in reality, significant lithium-plating would occur. The next section shows

some results of simulations performed at very low temperatures, and will discuss the effect of degradation parameters on the capacity fade of simulated batteries.

6.2.2 Low Temperature Results

More simulations were run at very low temperatures to observe the resultant trends. Figure 6-8 and Figure 6-9 show capacity fade results for these low temperatures both normalized and non-normalized.

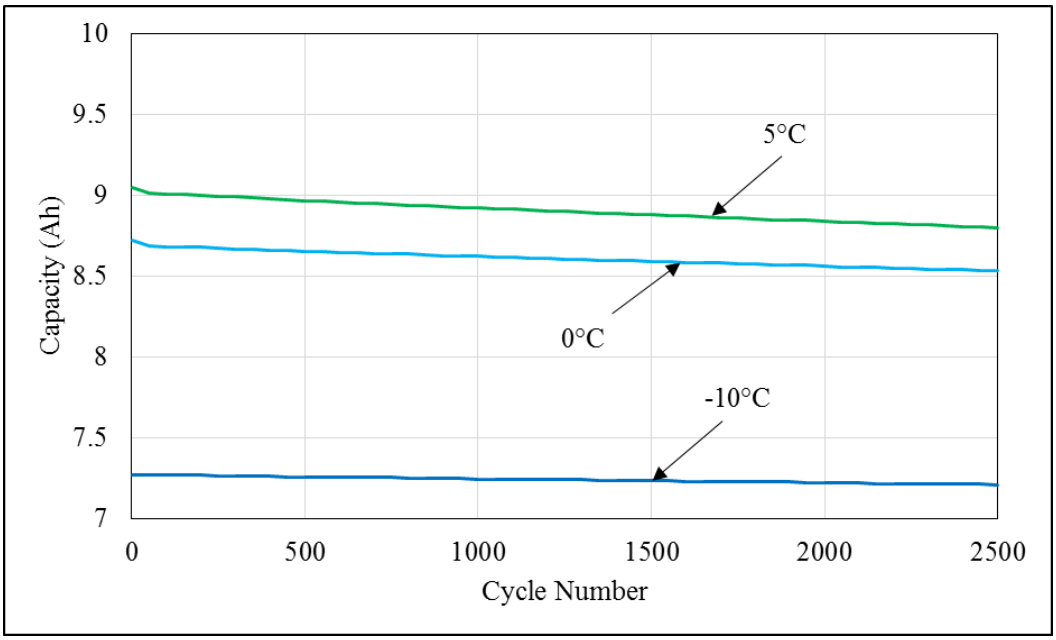

Figure 6-8: Capacity fade of cells at very low temperatures, 1C charge/discharge

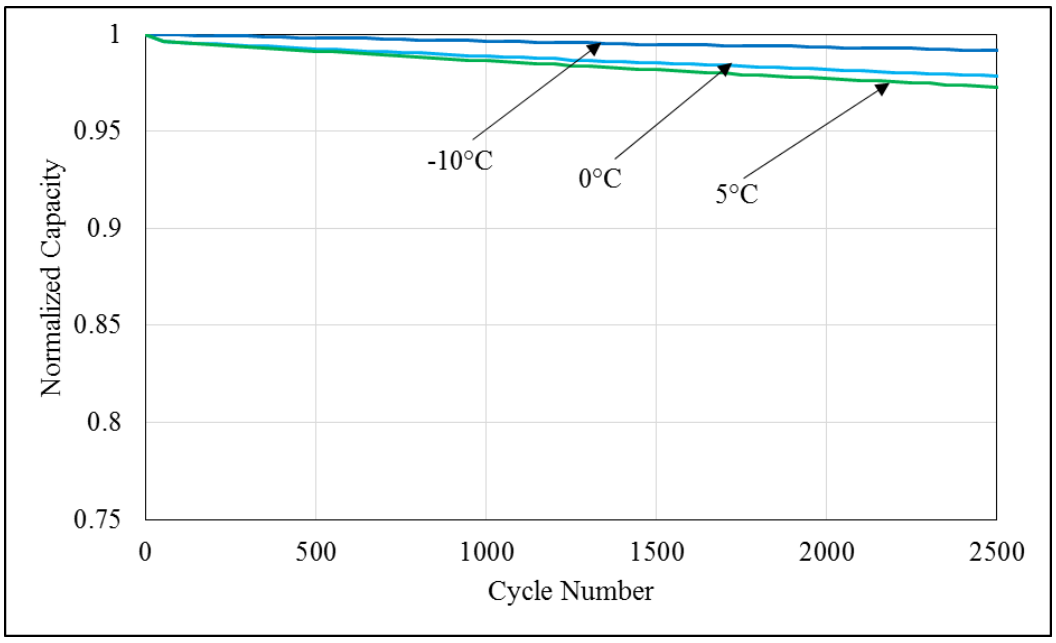

Figure 6-9: Normalized capacity fade of cells at very low temperatures, 1C charge/discharge

By observing these plots, it can be seen that the same trends noted previously continue at very low temperatures, namely a significant drop in initial capacity and nearly negligible capacity fade.

This can be attributed to the fact that the only two ageing mechanisms are accounted for; film growth and active material loss, and as seen in their model they are both accelerated at high temperature (due to the Arrhenius relation which governs the degradation rate constant). As a reminder, the only reported lithium-ion battery degradation mechanism that is amplified at low temperature is lithium plating [39].

6.2.3 Degradation Parameter Investigation

As mentioned, at the behest of the industry partner, a separate set of degradation parameters is required for simulations with lower temperature cells (~20˚C). A degradation parameter study was performed. The goal of this study was to better understand the sensitivity and effect of the degradation parameters, and then find a set of degradation parameters for the existing ageing mechanisms that are capable of predicting degradation at 20°C to more accurately reflect the expected trends.

The first step of this parameter study was to determine which of the four degradation mechanism has the greatest impact on capacity fade. To do this, a short simulation was run each with only one active degradation mechanism (the others were turned off). This was done at an arbitrary temperature of 40°C. The results are shown in Figure 6-10.

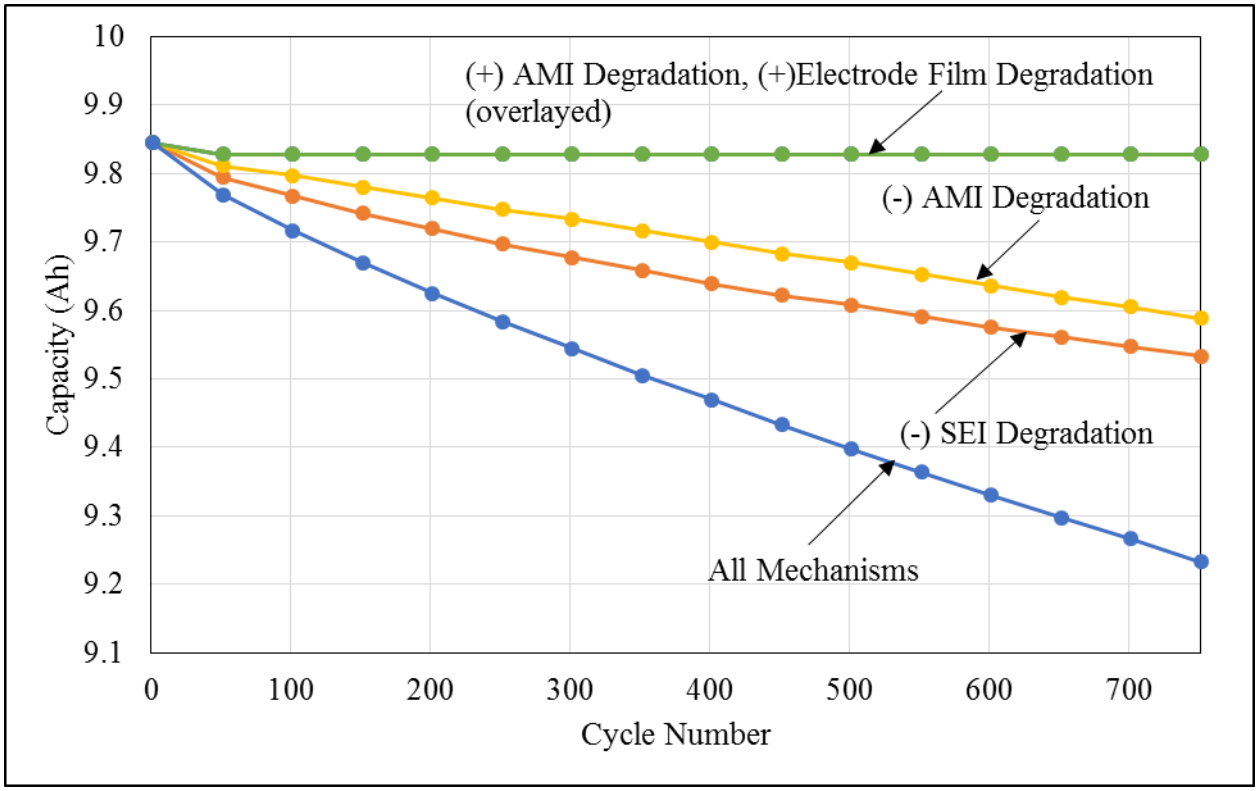

Figure 6-10: Comparison of effect of different degradation mechanisms on capacity fade using AutoLionST suggested parameters; 1C charge/discharge, 40˚C

The results clearly show that as SEI layer formation (on a negative electrode) and active material isolation of the negative electrode material are the key contributors to capacity fade, while degradation mechanisms at the positive electrode have little effect apart from a small drop in capacity in early cycles. Therefore, moving forward, the parameters for degradation mechanism only at the negative electrode would be studied.

For each of these mechanisms, there are two parameters which were varied: reference rate constant and activation energy. The first parameter to be varied is the reference rate constant for SEI layer formation. The parameter was varied over a large range from $1.3*10^{-20}$ m/s (orginial value) to $1.3*10^{-10}$ m/s. Figure 6-11 presents the results, note that the result for 30°C were also included as a reference. These batteries were all subject to 1C charge/discharge, under isothermal conditions with a battery temperature of 20˚C.

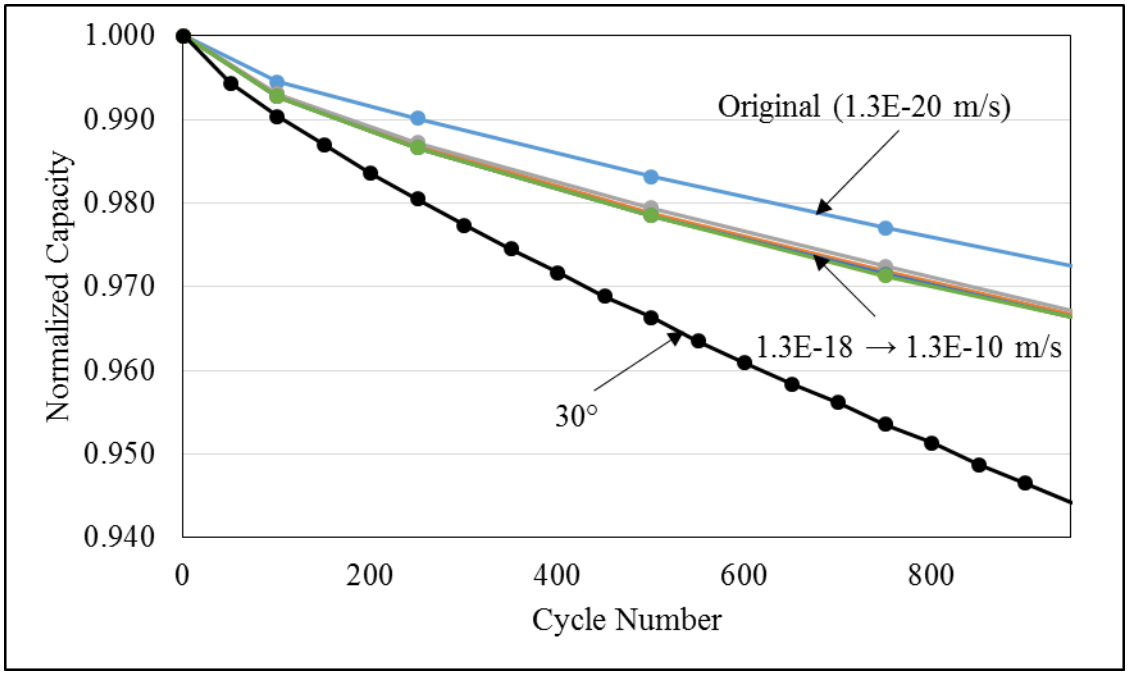

Figure 6-11: Normalized capacity fade at 20°C for a range of SEI layer formation rate constants; all refined values fall collapse onto same line, 30°C degradation shown for reference

Figure 6-11 shows that as the rate constant is increased there is very little variation once it reaches approximately $1.3*10^{-18}$ m/s. Although, when comparing these results to the original 20°C degradation results, there is very little change, so the other parameters must still be varied. Figure 6-12 shows the effect of varying the activation energy for the SEI layer formation. Figure 6-12 shows the effect of changing the SEI layer formation activation energy, even over orders of magnitude change has very little effect on the capacity fade. As a result, the activation energy was kept at the original value of $8.53*10^{4}$ J/mol.

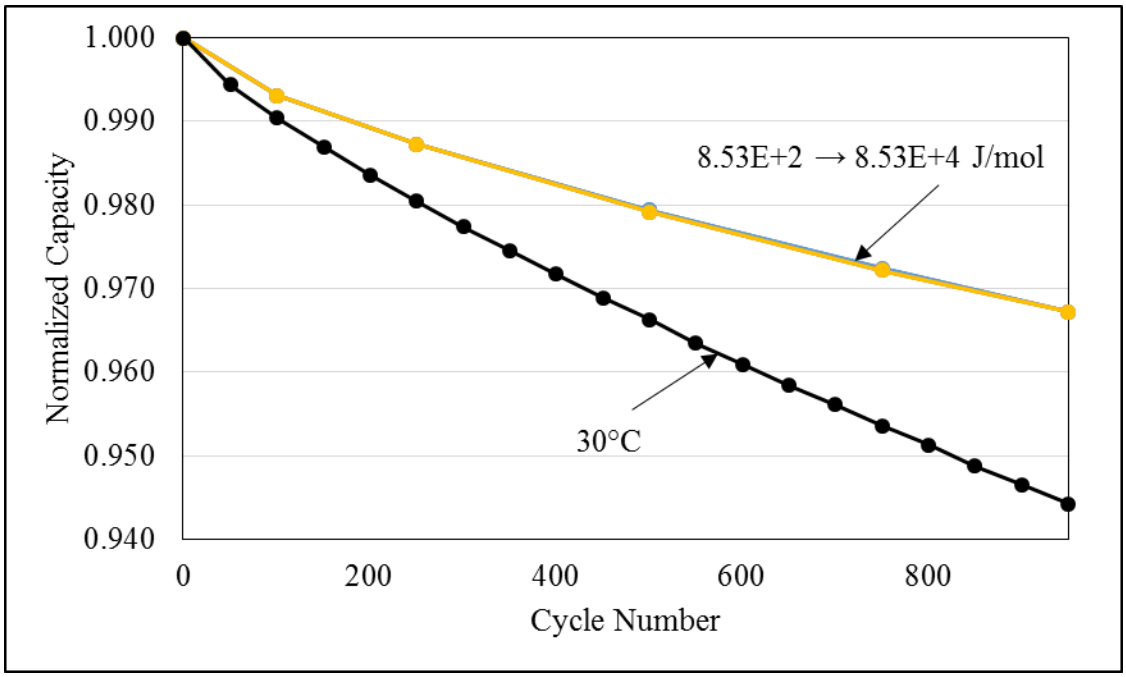

Figure 6-12: Normalized capacity fade at 20°C for a range of SEI layer formation activation energies, 30°C degradation shown for reference

A similar study was performed for the active material isolation (AMI) parameters. Varying the negative electrode AMI reference rate constant, the following plot was generated.

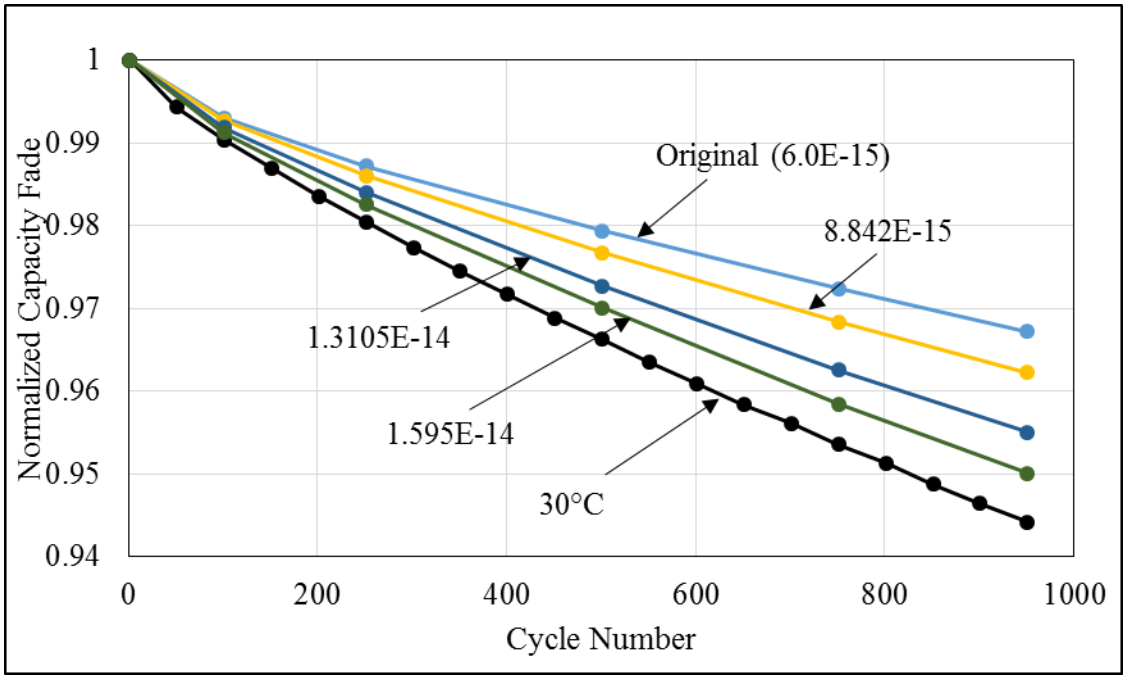

Figure 6-13: Normalized capacity fade at 20°C for a range of negative electrode AMI rate constants, 30°C degradation shown for reference

One point of interest is that battery degradation is extremely sensitive to small changes to the AMI reference rate constant when compared to the SEI layer formation reference rate constant. From these results a negative electrode rate constant of $8.842*10^{-15}$ J/mol was selected. The last parameter to be investigated is the activation energy for negative electrode AMI. These results can be seen in Figure 6-14; note that all these results were obtained by using the original reference rate constant of $6.0*10^{-15}$ J/mol.

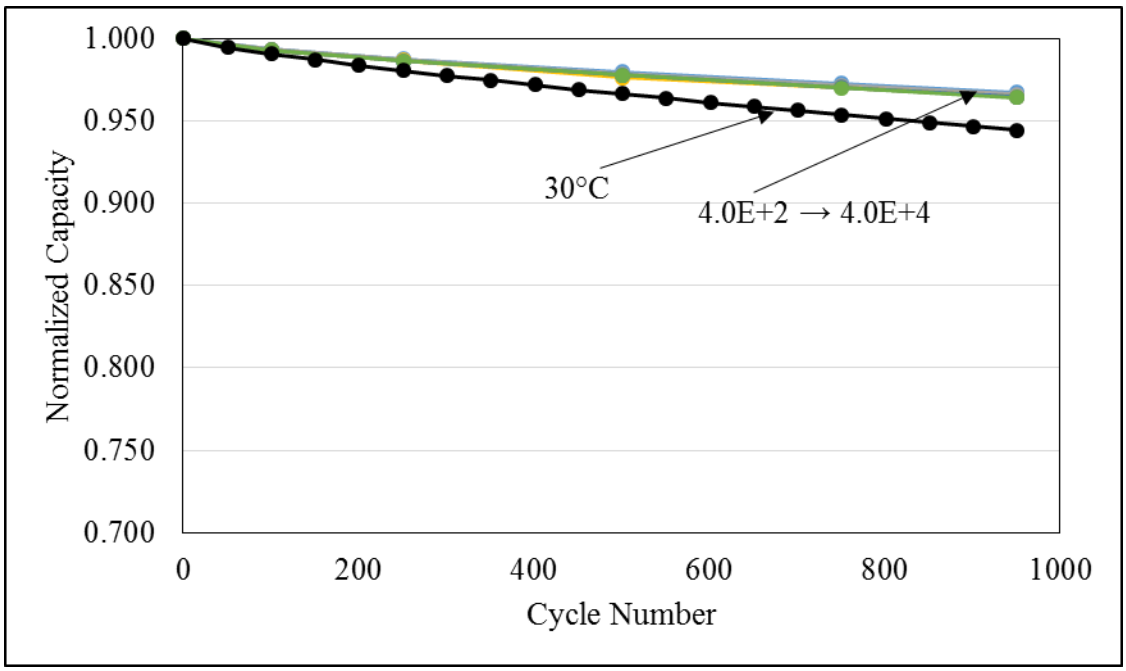

Figure 6-14: Normalized capacity fade at 20°C for a range of negative electrode AMI activation energies, 30°C degradation shown for reference

Similar to the results from SEI layer formation, it can be concluded that varying the negative electrode AMI activation energy even over orders of magnitude results in negligible change to the capacity fade. As a result, this parameter is to remain unchanged ($4.0*10^{4}$ J/mol). The current degradation parameters are summarized in Table 6-1.

Figure 6-15 shows the updated normalized capacity fade results using the updated parameters for batteries operating at 20°C. The results shown in Figure 6-15 have been deemed acceptable by the industry partner. Before degradation parameters are finalized, the AutoLionST model will first be refined using the experimental results.

Table 6-1: Degradation parameters used for 20°C cell simulations [64]

	Value for 20°C cell	Original Value	Units
Negative Electrode Film Growth			
Rate Constant	$1.3*10^{-18}$ m/s	$1.3*10^{-20}$	m/s
Activation Energy	Unchanged	$8.53*10^{4}$	J/mol
Positive Electrode Film Growth			
Rate Constant	Unchanged	$3.1*10^{-8}$	m/s
Activation Energy	Unchanged	$2.5*10^{4}$	J/mol
Negative Electrode AMI			
Rate Constant	$8.842*10^{-15}$	$6*10^{-15}$	m/s
Activation Energy	Unchanged	$4*10^{4}$	J/mol
Positive Electrode AMI			
Rate Constant	Unchanged	0	m/s
Activation Energy	Unchanged	$3*10^{4}$	J/mol

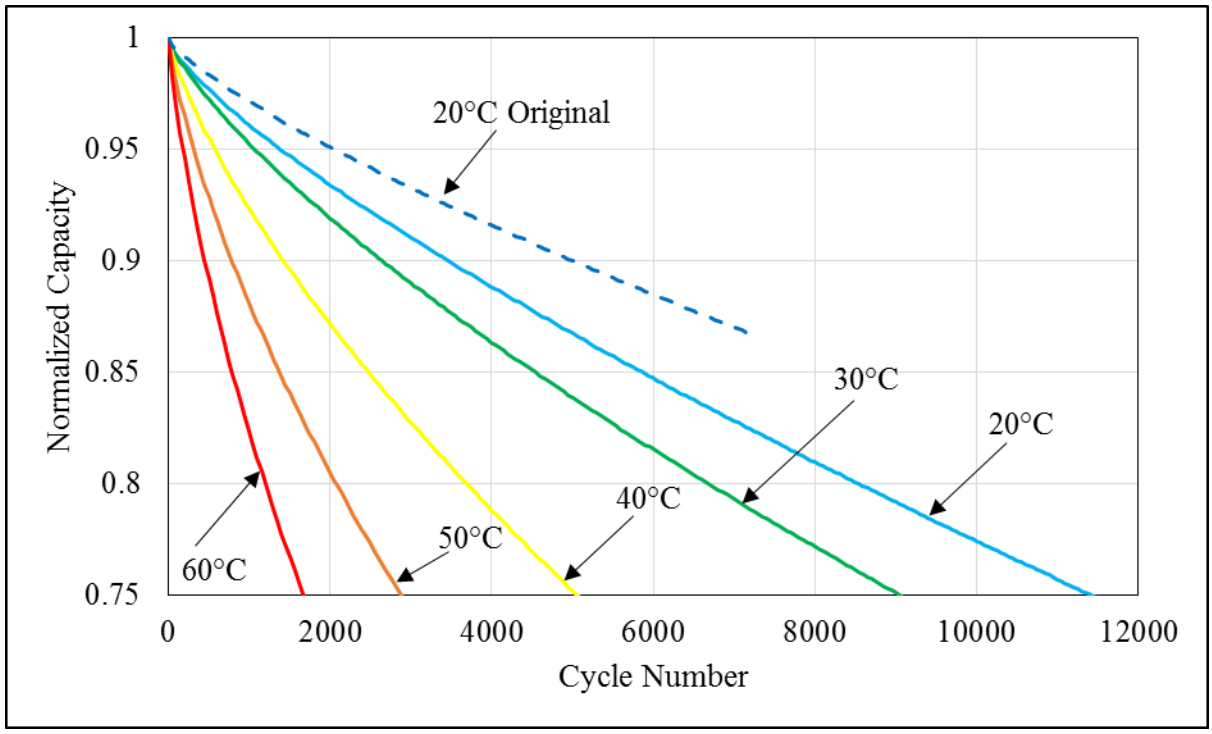

Figure 6-15: Normalized capacity fade results using updated degradation parameters at 20°C

6.3 Model Refinement

Following the parameter study, the model was refined in order to obtain good agreement between the experimental and simulation capacity fade results. Using the results of the parameter study, the degradation parameters were refined to reflect the experimental results. Similar to the parameter study shown in the last subsection, values of negative electrode

reference rate constant and activation energy were varied. Figure 6-16 shows updated 35°C isothermal results after refining the model to the experimental results.

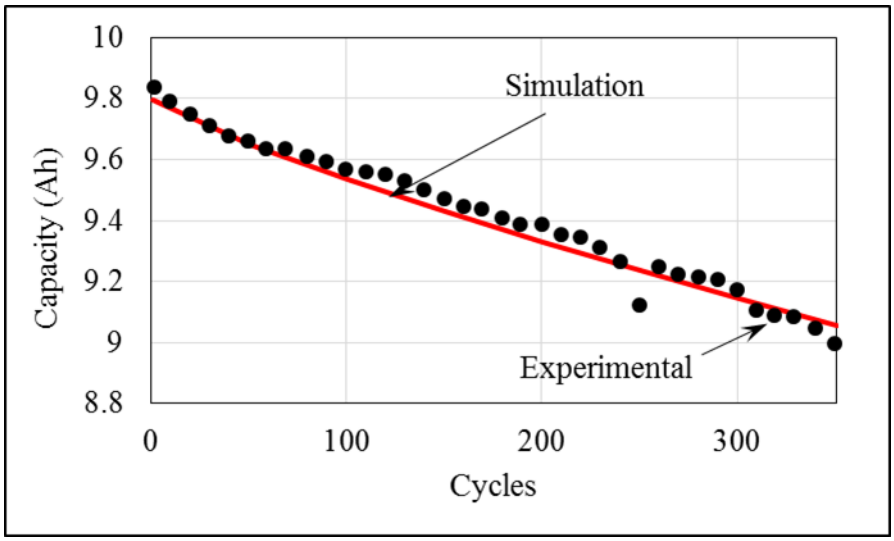

Figure 6-16: Comparison of experimental vs. simulation battery capacity following 1C charge/discharge at 35°C using refined degradation parameters

Table 6-2 shows the full list of updated degradation parameters following refinement with experimental data. After the experimental refinement was performed, the parameters at 20°C were again updated to provide the trends shown in Figure 6-15, but relative to the experimentally calibrated parameters. The listed parameters will be used for the remainder of the study.

Figure 6-17 shows the updated isothermal results using the parameters listed in Table 6-2, where appropriate. There are a few observations that can be made about these results. Firstly, and mostly obvious, is the dependence of the degradation on the battery temperature. It is clear that the initial capacity of the battery also strongly depends on cell temperature. These are both expected trends; a hotter battery provides higher initial capacity, but will degrade more quickly.

Using these degradation parameters based on experimental work, and external data, further results are obtained in Chapter 6. As mentioned in Chapter 5, further experimental work would be an ideal next step for this study. If further experimental data is collected, it would be possible to tune all parameters to the experimental data, rather than relying on the trends supplied by the industry partner.

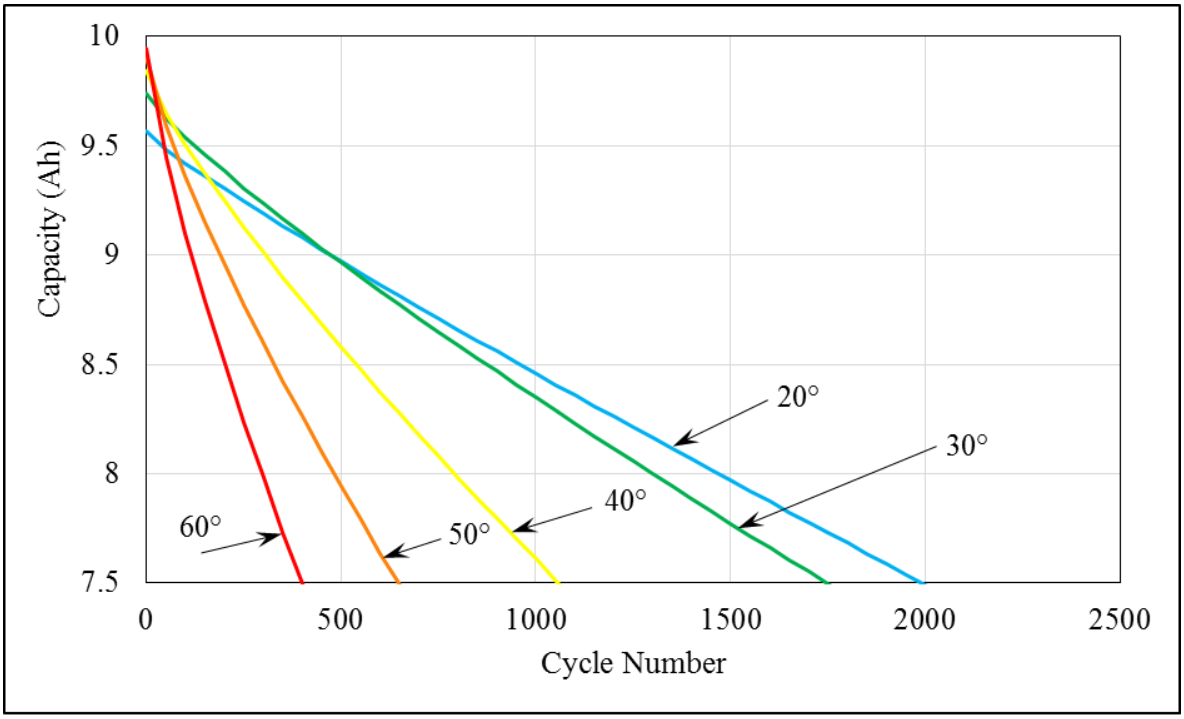

(a)

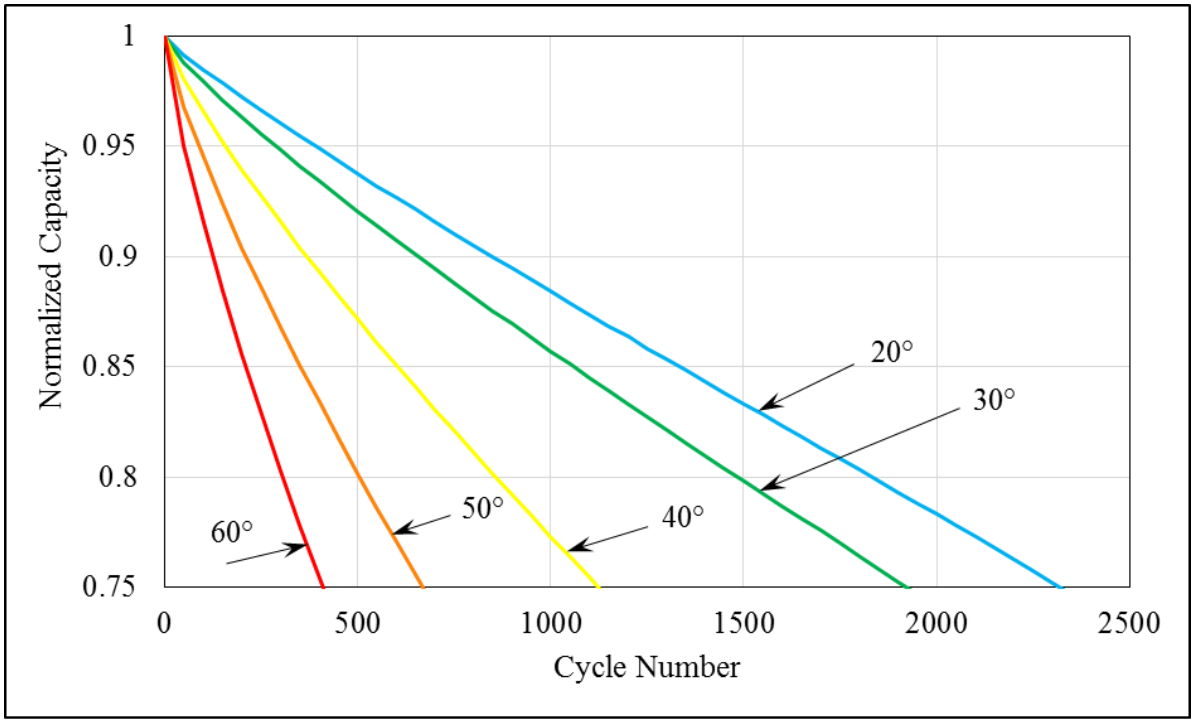

(b)

Figure 6-17: Battery capacity following 1C isothermal charge/discharge at various temperatures using tuned degradation parameters; (a) capacity; (b) normalized capacity

Table 6-2: Original (suggested) and tuned AutoLionST degradation parameters

	Tuned Parameters	Value for 20°C cell	Original Value	Units
Negative Electrode Film Growth				
Rate Constant	$1.30 *10^{-18}$	$1.30 *10^{-18}$	$1.30 *10^{-20}$	m/s
Activation Energy	Unchanged	Unchanged	$8.53 *10^{4}$	J/mol
Positive Electrode Film Growth				
Rate Constant	Unchanged	Unchanged	$3.10 *10^{-8}$	m/s
Activation Energy	Unchanged	Unchanged	$2.50 *10^{4}$	J/mol
Negative Electrode AMI				
Rate Constant	$3.47 *10^{-14}$	$5.11 *10^{-14}$	$6.00 *10^{-15}$	m/s
Activation Energy	Unchanged	Unchanged	$4.00 *10^{4}$	J/mol
Positive Electrode AMI				
Rate Constant	Unchanged	Unchanged	0	m/s
Activation Energy	Unchanged	Unchanged	$3.00 *10^{4}$	J/mol

6.4 Numerical Implementation

Finally, before the main results are presented, this subsection will briefly discuss the numerical implementation of the model.

Since the model employs a lumped thermal analysis, the conservation of energy Equation (25) is not discretized in space, but just solved at each time step [57]. As mentioned previously, properties and current distribution, concentration, and overpotential are assumed constant over the cell height, therefore the solid-phase conservation of charge, electrolyte-phase conservation of charge, and conservation of electrolyte-phase Li^+ species are all discretized once in space through the thickness of the cell (normal to the cell height) [57]. The conservation of active material Li species is discretized in the radial direction of a particle of active material [57]. These equations discretized in space all utilize a finite control volume method [57].

The user can specify the number of volumes in three mesh zones: the negative electrode, separator, and positive electrode, with default mesh numbers being 8, 5, and 8, respectively [57]. Note that the number of volumes in a given zone cannot exceed 100 [57]. A mesh refinement study is performed to observe any significant change in results due to mesh numbers; like the entire study, the result of interest is the battery capacity.

These simulations for mesh refinement were performed using the same method as the previous simulation presented in this chapter. Mesh refinements were performed at 1C charge/discharge, and at 1C charge / 2C discharge. All mesh refinement simulations were done at 35°C. The mesh study used mesh sizes of 8/5/8 (positive electrode/separator/negative electrode), 16/10/16, 40/25/40, and 80/50/80. Results below show the effect of mesh size on cell voltage and current over a single cycle, and capacity over a period of cycling. Figure 6-18 shows the voltage and current profiles for the first cycle for all simulations of different mesh sizes, for 1C and 2C discharge.

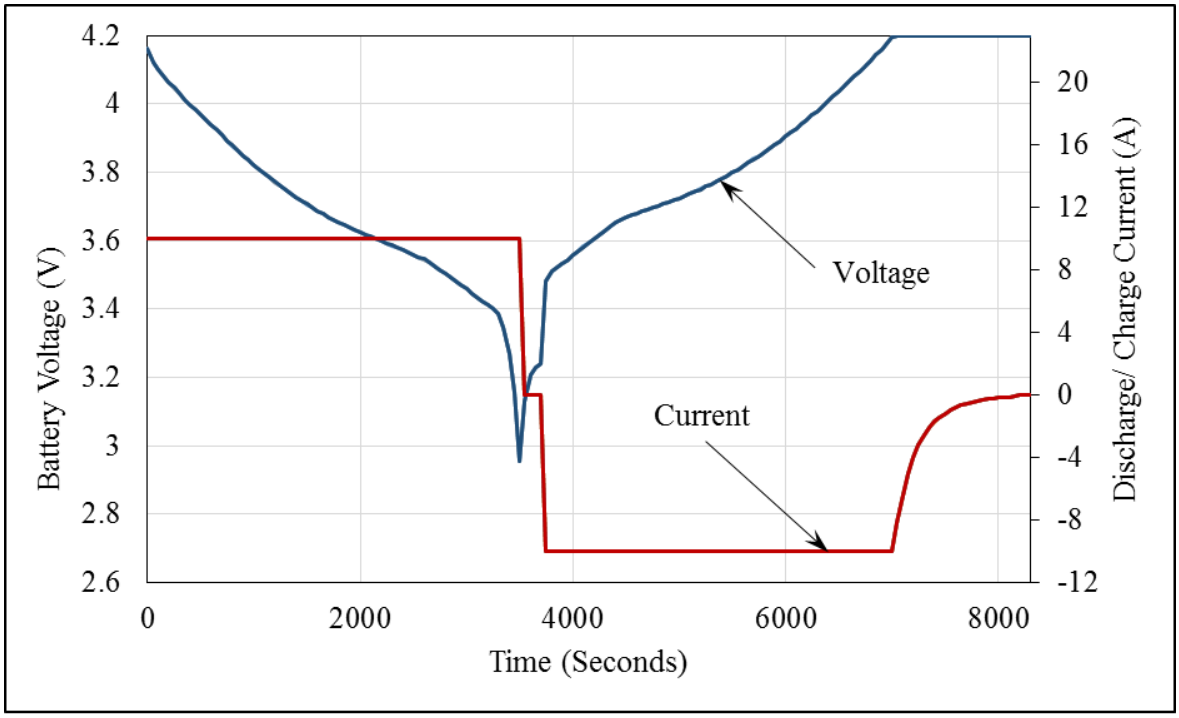

(a)

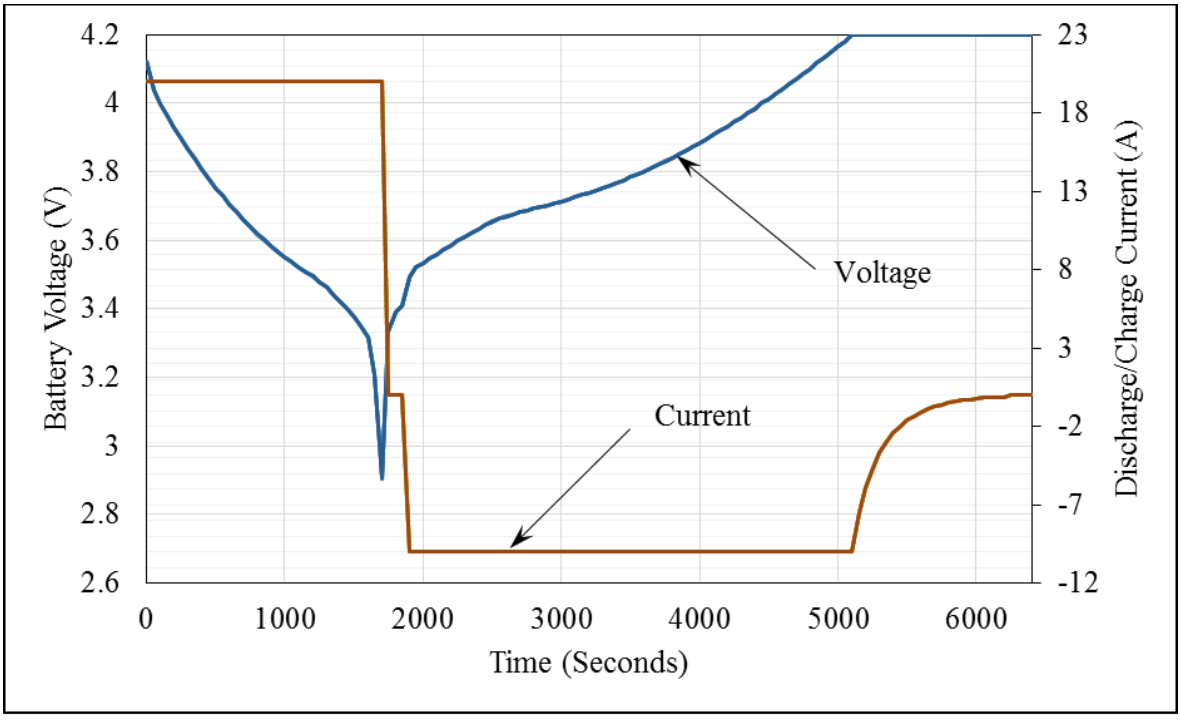

(b)

Figure 6-18: Voltage and current profiles from mesh refinement simulations employing meshes of 8/5/8, 16/10/16, 40/25/40, and 80/50/80: (a) 1C discharge; (b) 2C discharge

Figure 6-18 shows no noticeable difference in battery voltage when applying the same current loads between different mesh sizes.

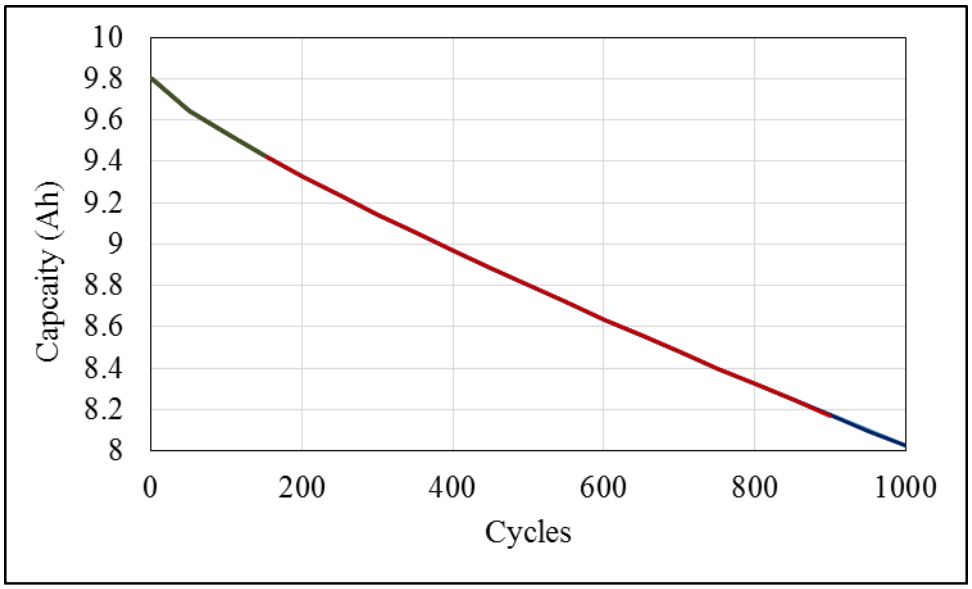

(a)

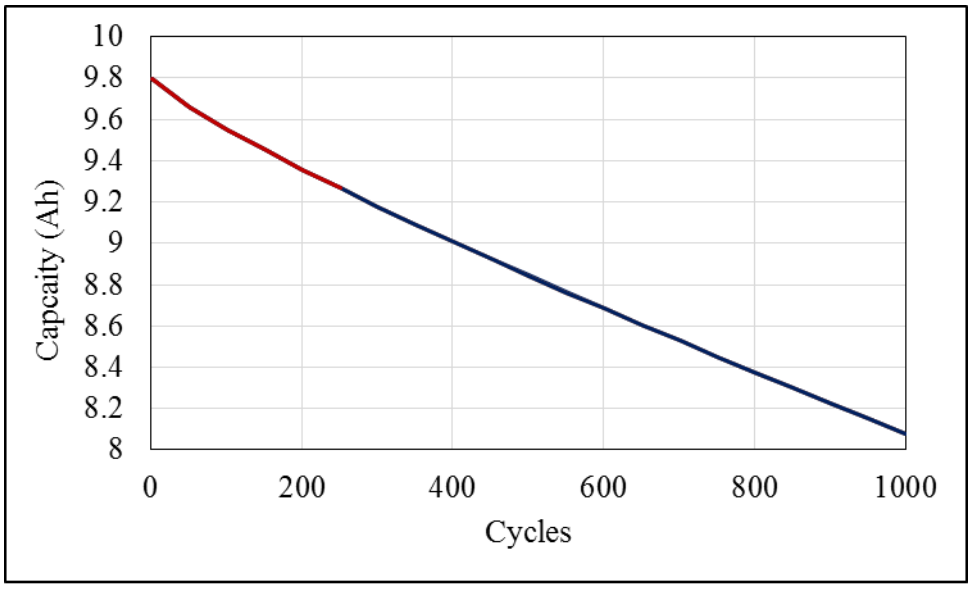

(b)

Figure 6-19: Capacity fade curves from mesh refinement simulations employing meshes of 8/5/8, 16/10/16, 40/25/40, and 80/50/80, 1C charge/discharge, and 35°C: (a) 1C discharge; (b) 2C discharge

As seen in Figure 6-19, there is no identifiable variation when using a finer mesh (relative to the default values). For this reason, the default mesh values will continue to be used. It should

also be noted that in terms of processing time, with the default mesh 100 1C charge/discharge cycles takes approximately one hour to simulate, and by a mesh which is ten times finer, simulations run approximately in real time (one cycle takes approximately two hours). This excessive time would be unacceptable from simulation work.

Now that the preliminary work has been discussed, they next section will present the results obtained.

7 Model Results & Discussion

Following the parameters adjustment, full results for the different cases of interest will now be presented.

7.1 Constant C-Rate Cycling Results

The first section of results will observe capacity fade of batteries subject to different discharge rates; the effect of thermal management (i.e. cooling rate) on capacity fade will be discussed. As mentioned earlier, batteries were simulated at three different temperatures; 20°C, 35°C, and 50°C. In simulations, the initial battery temperature and temperature with which heat transfer occurs are both set at the specified value (i.e. $T_{amb} = T_0$ = 20°C, 35°C, or 50°C). Cycling is done by discharging at one of three given rates of 1C, 2C, or 4C from 4.2V to 2.75V, and charging the battery back to 4.2V. Eight hour rest periods were used in between each discharge/charge and charge/discharge period in order for the cell to reach steady-state temperature conditions. Three different heat transfer coefficients are used to represent three different thermal management strategies. As a reminder, the three strategies are air cooled by free convection, using an ICE plate with air as the working fluid, and using an ICE plate with a liquid coolant. All combinations of battery temperature, discharge rate, and thermal management strategy were considered, leading to 27 unique simulations. These simulations consider the failure criteria of a battery to when the battery has reached 75% of the original capacity; as a result, all successive results will be presented using normalized capacity. The results of these tests are shown below in Figure 7-1 to Figure 7-3:

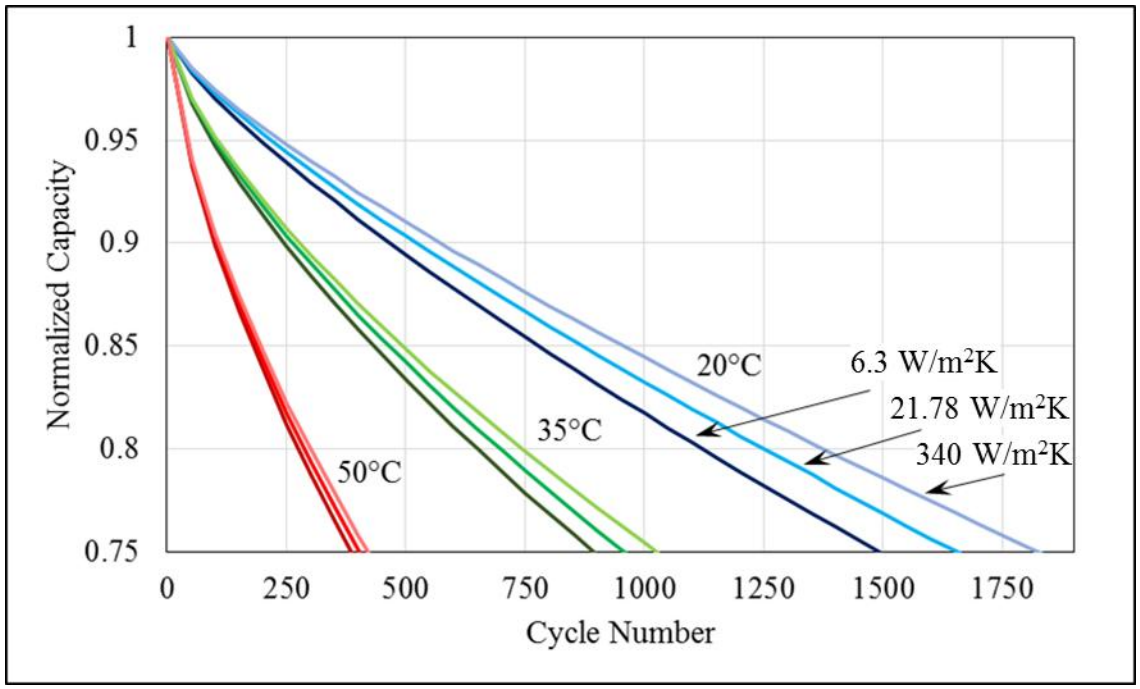

Figure 7-1: Normalized capacity of batteries cycled at 1C discharge/ 1C charge, with three different specified temperatures, and three different heat transfer coefficients

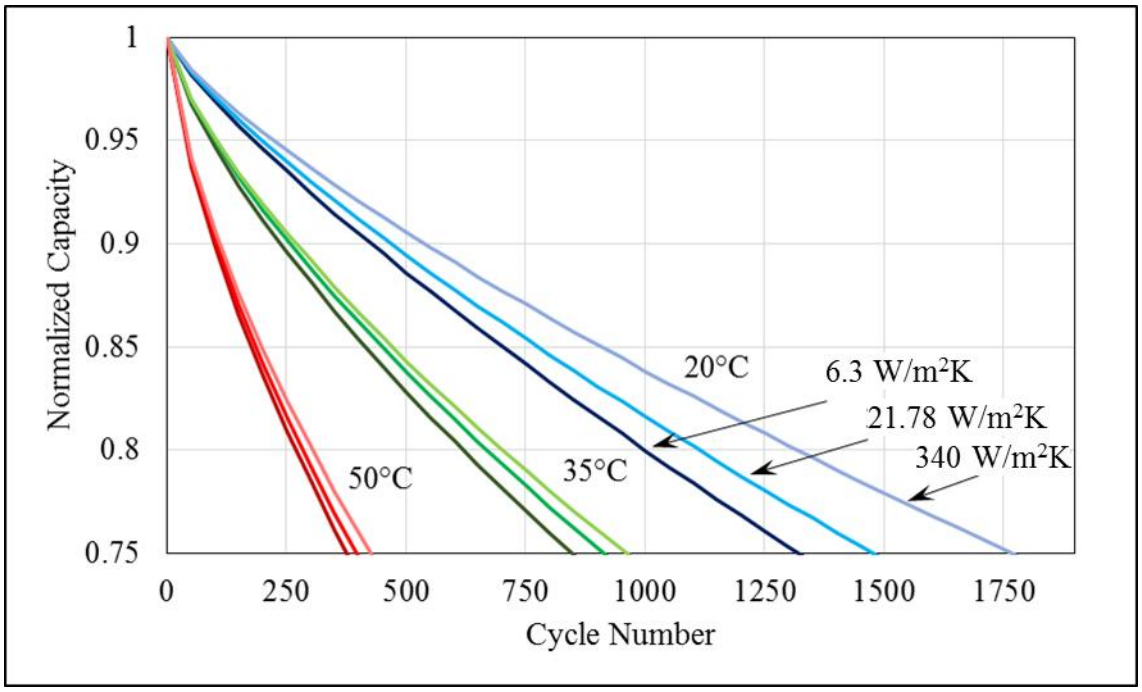

Figure 7-2: Normalized capacity of batteries cycled at 2C discharge/ 1C charge, with three different specified temperatures, and three different heat transfer coefficients

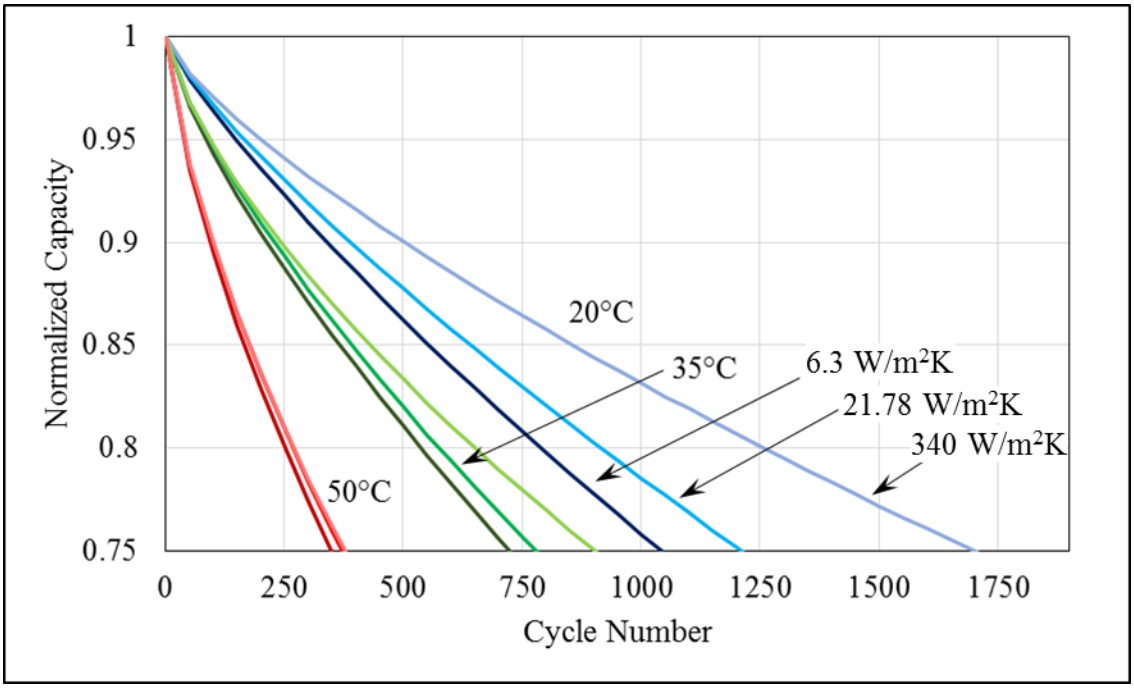

Figure 7-3: Normalized capacity of batteries cycled at 4C discharge/ 1C charge, with three different specified temperatures, and three different heat transfer coefficients

The first observation to make from Figure 7-1 to Figure 7-3 is that all indicate that overall cell temperature is still the most significant factor in battery capacity fade. With the exception of Figure 7-3 (with very high C-rate) all plots show a very clearly defined “band” of curves each

representing the specified battery temperature. On each plot, it can also be seen that the heat transfer coefficient has a significant impact on capacity fade, notably at lower temperatures; this need for effective cooling shows a strong interaction with discharge rate, again, notably at lower temperatures. Table 7-1 demonstrates the percent differences in cycles to failure (75% of original capacity) for batteries at 20°C.

Table 7-1: Comparison of cycles to failure between heat transfer coefficients at different C-rates; specified temperature of 20°C

	Heat Transfer Coefficients Compared	
C-Rate	6.3, 340 W/m^{2}K	21.78, 340 W/m^{2}K
1C	22%	10%
2C	34%	20%
4C	63%	40%

Table 7-1 clearly shows that at high C-rates, effective thermal management will significantly improve cycle life. To outline the capability of the different thermal management systems, Figure 7-4 to Figure 7-6 show the temperature increase during a single discharge for different C-rates for the central temperature of 35°C. These figures agree with Table 7-1, showing that high C-rate operations show a high need for effective thermal management.

Table 7-2,

Table 7-3, and Table 7-4 on summarize the temperature rise curves shown in Figure 7-4 to Figure 7-6, as predicted by the capacity fade curves, under every C-rate/heat transfer coefficient combination, the battery with the initial temperature of 20°C always experiences the highest temperature rise.

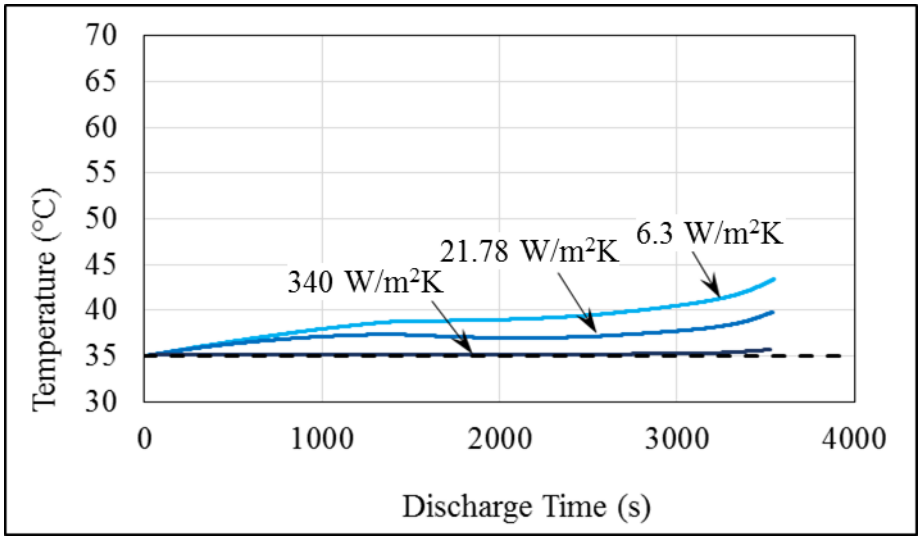

Figure 7-4: Temperature rise during discharge; 1C discharge, specified temperature of 35°C

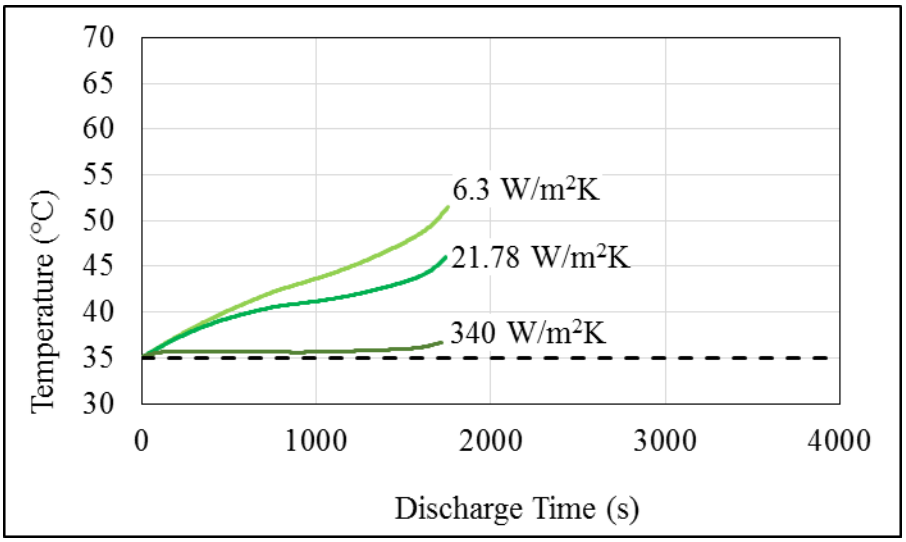

Figure 7-5: Temperature rise during discharge; 2C discharge, specified temperature of 35°C

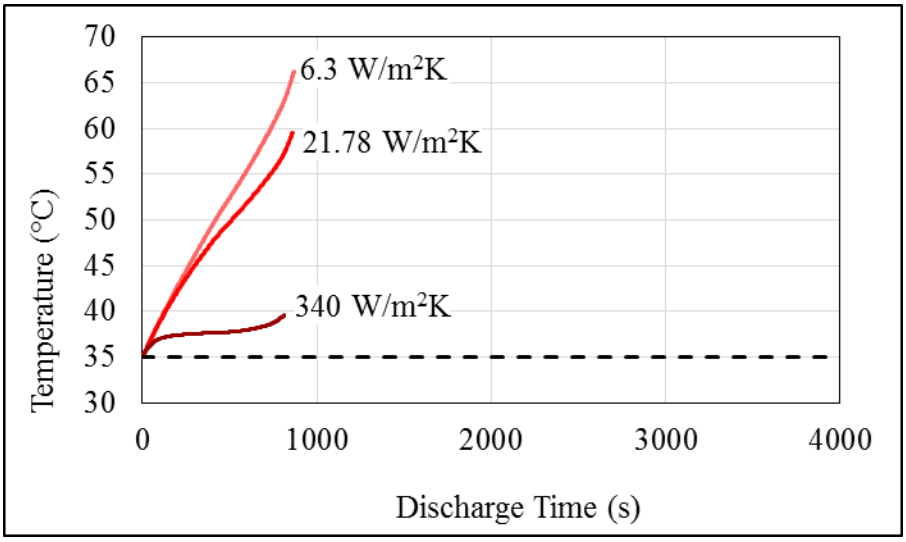

Figure 7-6: Temperature rise during discharge; 4C discharge, specified temperature of 35°C

Table 7-2: Temperature rise in batteries cycled using the specified discharge rate and heat transfer coefficient; T_0 = 20°C

Maximum Temperature Difference (K)			
	Heat Transfer Coefficient (W/m²K)		
C-Rate	**6.3**	**21.78**	**340**
1C	10.7	5.8	0.7
2C	20.0	13.8	1.9
4C	37.1	27.6	5.4

Table 7-3: Temperature rise in batteries cycled using the specified discharge rate and heat transfer coefficient; T_0 = 35°C

Maximum Temperature Difference (K)			
	Heat Transfer Coefficient (W/m²K)		
C-Rate	**6.3**	**21.78**	**340**
1C	8.4	4.8	0.7
2C	16.5	11.0	1.7
4C	31.2	24.5	4.6

Table 7-4: Temperature rise in batteries cycled using the specified discharge rate and heat transfer coefficient; T_0 = 50°C

Maximum Temperature Difference (K)			
	Heat Transfer Coefficient (W/m²K)		
C-Rate	**6.3**	**21.78**	**340**
1C	7.1	4.2	0.7
2C	13.6	9.1	1.5
4C	25.4	20.0	3.8

Another observation to point out is that apart from discussing battery degradation, many of the batteries listed in the previous tables would approach thermal runaway, which is one of the greatest possible dangers in lithium-ion battery operation.

7.2 Drive Cycle Simulation Results

7.2.1 Drive Cycle Simulations; Regenerative Braking Neglected

As mentioned in the methodology, drive cycle simulations will draw the energy requirements from the battery assuming an FTP drive cycle. Power requirements were calculated using mechanics, assuming the vehicle in question has properties similar to that of a Chevrolet Volt.

As a reminder, the overall drive cycle applied is meant to represent a single day use of the vehicle. A single cycle is summarized below:

- Eight hour rest period (overnight)
- FTP drive cycle (drive to work)
- Eight hour rest period (at work)
- FTP drive cycle (drive home)
- Three minute rest period (rest period before charging)
- 1C-CCCV charge period

This cycle allows the battery temperature to come to a steady value between discharges. Similar to the C-rate analysis, the same three specified temperatures were considered (set as initial and thermal management temperature), and the same three heat transfer coefficients

were considered. Three fully charged voltages of 4.0, 4.1, and 4.2 V are considered. As well as a reminder, since this is a fixed-time load, an additional failure criterion is considered; failure is defined as when the battery reaches 75% of original capacity *or* the battery is unable to complete the entire drive cycle. This second condition is defined as the voltage dropping below the specified minimum battery voltage of 3.0V. Figure 7-7 to Figure 7-9 show the results of this analysis.

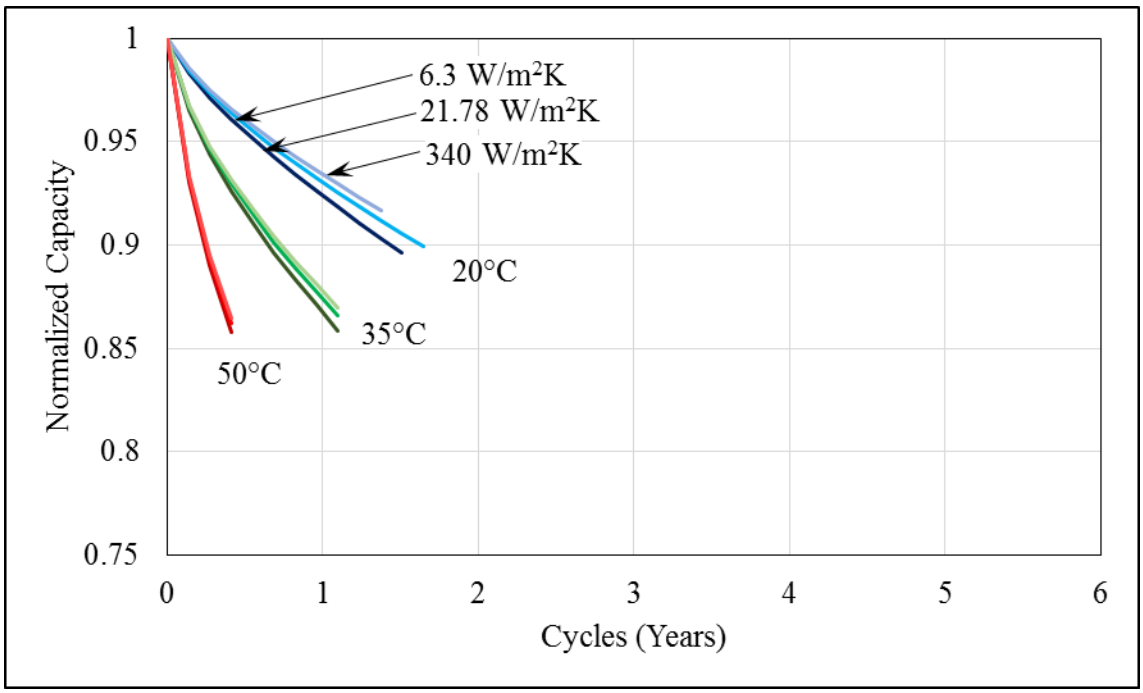

Figure 7-7: Normalized capacity of batteries cycled with an FTP drive cycle and maximum voltage of 4.0V; three different specified temperatures, and three different heat transfer coefficients

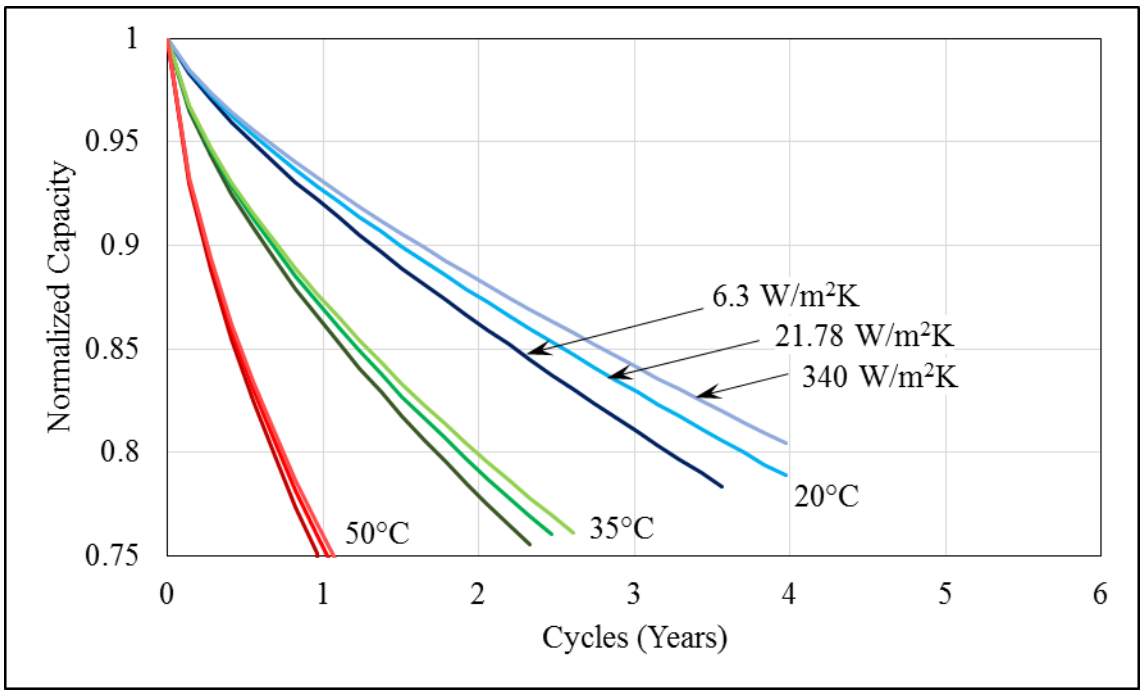

Figure 7-8: Normalized capacity of batteries cycled with an FTP drive cycle and maximum voltage of 4.1V; three different specified temperatures, and three different heat transfer coefficients

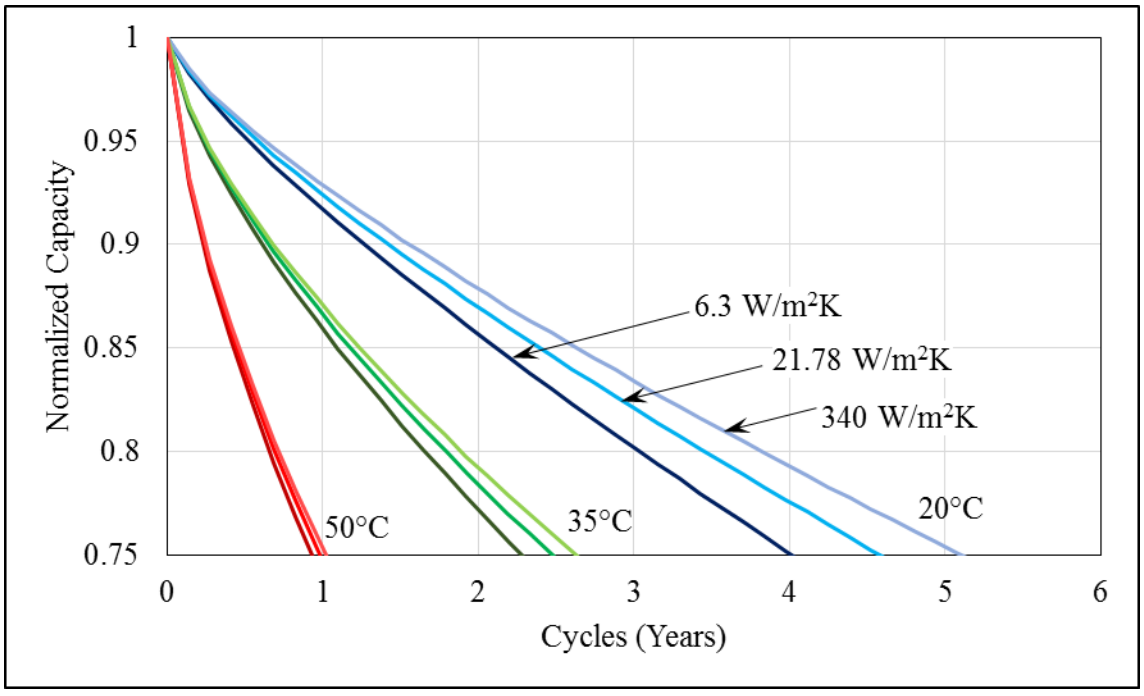

Figure 7-9: Normalized capacity of batteries cycled with an FTP drive cycle and maximum voltage of 4.2V; three different specified temperatures, and three different heat transfer coefficients

Conclusions drawn are similar to those from the C-rate analysis. Battery temperature is the dominant factor effecting capacity fade, while thermal management system has a significant effect at lower temperatures. The obvious effect of charge voltage is that batteries with less charge are prone to degrade to the point where they cannot provide the required energy. Note that this can be designed around as the battery pack in these simulations is relatively small (288 10Ah cells), and this analysis also does not factor in the hybrid nature of the Chevrolet Volt. Since some batteries did not get close to the 75% failure criteria, the effect of charge voltage on capacity fade cannot easily be observed.

Figure 7-10 demonstrates the effect of charge voltage by plotting curves representing different charge voltages on a single plot. In Figure 7-10, batteries with temperatures of 20°C and 35°C are shown, all employing a heat transfer coefficient of 6.3 W/m^{2}K.

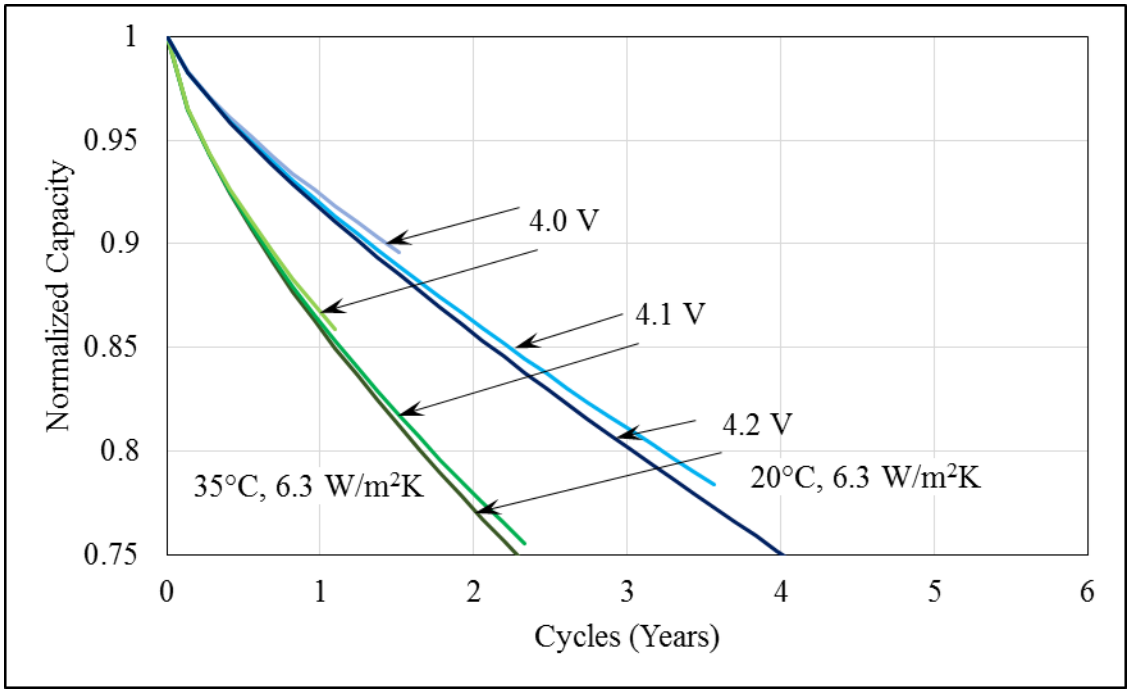

Figure 7-10: Normalized capacity of batteries cycled with drive cycle and specified temperature of 20°C and 35°C; three different maximum voltages, and heat transfer coefficient of 6.3 W/m^{2}K

While the curves in Figure 7-10 are not complete, since the minimum voltage criteria was reached, it appears that a higher charge voltage results in a more capacity fade (though not a significant increase).

7.2.2 Drive Cycle Simulations; Regenerative Braking Included

Finally, Figure 7-11 to Figure 7-13 show similar results but instead using the same FTP drive cycle regenerative braking.

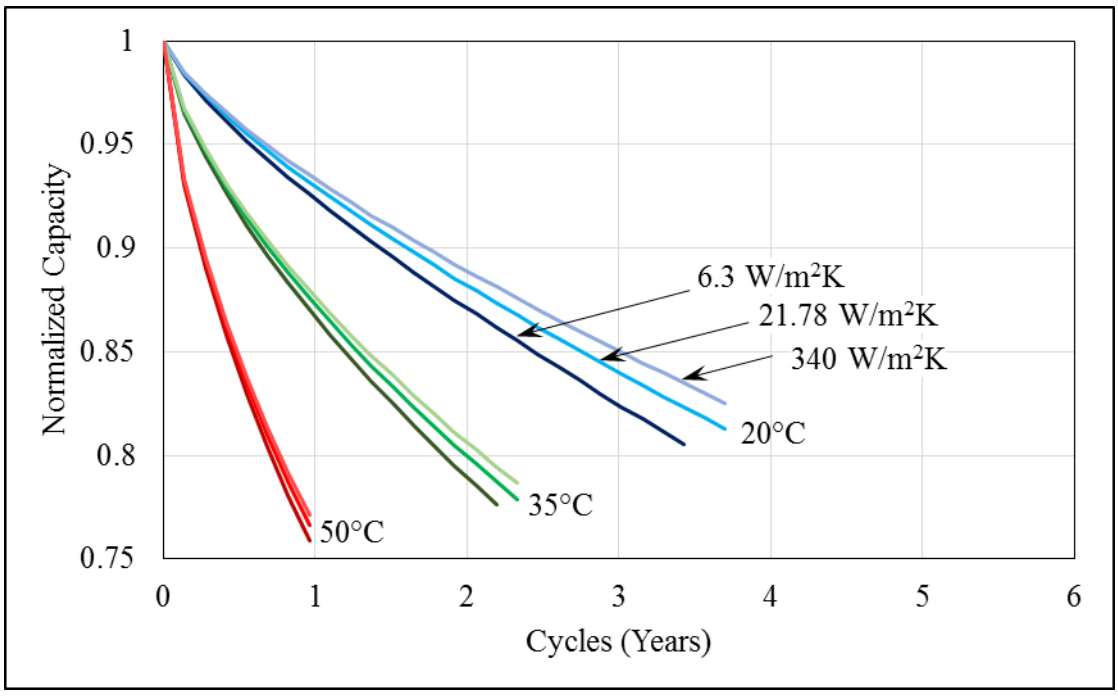

Figure 7-11: Normalized capacity of batteries cycled with drive cycle with regenerative braking and maximum voltage of 4.0V; three different specified temperatures, and three different heat transfer coefficients

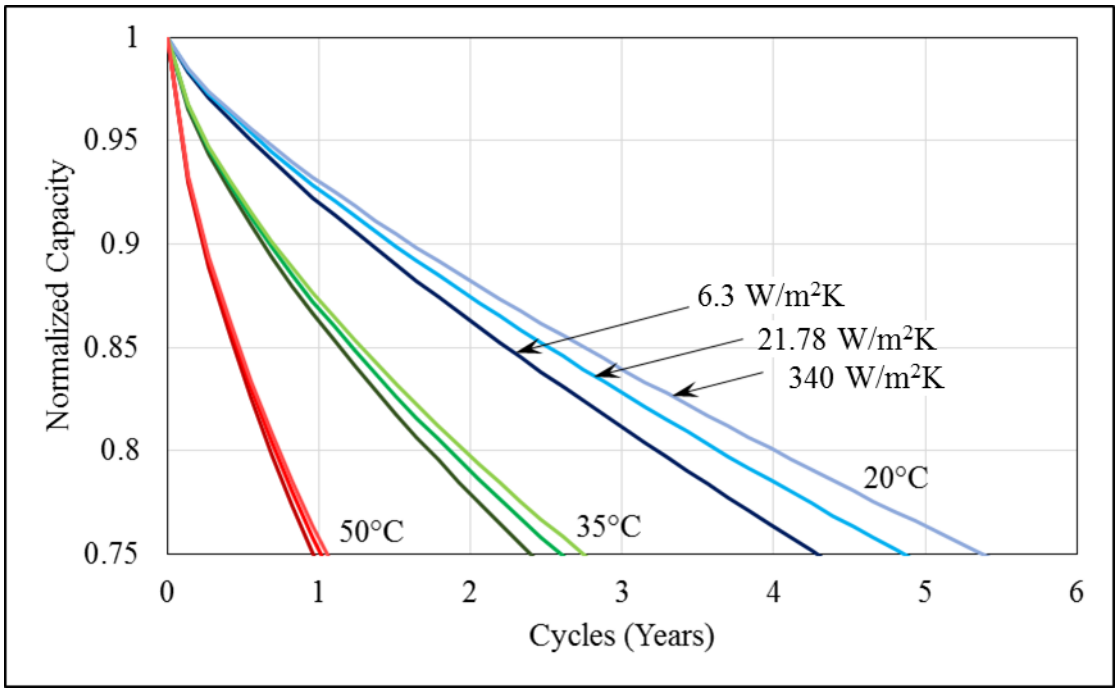

Figure 7-12: Normalized capacity of batteries cycled with drive cycle with regenerative braking and maximum voltage of 4.1V; three different specified temperatures, and three different heat transfer coefficients

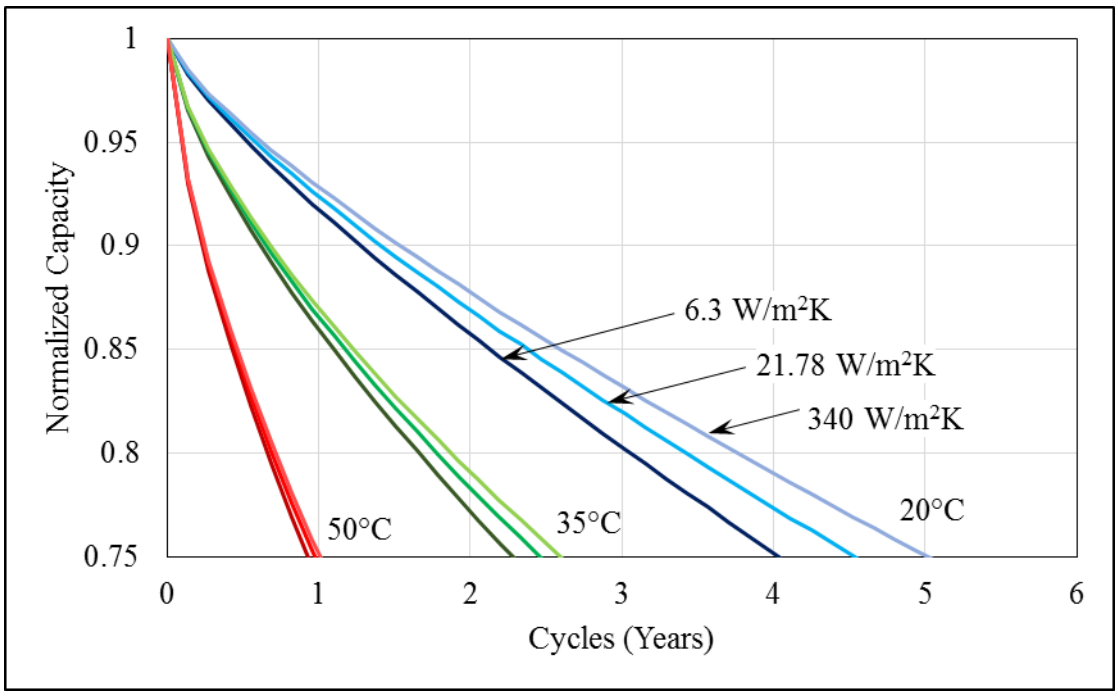

Figure 7-13: Normalized capacity of batteries cycled with drive cycle with regenerative braking and maximum voltage of 4.2V; three different specified temperatures, and three different heat transfer coefficients

As before, there is clear "band" encompassing batteries cycled at the same initial temperature. As well, it can again be seen that thermal management system has a significant effect on battery capacity, especially at lower temperatures. As shown in earlier tables, this is a result of higher heat generation, and subsequent temperature increase seen in batteries at lower temperature. It can therefore be concluded that it is very important to implement an effective thermal management strategy in electric vehicles. While many would assume that thermal management systems would be crucial only in unfavourable environments, such as very warm or cold climates, it is shown here that effective management can greatly reduce ageing effects even under reasonable conditions. This is evident in Figure 7-13 where it is shown that battery life can be extended by 25% between ineffective and effective thermal management, in a favourable environment of 20°C.

The most notable difference after including regenerative braking is the improved ability to deliver the desired charge. Comparing Figure 7-7 and Figure 7-11 it can be seen that it takes many more cycles before any batteries reach the minimum voltage failure. Since batteries at differing voltages have now both reached 75% of their capacity, Figure 7-14 is a better indicator of whether or not voltage is a significant contributor to capacity fade:

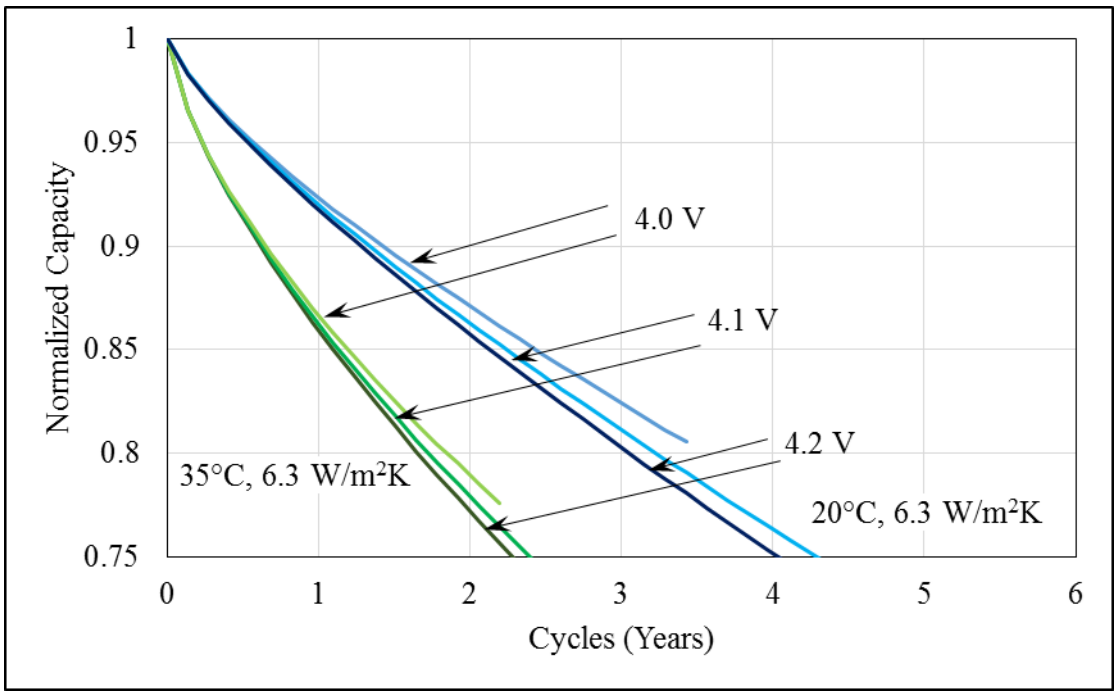

Figure 7-14: Normalized capacity of batteries cycled with drive cycle with regenerative braking and specified temperature of 20°C and 35°C; three different maximum voltages, and heat transfer coefficient of 6.3 W/m^{2}K

Figure 7-14 demonstrates that charge voltage does have a minor effect on capacity fade, as lower charge voltage in less capacity fade. These results agree with the results shown by Ramadass et al. [39], where they showed that a lower EOCV (end-of-charge voltage) resulted in less capacity fade.

7.2.3 Effect of Driving Style

One final note to make is regarding driving style; to apply results to real applications it should be noted that driving style can significantly affect the required load on the battery pack. In the previous drive cycle analyses, only the FTP drive cycle was considered. The FTP-75 drive cycle is known to have some shortcomings in representing true driving conditions, namely a lack of high acceleration and high speeds [70, 71]. Other drive cycles have been developed in an attempt to make up for this shortcoming [26, 29]. Some of these other standard drive cycles are shown in Table 7-5.

As seen in Table 7-5, the other drive cycles used have more demanding energy requirements, and represent different driving styles. The LA92 drive cycle is very similar to the FTP drive cycle, just with overall higher speeds, less idling, and higher acceleration. US06 is a very intense but short driving cycle with very high speeds and accelerations. The US06 drive cycle was developed, as a supplemental cycle to the FTP cycle as it was believed the FTP drive cycle was lacking in representing real world aggressive driving [71]. Figure 7-15 now shows a comparison of the average and maximum C-rates generated by other drive cycles. In this analysis, the FTP+US06 drive cycle was generated to reflect a period of calmer city driving to

a period of intense highway driving. The 2xUS06 drive cycle is merely two consecutive US06 drive cycles; this was done to have an intense drive cycle with a more comparable time period to the FTP cycle.

Table 7-5: Drive cycle characteristics [65]

Drive Cycle	Duration(s)	Distance(km)	Average speed(km/hr)	Top speed(km/hr)
FTP	1875	17.8	34.1	91.2
US06	601	12.9	77.8	129.2
LA92	1436	15.8	39.6	108.1
FTP+US06	2476	30.7	44.7	100.4
2 US06	1202	25.8	77.8	129.2

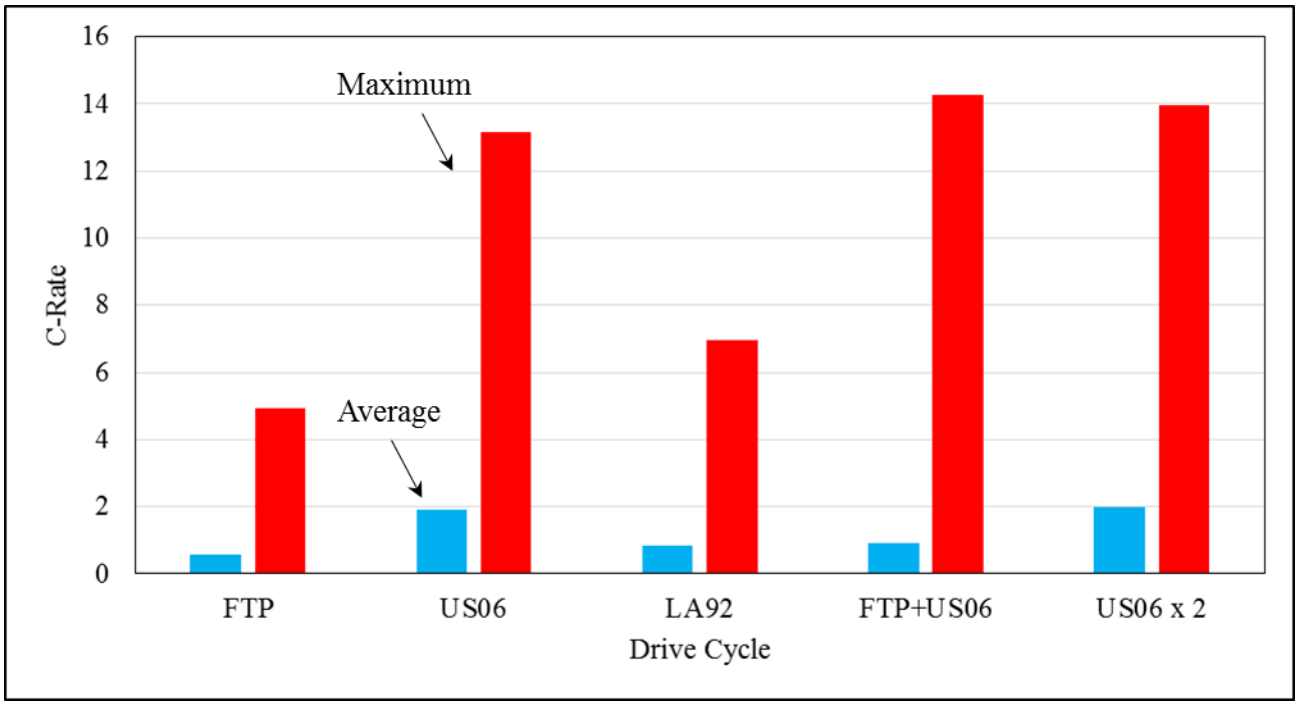

Figure 7-15: Comparison of C-rates for different drive cycles; data taken at 20°C with h = 6.3 W/m^{2}K, charge voltage of 4.2V

As seen by Figure 7-15, driving style can have a large impact on the required battery load, and hence the C-rate. As concluded earlier, namely in Table 7-1, there is a significantly higher need for effective thermal management with higher C-rates. Therefore, it is expected that more intense driving styles will result in a higher need for effective cooling strategies.

Figure 7-16 and Figure 7-17 show the average battery temperature and maximum battery temporal temperature change under the different drive cycles and different heat transfer coefficients with an initial temperature of 35°C.

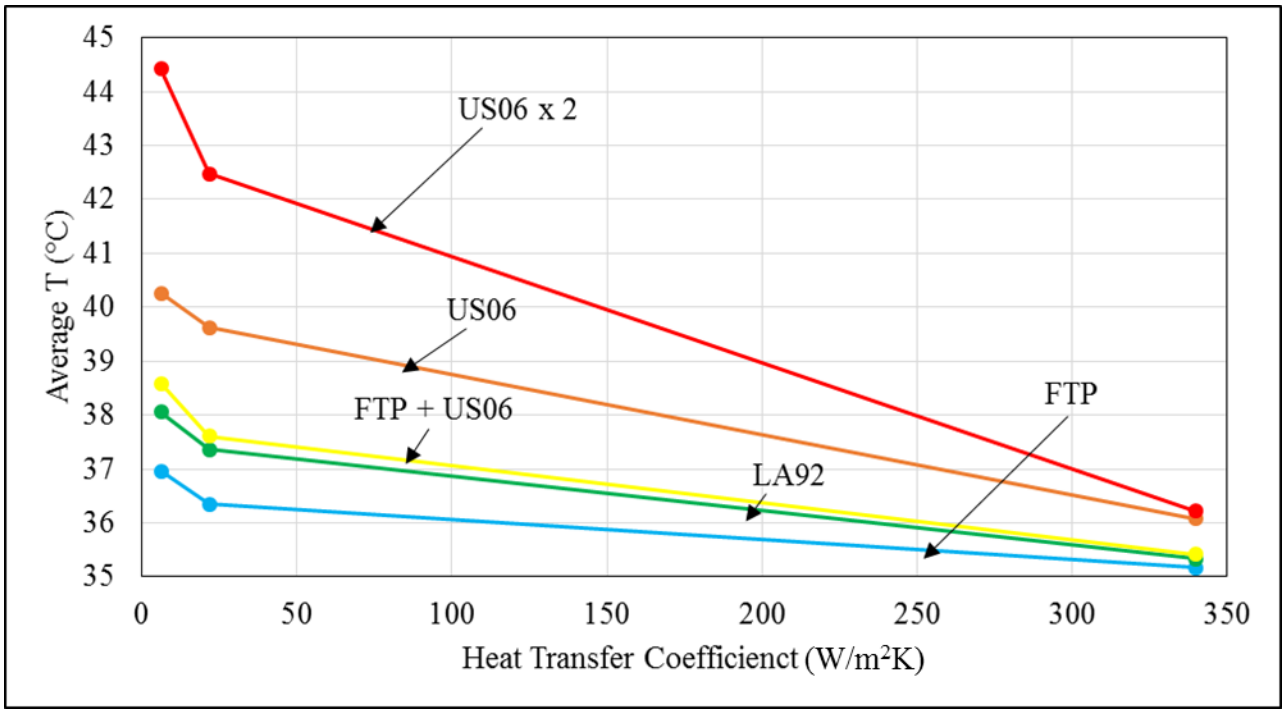

Figure 7-16: Average temporal cell temperature for a single drive cycle with varying heat transfer coefficients; initial temperature of 35°C

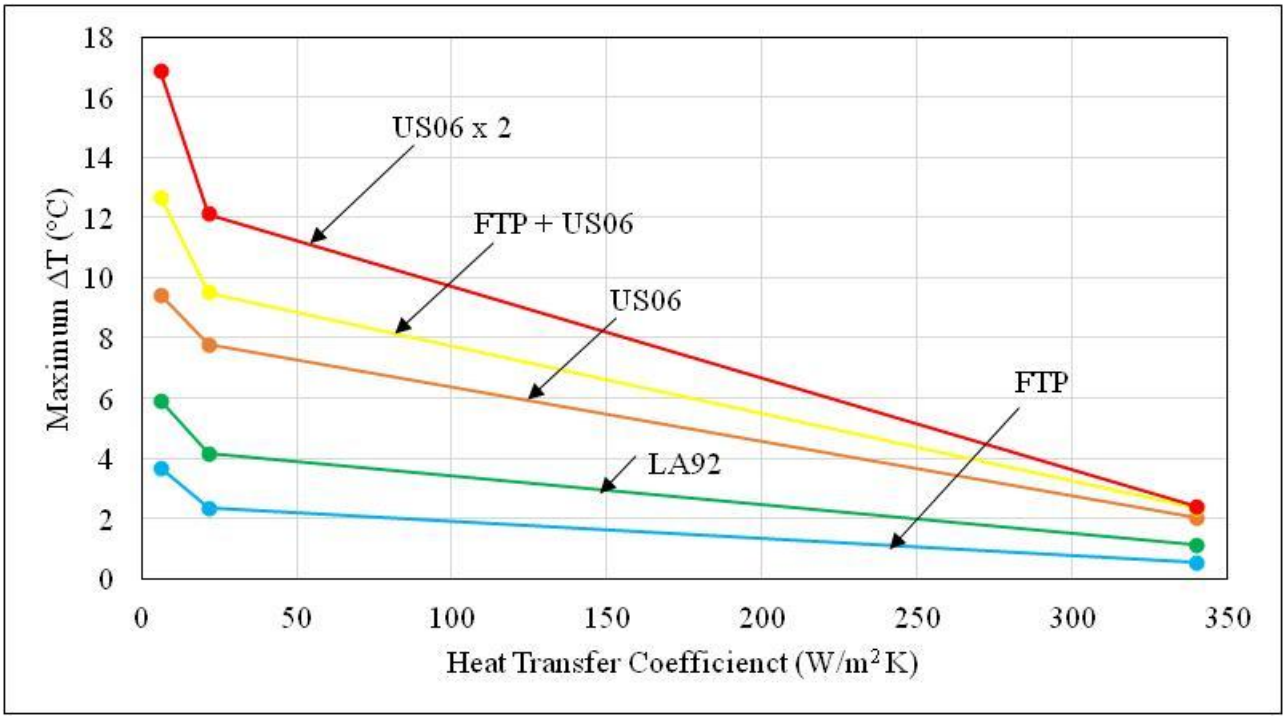

Figure 7-17: Maximum cell temperature over time for a single drive cycle with varying heat transfer coefficients; initial temperature of 35°C

Observing the above plots clearly shows the need for effective thermal management. While the FTP drive cycle shows minimal temperature increase, other drive cycle displays a considerable increase in cell temperature over a single drive cycle. However, with effective thermal management (as described with h = 340 W/m^3) the effects of even severe and aggressive driving can be mitigated. For instance, the US06 drive cycle which represents high intensity driving for 10 minutes, a very realistic case, would result in an average cell temperature of 4°C higher than the base temperature and a maximum temperature almost 10°C higher than the base, with no cooling system. With effective cooling this can be reduced to a 1°C increase in average temperature and only a 2°C maximum increase. As a reminder, heat generation was seen to be even more severe in 20°C, making thermal management systems even more useful.

The last result to reiterate is how much driving habits can influence a need for effective thermal management can be seen by observing heat generation rates for the different drive cycles in Figure 7-18.

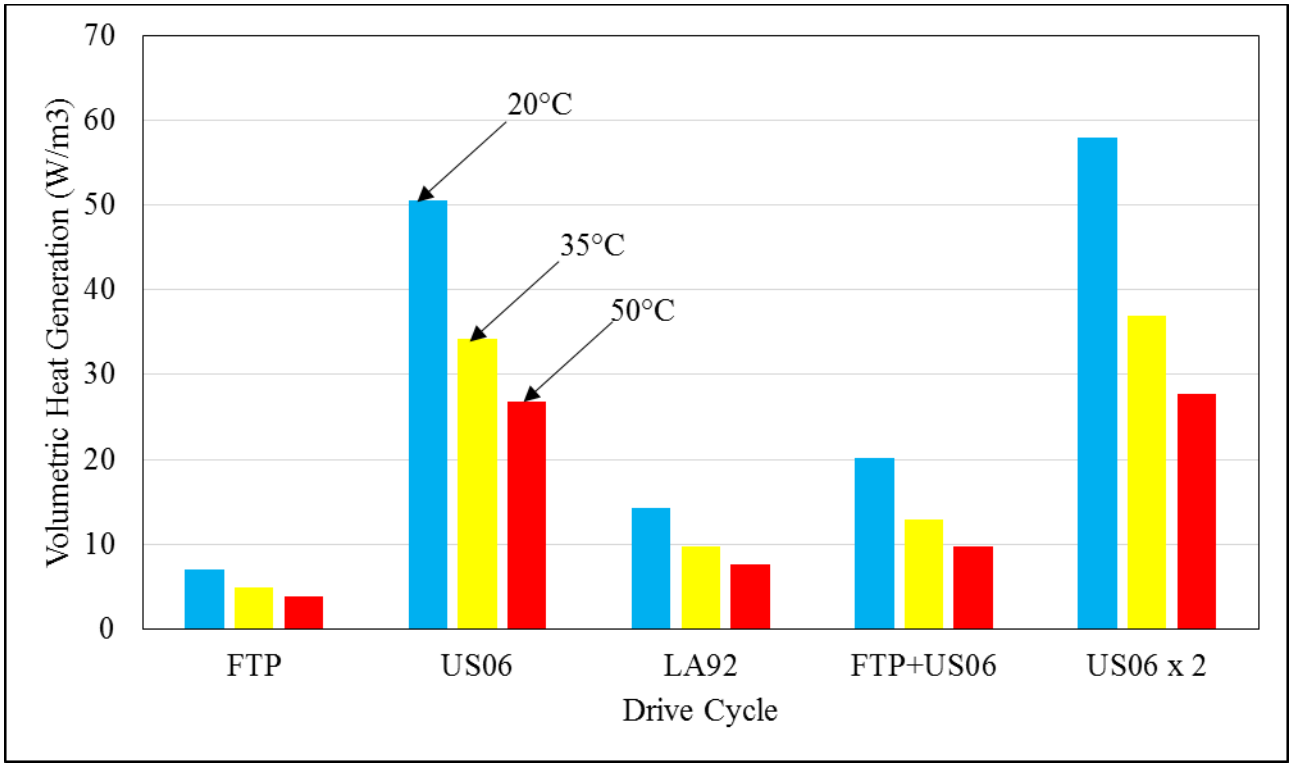

Figure 7-18: Average volumetric heat generation during a single drive cycle; h = 340 W/m^3

One final note to make is regarding environmental conditions. Effective thermal management must also be utilized to combat environmental conditions. In this study, the initial temperature of the battery was always set to the same temperature of the coolant. In reality, environmental conditions must also be taken into account when considering the thermal condition for a battery. For instance, if the desired battery temperature is 25°C, not only must temperature increase due to battery heat generation be mitigated, but if this vehicle is operating in a warm region (such as the southern United States) environmental conditions will also lend to increasing battery temperature.

Over this results section, the effect of thermal management system on lithium-ion battery capacity fade has been presented, and the need for effective thermal management has been demonstrated. This information is very useful for the industry partner who wishes to demonstrate to customers the need for effective cooling (ICE plate employing a coolant) opposed to simpler thermal management systems.

8 Conclusions

The section will reiterate the conclusions made during the course of this study.

Firstly, AutoLionST has shown to be a useful tool to model the operation and ageing of lithium-ion batteries. Inclusion of film formation and active material loss degradation mechanisms allow reflect the major ageing mechanisms in lithium-ion batteries. The only time these mechanisms alone are not suitable is at very low temperatures where lithium plating becomes the dominant contributor to battery degradation. While it is possible to adjust degradation parameters to give acceptable results at lower temperatures (20°C), it is not recommended to perform extended degradation testing at very low temperatures with this software, since the true degradation mechanisms are not being reflected.

As expected higher temperatures provide a higher initial capacity, however elevated temperatures (namely above 30°C) will result in much accelerated ageing.

Through the simulation of constant C-rate operation, it was shown that a choice of effective thermal management can significantly improve battery life. The importance of thermal management is most crucial at high C-rate operation, and the need to prevent battery temperature rise is most important at desirable battery temperatures (20-30°C).

Upon performing simulations employing FTP drive cycles, further conclusions can be drawn regarding battery performance against the variables of cell temperature, charge voltage, and heat transfer coefficient. Of the three variables, temperature again has the largest effect on capacity fade, a result which was expected following the result of the isothermal simulations. Again, a high heat transfer can significantly improve battery life, especially at desirable temperatures, with approximately 25% improvement in battery life. It was also shown by including regenerative braking into the model that a lower charge voltage will also contribute to improved battery life, and that using regenerative braking, these lower charge voltages can be used with less risk of reaching the lower voltage limit of the battery pack.

Following the drive cycle capacity fade simulations, the effect of different drive cycles on the cell operating temperature and heat generation was explored. It was shown that the FTP drive cycle represents very low intensity driving, and that other drive cycles, which better reflect certain real life driving conditions, result in increased heat generation and large increases in cell temperature during operation. As shown in earlier results, heat generation and significant temperature increase will lead to enhanced battery degradation. Therefore, it was shown that while thermal management plays an even more significant role when considering high intensity driving. Hence, in electric vehicles thermal management is important not only to combat environmental conditions, but is also crucial to battle the heat generation of the battery pack.

9 Future Work

The following is a brief discussion of the future work which could follow this study.

Firstly, further experimental experimentation would be very beneficial in order to ensure the model is properly calibrated to experimental data. Ideally this would include extended testing, hopefully to around 1000 cycles per cell, at multiple temperatures, with replication for each temperature (multiple cells cycled per temperature). Having such thorough experimental data would give a good measure of the variance between batteries when it comes to real life use, hence leading to more realistic model prediction once this data is used to calibrate the model.

As well, it is desired to extend results to capture the effect of temperature gradients on capacity fade of lithium-ion batteries. In many cases thermal gradients will exist both across the face of lithium-ion batteries, and through their thickness. As seen in the literature review, many researchers have documented that overall battery temperature has an effect on capacity fade, however no literature exists documenting the effect that non-uniformity of temperature has on capacity fade. For instance, if two batteries are both at an average temperature of 35°C, with one having a uniform temperature distribution, and one having minimum/maximum temperatures of 25°C and 40°C, respectively, how would their degradation vary? As a direct extension of the work presented in this study, the temperature gradients which are created for different thermal management systems can be studied, and the effect of these gradients on degradation can be explored.

If AutoLionST were to be used to study the effect of temperature gradients, multiple batteries at varying temperatures could be simulation in parallel, together representing different temperature zones of a single battery. This would be necessary since AutoLionST does not discretize temperature modeling. This work could also involve employing other AutoLion software, such as their 1D or 3D software which are Fluent based (opposed to MATLAB based).

References

[1] "UN News Centre - 'Today Is An Historic Day,' Says Ban, As 175 Countries Sign Paris Climate Accord", *UN News Centre,* 2016. Retrieved from *http://www.un.org/apps/news/ story.asp?NewsID=53756#.V9w80DUjOZN*.

[2] "Climate change: How Do We Know?", *NASA: Global Climate Change,* 2016. Retrieved from *http://climate.nasa.gov/evidence/.*

[3] "U.S. Greenhouse Gas Inventory Report: 1990-2014", *US Environmental Protection Agency*, 2016. Retrieved from *www3.epa.gov*.

[4] "Greenhouse Gas Emissions by Economic Sector", *Environment and Climate Change Canada,* 2016. Retrieved from *https://www.ec.gc.ca/indicateursindicators/default. asp?la ng=en&n=F60DB708-1*.

[5] "Greenhouse Gas Emissions", *US Environmental Protection Agency*, 2016. Retrieved from *www3.epa.gov*.

[6] S. Campanari, et al. "Energy analysis of electric vehicles using batteries or fuel cells through well-to-wheel driving cycle simulations." J. of Power Sources 186 (2009) 464-477.

[7] "Top Six Plug-in Vehicle Adopting Countries -2015", *hybridCARS,* 2016. Retrieved from *http://www.hybridcars.com/top-six-plug-in-vehicle-adopting-countries-2015/.*

[8] "Monthly Plug-In Sales Scorecard", *InsideEVs,* 2016. Retrieved from *http://insideevs.com/monthly-plug-in-sales-scorecard/.*

[9] "Chevy Bolt electric car could be 'the first mass-market EV success'", *Los Angeles Times,* 2015. Retrieved from *http://www.latimes.com/business/autos/la-fi-0113-chevrolet-volt-bolt-20150112-story.html.*

[10] "www.fueleconomy.gov", *U.S. Department of Energy*, 2016. Retrieved from *http://www.fueleconomy.gov/feg/Find.do?action=sbs&id=34918&id=34699&id=33558 &id=32154.*

[11] "EPA rating for 85 kWh Tesla Model S: 89 MPGe, 265-mile range", *Green Car Congress,* 2012. Retrieved from *http://www.greencarcongress.com/2012/06/models-20120621.html.*

[12] "With Tesla Model 3 Orders Nearing 400,000, Chevy Bolt Feels Heat of Tesla Brand", *Forbes,* 2016. Retrieved from *http://www.forbes.com/sites/brookecrothers/2016/04/15/ with-tesla-model-3-orders-nearing-400000-chevy-bolt-feels-heat-of-tesla-brand/#71c90a485349.*

[13] "Purchase or Lease Rebate Program", *Quebec Ministry of Transportation*, 2012. Retrieved from *http://www.vehiculeselectriques.gouv.qc.ca/english/particuliers/rabais.asp.*

[14] "New incentive to make clean energy vehicles more affordable", *Province of British Columbia,* 2015. Retrieved from *https://archive.news.gov.bc.ca/releases/news_releases_2013-2017/2015MEM0009-000380.htm.*

[15] "Ontario Making Electric Vehicles More Affordable", *Government of Ontario,* 2016. Retrieved from *https://news.ontario.ca/opo/en/2016/02/ontario-making-electric-vehicles-more-affordable.html?_ga=1.90272282.1899543433.1462901645.*

[16] "Incentives", *Tesla,* 2016. Retrieved from *https://www.teslamotors.com/en_CA/support/incentives.*

[17] L. Lu, et al. "A review on the key issues for lithium-ion battery management in electric vehicles." J. of Power Sources, 226 (2013) 272-288.

[18] B. Scrosati, and J Garche. "Lithium batteries: Status, prospects and future." J. of Power Sources, 195 (2010) 2419-2430.

[19] J.K. Park. "Principles and Applications of Lithium Secondary Batteries". John Wiley & Sons Inc., 2012.

[20] D. Linden, and T.B. Reddy. "Handbook of Batteries: Third Edition". McGraw-Hill Inc., 2002.

[21] T. Engel, and P. Reid. "Thermodynamics, Statistical Thermodynamics, & Kinetics". Pearson Education Inc., 2010.

[22] L. Ji, et al. "Recent developments in nanostructured anode materials for rechargeable lithium-ion batteries." Energy Environ. Sci., 4 (2011) 2682-2699.

[23] T. Ohzuku, and R.J. Brodd. "An overview of positive-electrode materials for advanced lithium-ion batteries." J. of Power Sources, 174 (2007) 449-456.

[24] J.M. Tarascon, and M. Armand. "Issues and challenges facing rechargeable lithium batteries." Nature, 414 (2001) 359-367.

[25] "BU-301a: Types of Battery Cells", *Battery University*, 2016. Retrieved from *http://batteryuniversity.com/learn/article/types_of_battery_cells.*

[26] "What Goes Into A Tesla Model S Battery--And What It May Cost", *Green Car Reports,* 2013. Retrieved from *http://www.greencarreports.com/news/1084682_what-goes-into-a-tesla-model-s-battery--and-what-it-may-cost.*

[27] B. Dunn, et al. "Electrical Energy Storage for the Grid: A Battery of Choices." Science, 334 (2011) 928-935.

[28] Q. Wang, et al. “Thermal runaway caused fire and explosion of lithium ion battery.” J. of Power Sources, 208 (2012) 210-224.

[29] P. Arora, et al. “Capacity Fade Mechanisms and Side Reactions in Lithium-Ion Batteries.” J. Electrochem. Soc., 145 (1998) 3647-3666.

[30] P. Ramadass, et al. “Capacity fade of Sony 18650 cells cycled at elevated temperatures Part I. Cycling performance.” J. of Power Sources, 112 (2002) 606-613.

[31] P. Ramadass, et al. “Capacity fade of Sony 18650 cells cycled at elevated temperatures Part II. Capacity fade analysis.” J. of Power Sources, 112 (2002) 614-620.

[32] P. Ramadass, et al. “Development of First Principles Capacity Fade Model for Li-Ion Cells.” J. Electrochem. Soc., 151 (2004) A196-A203.

[33] J. Vazquez-Arenas, et al. “Modeling of combined capacity fade with thermal effects for a cycled Li_xC_6-$Li_yMn_2O_4$ cell.” J. of Power Sources, 215 (2012) 28-35.

[34] R. Deshpande, et al. “Battery Cycle Life Prediction with Coupled Chemical Degradation and Fatigue Mechanics.” J. Electrochem. Soc., 159 (2012) A1730-A1738.

[35] L. Cai, et al. “Life modeling of lithium ion cell with a spinel-based cathode.” J. of Power Sources, 221 (2013) 191-2000.

[36] A.J. Smith, et al. “A High Precision Coulemetry Study of the SEI Growth in Li/Graphite Cells.” J. Electrochem. Soc., 158 (2011) A447-A452.

[37] P. Ramadass, et al. “Mathematical modeling of the capacity fade of Li-ion cells.” J. of Power Sources, 123 (2003) 230-240.

[38] K. Amine, et al. “Mechanism of capacity fade of MCMB/$Li_{1.1}[Ni_{1/3}Mn_{1/3}Co_{1/3}]_{0.9}O_2$ cell at elevated temperature and additives to improve its cycle life.” J. Mater. Chem., 21 (2011) 17754-17759.

[39] J. Vetter, et al. “Ageing mechanisms in lithium-ion batteries.” J. of Power Sources 147 (2005) 269-281.

[40] P. Bro, and S.C. Levy. “Quality and Reliability Methods for Primary Batteries”. John Wiley & Sons Inc., 1990.

[41] R. Fong, et al. “Studies of Lithium Intercalation into Carbons Using Nonaqueous Electrochemical Cells.” J. Electrochem. Soc., 137 (1990) 2009-2013.

[42] Y. Chen, and J.W. Evans. “Thermal Analysis of Lithium Polymer Electrolyte Batteries by Two Dimensional Model-Thermal Behaviour and Design Optimization.” Electrochemica Acta, 39 (1994) 517-526.

[43] Y. Chen, and J.W. Evans. “Thermal Analysis of Lithium-Ion Batteries.” J. Electrochem. Soc. 143 (1996) 2708-2712.

[44] S. Al Hallaj, et al. “Thermal modeling and design considerations of lithium-ion batteries.” J. of Power Sources 83 (1999) 1-8.

[45] H. Maleki, and A.K. Shamsuri. “Thermal analysis and modeling of a notebook computer battery.” J. of Power Sources (2002) 131-136.

[46] S.A. Khateeb, et al. “Design and simulation of a lithium-ion battery with a phase change material thermal management system for an electric scooter.” J. of Power Sources 128 (2004) 292-307.

[47] A. Mills, and S. Al-Hallaj. “Simulation of passive thermal management system for lithium-ion battery packs.” J. of Power Sources 141 (2005) 307-315.

[48] R. Sabbah, et al. “Active (air-cooled) vs. passive (phase change material) thermal management of high power lithium-ion packs: Limitation of temperature rise and uniformity of temperature distribution.” J. of Power Sources 182 (2008) 630-638.

[49] G. Karimi, and X. Li. “Thermal management of lithium-ion batteries for electric vehicles.” Int. J. Energy Res. 37 (2013) 13-24.

[50] D. Bernardi, et al. “A General Energy Balance for Battery Systems.” J. Electrochem. Soc. 132 (1985) 5-12.

[51] M. Doyle, et al. “Modeling of Galvanostatic Charge and Discharge of the Lithium/Polymer/Insertion Cell”, J. Electrochem. Soc. 140 (1993) 1526-1533.

[52] W. Fang, et al. “Electrochemical-thermal modeling of automotive Li-ion batteries and experimental validation using a three-electrode cell.” Int. J. Energy Res. 34 (2009) 107-115.

[53] W.B. Gu, and C.Y. Wang. “Thermal-Electrochemical Coupled Modeling of a Lithium-Ion Cell.” J. Electrochem. Soc. 147 (2000) 2910-2922.

[54] V. Srinivasan, and C.Y. Wang. “Analysis of Electrochemical and Thermal Behaviour of Li-Ion Cells.” J. Electrochem Soc. 150 (2003) A98-A106.

[55] K. Smith, and C.Y. Wang. “Power and thermal characterization of a lithium-ion battery pack for hybrid-electric vehicles.” J. of Power Sources 160 (2006) 662-673.

[56] N. Omar, et al. “Assessment of Performance of Lithium Iron Phosphate Oxide, Nickel Manganese Cobalt Oxide and Nickel Cobalt Aluminium Oxide Based cells for Using in Plug-in Battery Electric Vehicle Applications.” IEEE Vehicle Power and Propulsion Conference (2011).

[57] EC Power, “AutoLionST: A Thermally Coupled Battery Model for System-level Analysis of Li-ion Battery Packs, User’s Manual.” 2015.

[58] M. Doyle, et al. “Comparison of Modeling Predictions with Experimental Data from Plastic Lithium Ion Cells.” J. Electrochem. Soc. 143 (1996) 1890-1903.

[59] L.O. Valøen, and J.N. Reimers. “Transport Properties of $LiPF_6$-Based Li-Ion Battery Electrolytes.” J. Electrom. Soc. 152 (2005) A882-A891.

[60] K.E. Thomas, et al. “Measurement of the Entropy of Reaction as a Function of State of Charge in Doped and Undoped Lithium Manganese Oxide.” J. Electrochem. Soc. 148 (2001) A570-A575.

[61] S. Al Hallaj, et al. “Entropy Changes Due to Structural Transformation in the Graphite Anode and Phase Change of the $LiCoO_2$ Cathode.” J. Electrochem. Soc. 147 (2000) 2432-2436.

[62] “Polymer Lithium-ion Battery Safety Data Sheets,” *AA Portable Power Corp,* 2012.

[63] M. Liu, “Polymer Lithium-ion Battery Product Specification, Model:10059156-5C,” *AA Portable Power Corp,* 2012.

[64] “AutoLionST: Lithium-Ion Battery Simulator.” Version 5.0, software produced by *EC Power LLC, 2015.*

[65] M. Safoutin, "Wheels: Vehicle Road Load and Fuel Economy online calculator," *Wheels: Vehicle Road Load and Fuel Economy Online Calculator,* 2009. Retrieved from *http://www.virtual-car.org/wheels/wheels-road-load-calculation.html*.

[66] “Dynamometer Drive Schedules,” *United States Environmental Protection Agency,* 2013. Retrieved from *http://www3.epa.gov/nvfel/testing/dynamometer.htm*.

[67] “2014 Chevrolet Volt,” *Car and Driver,* 2014. Retrieved from *http://www.caranddriver.com/.*

[68] “2015 Chevrolet Volt,” *Hybrid and Electric Cars Reviews,* 2014. Retrieved from *http://hybridcars.reviews/2015-chevrolet-volt/*.

[69] “Battery Cooling Plate”, *Automotive World,* 2013. Image retrieved from *https://jan2013.tems-system.com/exhisearch/CAR/eng/searchResult_detail.aspx ?id=00789787-1f9b-4ddd-a0c5-e1b498eb8377.*

[70] “Federal Test Procedure Revisions,” *United States Environmental Protection Agency,* 2015. Retrieved from *http://www3.epa.gov/otaq/sftp.htm*.

[71] “EPA fuel economy ratings – what’s coming in 2008”, *Earthcars,* 2007. Retrieved from *http://web.archive.org/web/20071008015835/http://www.earthcars.com/articles/article .htm?articleId=6.*

[72] “Silver Ice 710NS Data Sheet” *TIMTRONICS*: Thermal Interface Material.

[73] “Emerald-ABT: Test Control Software For Advanced Battery Testing User Manual,” *Greenlight Innovation,* 2012.

[74] “Laboratory Temperature Control Products,” *Thermo Scientific,* 2010.

[75] “AC200 Immersion Circulators”, *ThermoFisher Scientific*, 2016. Retrieved from https://www.thermofisher.com/order/catalog/product/156-0001.

[76] “Thermocouples: Using Thermocouples in Temperature Measurement,” *OMEGA*, 2016. Retrieved from http://www.omega.ca/prodinfo/thermocouples.html.

Appendix A: Full List of AutoLionST Battery Parameters

Table A-1: Cell dimensions

Cell Dimension	Value (mm)	Status
Cell width	60	Selected
Cell height	162	Selected
Cell thickness	11	Selected
Inner width	55	Selected
Inner height	148	Selected
Inner thickness	8	Selected

Table A-2: Positive electrode material parameters and properties [64]

Positive Electrode			
Foil Parameters	**Value**	**Units**	**Status**
Material	Aluminum	-	Selected
Thickness	15	µm	Default
Width	59.7	mm	Default
Density	2.7	g/cm^3	Default
Conductivity	$3.538*10^7$	S/m	Default
Active Material Parameters	**Value**	**Units**	**Status**
Material	NMC	-	Selected
Molecular Weight	96.461	g/cm^3	Material Constant
Density	4.8	g/cm^3	Material Constant
1^{st} Charge Capacity	163	mAh/g	Material Constant
1^{st} Discharge Capacity	153	mAh/g	Material Constant
Umax	4.3	V	Material Constant
Particle Size	10	µm	Material Constant
Weight Percentage	94%	-	Default
Conductive Agent Parameters	**Value**	**Units**	**Status**
Material	Carbon	-	Default
Density	1.95	g/cm^3	Default
Weight Percentage	3%	-	Default
Binder Parameters	**Value**	**Units**	**Status**
Material	PVdF	-	Default
Density	1.77	g/cm^3	Default
Weight Percentage	3%	-	Default
Coating Parameters	**Value**	**Units**	**Status**
Loading	3.9	mAh/cm^2	Selected
Electrode Thickness	170	µm	Selected
Electrode Width	49	mm	Selected
Electrode Height	144	mm	Selected
# of Electrode Plates	20	-	Calculated

Table A-3: Negative electrode material parameters and properties [64]

Negative Electrode			
Foil Parameters	**Value**	**Units**	**Status**
Material	Copper	-	Selected
Thickness	8	µm	Default
Width	59.7	mm	Default
Density	8.96	g/cm^3	Default
Conductivity	$5.8*10^7$	S/m	Default
Active Material Parameters	**Value**	**Units**	**Status**
Material	Graphite	-	Selected
Molecular Weight	72.06	g/cm^3	Material Constant
Density	2.24	g/cm^3	Material Constant
1^{st} Charge Capacity	371.933	mAh/g	Material Constant
1^{st} Discharge Capacity	350	mAh/g	Material Constant
Umax	2	V	Material Constant
Particle Size	15	µm	Material Constant
Weight Percentage	94%	-	Default
Conductive Agent Parameters	**Value**	**Units**	**Status**
Material	Carbon	-	Default
Density	1.95	g/cm^3	Default
Weight Percentage	3%	-	Default
Binder Parameters	**Value**	**Units**	**Status**
Material	PVdF	-	Default
Density	1.77	g/cm^3	Default
Weight Percentage	3%	-	Default
Coating Parameters	**Value**	**Units**	**Status**
N/P Ratio	115%	-	Selected
Loading	4.485	mAh/cm^2	Calculated
Electrode Thickness	170	µm	Selected
Electrode Width	49	mm	Selected
Electrode Height	144	mm	Selected
# of Electrode Plates	21	-	Calculated

Table A-4: Separator parameters [64]

Separator Parameters	**Value**	**Units**	**Status**
Type	Celgard	-	Default
Thickness	20	µm	Default
Height	145	mm	Selected
Porosity	0.4	-	Default

Table A-5: Electrolyte Parameters [64]

Electrolyte Parameters	Value	Units	Status
Lithium Salt	$LiPF_6$	-	Default
Solution	EC-EMC-DMC	-	Default
Concentration	1.2	mol/L	Default
Density	1.2	g/cm^3	Default

Table A-6: Cell specifications [64]

Cell Specifications	Value	Units	Status
Cell Surface Area	243.24	cm^2	Calculated
Cell Volume	106.92	cm^3	Calculated
Cell Weight	199.12	g	Calculated
Cell Capacity	10.224	Ah	Calculated

Table A-7: Cell sizing [64]

Cell Sizing	Weight (g)	Status
Negative Active Material	35.74	Calculated
Positive Active Material	67.53	Calculated
Separator	4.27	Calculated
Electrolyte	17.61	Calculated
Negative Electrode Binder/Additive/Conductive Agent	2.28	Calculated
Positive Electrode Binder/Additive/Conductive Agent	4.31	Calculated
Negative Current Collector	10.62	Calculated
Positive Current Collector	5.72	Calculated
Enclosure	51.05	Selected

Table A-8: Mesh parameters [64]

Mesh Number Parameters	Value	Status
Negative Electrode	8	Default (verified with mesh refinement)
Separator	5	Default (verified with mesh refinement)
Positive Electrode	8	Default (verified with mesh refinement)

Table A-9: Operating conditions [64]

Operating Conditions	Value (V)	Status
Lower Cut-off Voltage	2.75	Selected
Upper Cut-off Voltage	4.2	Selected

Table A-10: Initial conditions [64]

Initial Conditions	**Value**	**Units**	**Status**
Cell Temperature	Varies	K	Selected
OCV@100%SOC	4.2	V	Selected
SOC	Varies	-	Selected

Table A-11: Butler-Volmer equation parameters [64]

Butler-Volmer Equation			
Negative Electrode	**Value**	**Units**	**Status**
Open Circuit Potential	database	V	Database
Anodic Transfer Coefficient	0.5	-	Default
Cathodic Transfer Coefficient	0.5	-	Default
Exchange Current Density	database	A/m^2	Database
SEI Layer Thickness	5	nm	Default
SEI Layer Resistance	0.00033	$Ohm*m^2$	Default
Activation Energy	$3.2*10^4$	J/mol	Default
dU/dT (Entropic heat)	database	V/K	Database
Positive Electrode	**Value**	**Units**	**Status**
Open Circuit Potential	database	V	Database
Anodic Transfer Coefficient	0.5	-	Default
Cathodic Transfer Coefficient	0.5	-	Default
Exchange Current Density	database	A/m^2	Database
Film Thickness	2	nm	Default
Film Resistance	0.00013	$Ohm*m^2$	Default
Activation Energy	$3.2*10^4$	J/mol	Default
dU/dT (Entropic heat)	database	V/K	Database

Table A-12: Bruggeman exponents [64]

Bruggeman Exponents	**Value**	**Status**
Negative	1.5	Default
Separator	1.5	Default
Positive	1.5	Default

Table A-13: Electrolyte concentration properties [64]

Electrolyte Concentration	**Value**	**Units**	**Status**
Average Concentration	1200	mol/m^3	Default
Diffusion Coefficient	Database	m^2/s	Default
Transference Number	0.38	-	Default

Table A-14: Solid state diffusion properties [64]

Solid State Diffusion	Value	Units	Status
Negative Active Material Diffusion Coefficient	database	m^2/s	Database
Positive Active Material Diffusion Coefficient	database	m^2/s	Database

Table A-15: Electrolyte potential properties [64]

Electrolyte Potential	Value	Units	Status
Ionic Conductivity	database	S/m	Database
Diffusional Conductivity	database	A/m	Database

Table A-16: Solid phase potential properties [64]

Solid Phase Potential			
Negative Electrode	**Value**	**Units**	**Status**
Conductivity	100	S/m	Default
Contact Resistance	0.0002	$Ohm*m^2$	Default
Positive Electrode	**Value**	**Units**	**Status**
Conductivity	3.8	S/m	Default
Contact Resistance	0.0002	$Ohm*m^2$	Default

Table A-17: Heat transfer parameters [64]

Heat Transfer	Value	Units	Status
Thermal Model	On	-	Selected
Specific Heat	1000	J/kg*K	Default

Table A-18: Degradation controls [64]

Degradation Controls	Value	Units	Status
Characterization Frequency	50 or 73	-	Selected
Characterization Discharge Current	10	A	Selected
Start From	0	-	Selected

Table A-19: Degradation parameters [64]

Degradation Parameters			
Negative Electrode Film Growth			
	Value	**Units**	**Status**
SEI Layer Growth Model	On	-	-
Molecular Weight	162	g/mol	Default
Density	1.69	g/cm^3	Default
Porosity	0.05	-	Default
Rate Constant	$1.3*10^{-18}$	m/s	Selected
Activation Energy	$8.53*10^{4}$	J/mol	Default
Positive Electrode Film Growth			
	Value	**Units**	**Status**
Film Growth Model	On	-	-
Molecular Weight	162	g/mol	Default
Density	1.69	g/cm^3	Default
Porosity	0.02	-	Default
Rate Constant	$3.1*10^{-8}$	m/s	Default
Activation Energy	$2.5*10^{4}$	J/mol	Default
Negative Electrode AM Isolation			
	Value	**Units**	**Status**
AM Isolation Model	On	-	-
Rate Constant	$3.47*10^{-14}$ ($5.11*10^{-14}$ for 20°C)	m/s	Selected
Activation Energy	$4*10^{4}$	J/mol	Default
Positive Electrode AM Isolation			
	Value	**Units**	**Status**
AM Isolation Model	On	-	-
Rate Constant	0	m/s	Default
Activation Energy	$3*10^{4}$	J/mol	Default

Appendix B: Full List of Dynamic Outputs for AutoLionST

Table B-1: Dynamic outputs in the Simulink environment [57]

Parameter	Description	Units
Time	Tracks time of simulations	min
Current	Current output of battery	A
Voltage	Voltage output of battery	V
Power	Power output of battery	W
Temperature	Average battery temperature	K
Qtotal	Instantaneous heat generation of battery	W
SOC	State of charge of battery; instantaneous capacity/design capacity	-
Degraded Capacity	Capacity of battery throughout cycling	Ah
OCV	Open circuit voltage of battery throughout cycling	V
Ce1	Electrolyte concentration at anode/current collector interface	mol/m^3
Ce2	Electrolyte concentration at anode/separator interface	mol/m^3
Ce3	Electrolyte concentration at cathode/current collector interface	mol/m^3
Ce4	Electrolyte concentration at cathode/separator interface	mol/m^3
Stoich1	Stoichiometry of Li at the active material particle surface at anode/current collector interface	
Stoich2	Stoichiometry of Li at the active material particle surface at anode/separator interface	
Stoich3	Stoichiometry of Li at the active material particle surface at cathode/current collector interface	
Stoich4	Stoichiometry of Li at the active material particle surface at cathode/separator interface	